The effect of temperature on phase transformation mechanisms in electrodes for Li-ion batteries

Wei Meng

Churchill College
Department of Chemistry
University of Cambridge
September 2017

This dissertation is submitted for the degree of

Doctor of Philosophy

Declaration

This thesis is the result of my own work and includes nothing, which is the outcome of work done in collaboration except as declared in the Preface and specified in the text.

It is not substantially the same as any that I have submitted, or, is being concurrently submitted for a degree or diploma or other qualification at the University of Cambridge or any other University or similar institution except as declared in the Preface and specified in the text. I further state that no substantial part of my dissertation has already been submitted, or, is being concurrently submitted for any such degree, diploma or other qualification at the University of Cambridge or any other University or similar institution except as declared in the Preface and specified in the text

This thesis does not exceed the word limit of 60,000, including summary/abstract, tables, and footnotes, but excluding table of contents, photographs, diagrams, figure captions, list of figures/diagrams, list of abbreviations/acronyms, bibliography, appendices and acknowledgements.

Acknowledgement

I am grateful to my supervisor Professor Clare P. Grey, who has given me an incredible support and guidance throughout my PhD. She gave me the opportunity to enter the field of energy storage materials, which I have long been craving for. Her knowledge, ideas, and spirit have always been enlightening, and I feel truly privileged to have had her as my supervisor.

My PhD work would not have been possible without the day-to-day supervision by Dr. Oliver Pecher. I gratefully acknowledge his training and help on both scientific and organisational challenges. My great gratitude also goes to Dr. Paul Bayley (now: Apple Inc., CA, US), who guided me into the PhD life and the subject of batteries and electrolytes. I would also like to thank Dr. Michael Gaultois for numerous fruitful discussions and the different perspectives he offered whenever I encounter difficult problems.

I gratefully acknowledge the generous support of many current and previous members of the Grey research group. In particular, I thank Roberta Pigliapochi (who has done most of the density functional calculation in this thesis, as will be specified in the text), Dr. Ieuan Seymour, Kent Griffith, and Matthew Sullivan (now: Dehns, Brighton, UK) for their help during collaborations on various projects. Furthermore, I gratefully acknowledge Dr. Hao Liu (now: Advanced Photon Source, Argonne National Laboratory, IL, US), Dr. Phoebe Allan (now: Gonville and Caius College, University of Cambridge, UK), Dr. Javier Carretero Gonzalez (now: Polymer Science and Technology Institute, Madrid, Spain), Dr. Matthias Groh, Dr. Sylvia Britto, Dr. Elizabeth Castillo Martinez, Dr. Tao Liu, Dr. Alison Michan, and Dr. Wanjing Yu (now: Zhongnan University, China) for fruitful discussions.

Collaboration with research facilities, industry, and engineering experts has been key to achieve many of the goals of my thesis. At Diamond Light Source (DLS, Didcot, UK), I sincerely thank Prof. Chiu Tang and Dr. Sarah Day for their help in developing and testing the high-temperature *in situ* X-ray diffraction setup. At Advanced Photon Source (APS, IL, US), I thank Dr. Wenqian Xu, Dr. Kamila Wiaderek, Dr. Karena Chapman, and Dr. Peter Chupas for their great assistance during my beamtime. At Schlumberger Gould Research (SGR, Cambridge, UK), I thank Prof. Han-Pu Liang (now: Chinese Academy of Science, Qingdao, China), Dr. Nathan Lawrence (now: ANB Sensors, Cambridge, UK), and Dr. Tim Jones for their support of my PhD work. Furthermore, I would like to thank Manuel Wentscher, Wayne Bailey, Simon Dowe, and Richard Nightingale (Department of Chemistry, Electronic and

Mechanical Workshop) for their help and technical guidance regarding the development and manufacturing of the high-temperature *in situ* X-ray diffraction setup.

Last but not least, I am thankful to my friends, Xinya Bian, Zheng Lin, Kaiyan Xiao, Deli Zhang, Cen Zhang, Zhen Du, and Xiaonan Wang. My special thanks also go to Xiaomei Ouyang, who brings so much joy and happiness to my life. And finally, I am grateful to my parents, Fang Zheng and Xianjia Meng, for their continuing care and support.

Publications

Chapter 3 is based on the work that is in preparation for the following publications:

Wei Meng, Roberta Pigliapochi, Paul M. Bayley, Oliver Pecher, Michael W. Gaultois, Kent J. Griffith, Ieuan D. Seymour, Sarah J. Day, Chiu Tang, and Clare P. Grey, "Toward a High-Temperature V_6O_{13} Based Lithium-Ion Battery", *Manuscript in Preparation* **2017**.

Wei Meng, Oliver Pecher, Michael W. Gaultois, Matthew Sullivan, Sarah J. Day, Chiu Tang, and Clare P. Grey, "The Effect of Temperature on Phase Transformation Mechanisms in $LiFePO_4$ Electrodes during High-Rate Cycling", *Manuscript in Preparation* **2017**.

Chapter 4 is based on the work that was published in following paper:

Wei Meng, Roberta Pigliapochi, Paul M. Bayley, Oliver Pecher, Michael W. Gaultois, Ieuan D. Seymour, Han-Pu Liang, Wenqian Xu, Kamila M. Wiaderek, Karena W. Chapman, and Clare P. Grey, "Unraveling the Complex Delithiation and Lithiation Mechanisms of the High Capacity Cathode Material V_6O_{13}", *Chem. Mater.* **2017**, *29*, 5513–5524.

DOI: 10.1021/acs.chemmater.7b00428

Chapter 5 is based on the work that is in preparation for the following publication:

Wei Meng, Roberta Pigliapochi, Paul M. Bayley, Oliver Pecher, Michael W. Gaultois, Kent J. Griffith, Ieuan D. Seymour, Sarah J. Day, Chiu Tang, and Clare P. Grey, "Toward a high-temperature V_6O_{13} based lithium-ion battery", *Manuscript in Preparation* **2017**.

Summary

The effect of elevated temperatures on the phase transformation mechanisms in electrodes for lithium-ion batteries (LIBs) is an important but – to date – only less studied subject in battery research. In real-life applications, LIBs usually function at non-ambient conditions and especially increased temperatures give rise to safety concerns. This thesis focuses to gain deeper insights into the phase transformations at high temperatures (HTs) by tackling both the challenging hardware development of a HT *in situ* synchrotron X-ray diffraction (XRD) battery testing system as well as its application to study two important cathode materials: $LiFePO_4$ and V_6O_{13}. This allows unprecedented insights into the structural changes and its influence on electrochemical performance at variable temperatures (VTs).

$LiFePO_4$ was investigated for various battery cycling rates and temperatures. Electrochemical cycling of $LiFePO_4$ in the newly designed *in situ* XRD setup proved that the *in situ* XRD cells work from low to high cycling rates between 25 to 150°C. The current induced non-equilibrium solid solution metastable $LiFePO_4$ phase, present at room temperature during high rate cycling, was found to be less pronounced at temperatures above 125°C. This is possibly due to faster Li-ion diffusion at HT, leading to faster phase separations in the solid solution phases.

In a next step, V_6O_{13}, a promising cathode material for HT applications, especially for oil field applications, was tested using the *in situ* HT XRD setup. The material exhibits a very high capacity with a complex voltage profile. The underlying asymmetric discharge and charge phase transition mechanisms, which include a six-step discharge and five-step charge process, are unravelled by *in situ* XRD. The $Li_xV_6O_{13}$ unit cell expands sequentially in *c*, *b*, and *a* directions during discharge and reversibly contracts back during charge. The process is associated with a change of occupied lithium sites as well as charge ordering in $Li_xV_6O_{13}$. Density functional theory (DFT) calculations and nuclear magnetic resonance spectroscopy gave further insight into the electronic structures and preferred Li positions in the different structures formed upon cycling, particularly at high lithium contents.

At HT, V_6O_{13} exhibits an even greater capacity, as well as a more symmetric discharge and charge profile. Combining the results from the HT *in situ* XRD study and the DFT calculation, the most Li puckered phase was found to be able to open further along the *b* axis, with a new Li site getting (partially) occupied. The new Li site corresponds to more Li intercalation into the $Li_xV_6O_{13}$ structure and, therefore, more electrode charge storage capacity. The more

symmetric discharge and charge process was attributed to the disappearance of phase 2 (present at room temperature for $1.7 < x \leq 2.1$ in $Li_xV_6O_{13}$) at HT.

Table of Contents

List of Abbreviations

1D	One-dimensional
2D	Two-dimensional
3D	Three-dimensional
AMPIX	Argonne's multi-purpose in situ X-ray
ARC	Accelerated rate calorimeter
Be	Beryllium
CASM	Cluster-assisted statistical mechanics
Cu	Copper
DFT	Density functional theory
DMC	Dimethyl carbonate
EC	Ethylene carbonate
EELS	Electron energy loss spectroscopy
GCPL	Galvanostatic cycling with potential limitation
HRTEM	High-resolution transmission electron microscope
HT	High temperature
IL	Ionic liquid
Li	Lithium
LIB	Lithium-ion batteries
LWD	Logging while drilling
MAS	Magic angle spinning
MWD	Measurement while drilling
Na	Sodium
NCA	$LiNiCoAlO_2$
NMC	$LiNiMnCoO_2$
NMR	Nuclear magnetic resonance
PAW	Projected-augment wave
PBE	Perdew-Burke-Ernzerhof
RT	Room temperature
SEM	Scanning electron microscopy
Si	Silicon
sXRD	Synchrotron X-ray diffraction

VATIC	Variable temperature *in situ* XRD cell
XRD	X-ray diffraction

1 Introduction

This thesis is focused on the high-temperature (HT) performance and phase transformation mechanisms of cathode materials for lithium-ion batteries (LIBs). This introduction summarises important background knowledge on the working mechanism of LIBs, the need to study LIBs at elevated temperatures, as well as two most common open framework structure types of cathode materials. In addition, this chapter gives an overview of the up-to-date knowledge on the two cathode materials studied in detail, namely $LiFePO_4$ and V_6O_{13}. Finally, the objectives of the thesis are summarised.

1.1 Lithium-ion batteries

1.1.1 The basic working principle of LIBs

LIBs are widely applied in our society nowadays and are likely to play an even more important role in the future. The rapid development of LIBs has enabled the mass use of mobile devices and changed people's way of communication and life. This revolution keeps on going with the wider application of LIBs in transport and grid storage.[1,2] Modern LIBs have various components depending on their applications, and they look immensely different. Cell phone batteries are usually small pouch cells; electric vehicles use battery packs that are enclosed in hard shells; energy storage facilities can use containers filled with battery packs.[3] Despite the wide variation in appearance, the basic working principle of LIBs is the same: a typical LIB is a multi-component system with two electrodes separated by the electrolyte (Figure 1.1). Conventionally, the electrodes are termed as follows: the anode is oxidised during discharge, resulting in electrons and ions being released to the external circuit and the electrolyte, respectively.[3] The ions migrate through the electrolyte and are reduced at the cathode, accepting electrons from the external circuit. The electrolyte, being an electronic insulator, is a filter for conveying ionic species, but not electrons.[4] Upon charge, the anode is reduced, and the cathode is oxidised. The redox reactions take place in three forms at the electrodes, i.e., conversion[5], alloying[6], and intercalation[7], among which intercalation is the most common one.[8]

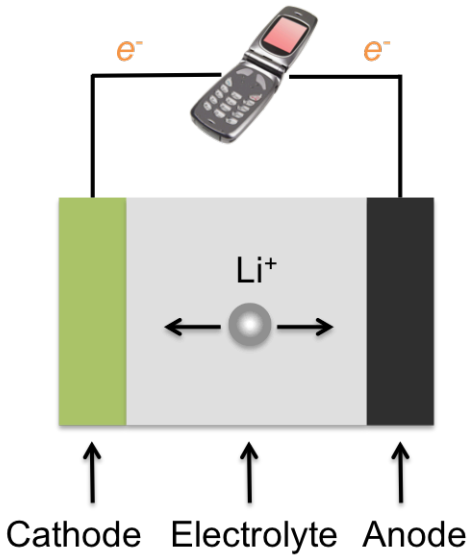

Figure 1.1. A simplified schematic drawing showing the building blocks of an electrochemical cell: cathode, electrolyte, and anode. The Li ions move in the electrolyte and combine with electrons at the cathode or anode during discharge or charge, respectively. The electrons move in the external circuit to powers electronic devices.

A typical LIB uses a pair of intercalation electrodes separated by either a liquid solution of organic solvent and lithium (Li) salt mixture (soaked in polymer or glass fibre separators) or such solution trapped in a gel (Figure 1.2).[9] In commercial batteries, layered graphite is usually used as the anode, while a range of intercalation compounds, such as $LiCoO_2$, $LiFePO_4$, $LiMn_2O_4$, $LiNiMnCoO_2$ (NMC), and $LiNiCoAlO_2$ (NCA), has been used as the cathode Li ions are inserted into and extracted out of the electrodes and shuttle between the two electrodes during the electrochemical process.[10,11]

Ideally, the electrolyte is a chemically inert medium that merely impregnates cathode, anode and the separator to enable ionic transport. However, in most commercial LIBs, a mixture of organic solvents (e.g. alkylcarbonates) is used, typically with Li salts (e.g. $LiPF_6$) dissolved. The energy separation of the lowest unoccupied molecular orbital (LUMO) and the highest occupied molecular orbital (HOMO) of the electrolyte determines the electrochemical stability window.[3] The electrolyte is critical in generating a stable solid electrolyte interface (SEI) between electrode and electrolyte, and plays a key role in cycle life, which is defined as the number of discharge and charge cycles that a battery can sustain while keeping a given percentage of its initial capacity (e.g. 80%).[12,13] For the state of art LIB technology, electrolyte solvents are not stable below 0.8 V and above 4.5 V versus Li+/Li when electrode materials, which are normally strong reducing or oxidizing agents, are present.[14] Consequently, electrolyte degrades at the electrode/electrolyte interfaces,

forming SEI, which is essentially insoluble products passivating both electrode interfaces. The formation of SEI layer often also involve the traces of water impurity and Li salt in the electrolyte.[15,16] With SEI enabling successful operation of the electrolytes outside their thermodynamic stability windows, LIB operation is made possible.[17]

The most important figures of merit of commercial batteries are specific energy and energy density, which correspond to the energy stored per unit mass and per unit volume respectively. Even though a significant amount of the total mass and volume of batteries is dedicated to inactive components, such as the current collectors, electrode separators, shells, the energy that can be utilised in a battery is mostly dictated by the active electrode materials. Therefore, understanding the underlying structural changes and chemistry of the electrodes remains an important and sought-after issue to improve the performance of LIBs.[18]

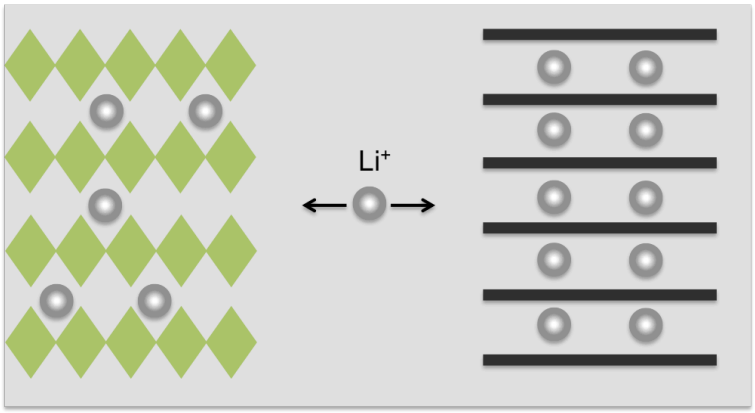

Figure 1.2. LIBs are constructed by two Li-exchanging electrodes separated by a Li-conducting electrolyte in the simplest model. The most common electrode materials are intercalation compounds, such as $LiCoO_2$ (cathode) and graphite (anode), whereas a Li salt in organic electrolyte mixtures (for example $LiPF_6$ in EC/DMC) is mostly used as the electrolyte.

1.1.2 Electrochemical energy storage – basic concepts and terminology

Energy is stored in chemical forms in batteries and reversibly converts to electrical energy in secondary batteries through discharge and charge processes. The amount of energy that electrode materials can store depends on their voltage and capacity.

Voltage

Voltage, or strictly, potential, is an important battery/electrode parameter that is determined by both thermodynamic and kinetic factors. The equilibrium cell voltage, or the open circuit voltage, is determined by the thermodynamics of the electrodes. During actual cycling, however, the actual voltage deviates from the equilibrium value. A major factor that causes the deviation is the impedance.[4] Impedance exists in the transport of electroactive species, i.e., ions and electrons, across the cell, at the solid electrolyte interface, or in the electrode, where solid state diffusion of Li ions takes place.

The thermodynamics of reactions between the electrodes is the driving force for the transport of ions through the electrolyte.

$$\Delta\mu_i = \Delta G_j \tag{1.1}$$

where μ is the chemical potential, *G* the Gibbs free energy. When the cell is in an equilibrium state, there is no net flux of ions in the electrolyte. An electrostatic force, due to the difference in chemical potential between the two electrodes, balances the chemical driving force. Therefore, the energy balance in the single species *i* can be written as:

$$\Delta G_i = -z_i F E \tag{1.2}$$

where ΔG_i is the standard Gibbs free energy change per mol of reaction, z_i is the number of elementary charges that ions of species i carry, *F* is the Faraday constant, and *E* is the voltage between electrodes. This equation expresses the relationship between the chemical and electrical driving forces.

Capacity

Capacity is the parameter that measures the amount of Li being allowed into electrode materials. For intercalation materials with transition metals, charge storage capacity depends on the number of available Li sites and the accessibility of multiple valences in the transition metal in the material. The theoretical capacity of a battery electrode material is calculated by the following equation

$$q = \frac{nF}{3.6M} \quad (1.3)$$

where n is the number of moles of electrons available for electrochemical reaction, F is the Faraday constant and M is the molecular weight of the electrode material. Capacity is conventionally expressed in the unit of mA h/g.

Cycle rate

The current rate is expressed in terms of C rate. A rate of C/n is used, where n is the number of hours required to fully discharge or charge a battery to its theoretical capacity.

Other terms

Other terms that are frequently used in the literature are listed as follows: specific energy, power and capacity denote to the energy, power, and capacity available per unit weight respectively. These are critical parameters for some application, such as vehicle propulsion. As for the energy stored per unit volume, the term energy density is used. This parameter is especially crucial for portable electronic devices.[4]

1.1.3 Various types of cathode materials for LIBs

In addition to high voltage and large capacity, a few more criteria/design parameters need to be satisfied for intercalation compounds to be used as battery electrodes.[3] (1) The crystal structure of the intercalation compound should be preserved over the entire range of Li insertion/extraction to impart reversibility and good cycle life. (2) The compound should support both electronic conduction and Li ion conduction to sustain high current densities, which is required for high power applications. (3) The chemical potential of the electrode for the entire Li composition range should lie within the bandgap of the electrolyte, i.e., above the highest HOMO and below the LUMO level of the electrolyte, such that cathode is chemically stable and non-reactive with the electrolyte. (4) The compound should be relatively inexpensive, lightweight, and environmentally friendly, which is usually fulfilled by the first-row transition metals.

Based on these criteria, research and commercialisation of LIB cathodes mainly focus on compounds of two structural types: the first type generally has close-packed lattice, with transition metal and Li (when present) occupying alternating layers between the anion sheets, for instance, $LiCoO_2$ and NMC material; the other type has more open structures, like many transition-metal phosphates and vanadium oxides. In this thesis, the focus is on the second type of material, namely $LiFePO_4$ (Chapter 1.3) and V_6O_{13} (Chapter 1.4), respectively.

1.2 LIBs at elevated temperatures

1.2.1 The underestimated importance of temperature on LIBs

Even though most battery studies are done at room temperature (RT), the working conditions of real batteries are always at elevated temperatures. LIBs generate heat during cycling, for instance, mobile phones always heat up when being extensively used, which is mostly caused by battery heating. Battery heating, burning, and explosion are hazards of different severity that undermines the development of LIBs industry[14].

Temperature is one of the essential parameters that govern the thermodynamics and kinetics of the heterogeneous LIB system. LIBs are tested using a combination of approaches before being released to the market. The choice of tests is based on the application, manufacture, and standard of the country where batteries are to be used in. Temperature tests, including electrochemical cycling, cycle life testing, and thermal runaway tests are always included in the set of tests in the industry.

However, the number of battery studies carried out at elevated temperatures is much smaller compared with that at RT. There are even fewer studies that provide real-time observation of a working battery. Without knowing the mechanisms properly, researchers and practitioners will never be able to understand how and why a battery works and/or fails. Therefore, being able to monitor and probe battery mechanisms in real time is essential, and its importance is much underestimated at this point.

1.2.2 Growing needs in high temperature secondary batteries for the oil field

In addition to the general need of HT studies of batteries, certain applications, such as oil field batteries, do require special batteries that can sustain these extreme conditions. In the oil and gas industry, batteries have long been used in devices for measurement while drilling (MWD) and logging while drilling (LWD).[19,20] These tools are essential in drilling since they provide field engineers with real-time information on the position and tilt of the wellbore.

At this stage, primary batteries still dominate this market because of the chemistry, such as $LiSOCl_2$, provides sufficient energy density and operates at the required temperatures range experienced in the downhole environment (up to 150^{o}C), simplifying field inventory.[19] However, the $LiSOCl_2$ chemistry suffers fundamental safety issues, which include potential contact of Li metal with water, and cell susceptibility for explosions when externally shorted. Furthermore, replacement of primary batteries causes operation downtime so that, they are

less desirable for use in oil field applications. Field engineers must pull out the battery-containing tool kit well before the batteries run out, which heavily interrupts the drilling operation. Rechargeable batteries can minimise the cost incurred by the operation downtime caused by primary battery replacement since mud turbines can be used for charging batteries. However, most commercially available rechargeable LIBs cannot sustain such a HT. To fulfil the need of downhole rechargeable batteries, materials with high specific and volumetric capacity, moderate cycle voltage and rate performance are highly sought after.

1.2.3 Improving the high temperature performance of LIBs

Improving the HT performance of LIBs requires the most commonly used liquid organic electrolyte being substituted with electrolytes with more suitable properties and forming more stable SEI layers at HT.[21–23] Currently, a selection of binary organic solvent mixtures serves as the standard electrolyte,[24,25] among which the mixture of ethylene carbonate (EC) and dimethyl carbonate (DMC) is the most common combination.[26] These organics are not the ideal solvents for HT batteries operating up to 150^{o}C, as it is shown by the study of Botte et al. that EC decomposes at a temperature around 200^{o}C and DMC in the same temperature range.[27] Especially, the linear carbonates usually have flash points below 30^{o}C and are highly flammable.[17] HT causes the pressure building up inside a cell, due to both the high vapour pressure of organic electrolyte[24] and the exothermic reaction between electrodes and the electrolyte (SEI layer not efficiently passivating electrode surfaces at HT, causing constant reactions between electrodes and electrolyte).[28] The accumulated pressure finally leads to explosions of batteries.

Ionic liquids (ILs)[9], polymers[1], and solid electrolytes[29] are all contenders to replace the liquid organic electrolyte. Both polymer and solid electrolytes are restricted to elevated temperature applications at this moment since Li ion transport in these materials has not yet matched the requirements for RT battery usage. Meanwhile, RT IL has shown some promising results as battery electrolytes.[30–32] Since the scope of this thesis is to compare the electrode phase transition mechanisms at room and elevated temperatures, the electrolyte is better maintained in a liquid state; otherwise, the problems studied might diverge. Therefore, ILs are chosen as electrolyte solvents in this work.

ILs are unique materials composed of only ions in the liquid state at RT.[33] In principle, ILs have large electrochemical windows (greater than 4 V),[34] good thermal stability[9] and low volatility,[35] which make them suitable for HT battery electrolyte. Vijayaraghavan *et al*. used

accelerated rate calorimeter (ARC) to study the exothermic behaviour of some ILs[36] and observed no thermal runaway onset temperature up to 400°C for ILs with a bis(trifluoro-methylsulfonyl)imide (TFSI) anion. The low vapour pressure of IL means that, even at HT, a negligible amount of liquid will evaporate.[35] This low volatility is due to the strong Coulomb interaction between the cation and the anion.

N-propyl-N-methylpyrrolidinium bis(trifluoro-methylsulfonyl)imide, namely [C_3mpyr][TFSI], is a good candidate for HT batteries.[37] Sakaebe *et al*. showed that the electrochemical window of [C_3mpyr][TFSI] is larger than 5 V,[38] sufficient to be used in batteries. [C_3mpyr][TFSI] supports Li electrochemistry[39] and forms a suitable solid electrolyte interphase (SEI), which is key to the stable, long-term cycling of batteries.[40] Howlett *et al*. presented that the pyrrolidinium IL had a Coulombic efficiency greater than 97% after the first five cycles.[41] The cycling performance of [C_3mpyr][TFSI] was first tested in Li/$LiCoO_2$ cells by Sakaebe *et al.* and a severe capacity fade was detected.[38] Howlett *et al*. demonstrated that minimal capacity decay was found in Li symmetric cells, concluding that the capacity fade was related to the $LiCoO_2$ cathode, not the IL.[39,42] The SEI layer on the Li surface was proved to consist mainly of the species decomposed from TFSI anion, which contain LiF, Li_2S, Li_2O, $Li_2S_2O_4$ and Li_2CO_3.[40,42] The principal drawback for [C_3mpyr][TFSI] is its transport properties at RT. It has the same ionic conductivity at elevated temperature (conductivity of 0.65M LiTFSI in [C_3mpyr][TFSI] is 8 mS/cm at 80°C)[43] as does the organic solvent electrolytes at RT (conductivities of 1 M $LiPF_6$ in various carbonate-based electrolytes are within the range of 8 to 12 mS/cm at 20°C).[44,45]

1.3 Phase transformation in $LiFePO_4$ electrodes

$LiFePO_4$ has been one of the most studied commercial cathode materials in the past two decades. Vast knowledge on phase transformation, including the effect of particle size, defects, current applied and temperature has been gained on this material, making it an ideal model compound to test new characterisation techniques. The key findings on $LiFePO_4$ are reviewed in this section, and the problem that remains to be addressed is identified.

1.3.1 Crystal structure and application in LIBs

Since being introduced as a battery cathode material in 1997[46,47], $LiFePO_4$ has attracted immense attention both in academia and industry, due to its normally lower synthesis expense and toxicity[48], and better safety characteristics.[49] The capacity of $LiFePO_4$ battery production exceeds 20 GWh/yr, which makes $LiFePO_4$ a candidate of the most popular

cathode material in LIBs before the Tesla Gigafactory is fully commissioned in the coming years.

The olivine-type $LiFePO_4$ is crystallised in the space group *Pnma*, and its crystal structure is shown in Figure 1.3. Padhi *et al.* studied different iron phosphates and concluded that the relative redox potential of Fe^{3+}/Fe^{2+} against the Fermi level of Li could be tuned by the positions of the polyanions and the Fe^{3+}/Fe^{2+} couple is lowest in $LiFePO_4$, which best suits the criteria of a cathode material.[47] $LiFePO_4$ is delithiated to $FePO_4$, which adopts the same crystal structure with an expansion in the *c* lattice parameter and a shrinkage in the *a* and *b* lattice parameters.[46] $LiFePO_4$ was first characterised to be a low rate material due to its two-phase nucleation and growth reaction mechanism during battery cycling, which is considered as kinetically limited.[46] However, with advances in materials preparation[50–52], $LiFePO_4$ was later recognised as one of the mostly used high rate battery electrode materials. Much work has been done to understand this high-rate, phase-separating material. In the following sections, both thermodynamic and kinetic aspects of the $LiFePO_4$ phase transition and its rate capability will be discussed.

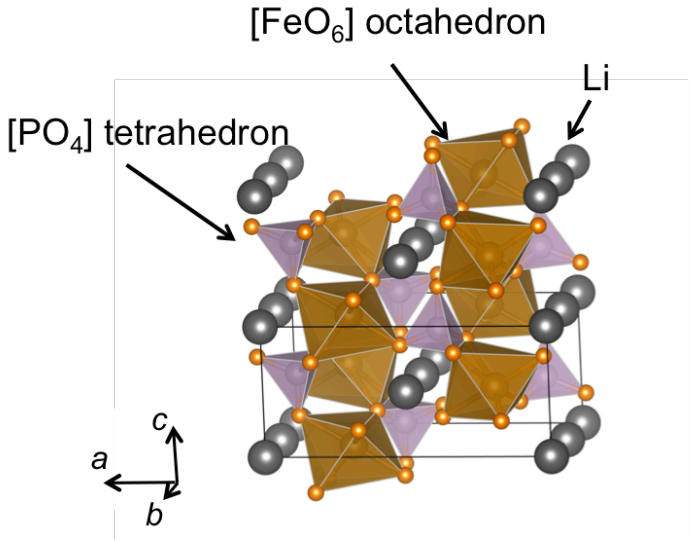

Figure 1.3. Crystal structure of olivine-type $LiFePO_4$ (*Pnma*). Iron, phosphate, oxygen, and Li atoms are represented by brown, purple, orange and grey spheres respectively. The black lines show the unit cell. The V_6O_{13} structure is composed of corner-sharing FeO_6 octahedra and PO_4 tetrahedron.

1.3.2 Electrochemical and thermodynamic aspects

Of all the most commercially used cathode materials, $LiFePO_4$ is unique to having a flat room-temperature voltage curve (Figure 1.4). The other cathode materials, such as $LiMn_2O_4$,[53] $LiCoO_2$[7], NMC[54], and NCA all have sloping voltage profiles due to solid solutions forming over a wide Li composition range.[55] Some of them may contain weak first-order phase transitions that arise from either Li ordering [7] or electronic effects.[56] In the case of bulk $LiFePO_4$, Li has limited solubility in either Li-poor or Li-rich end-member phases.[57] A large miscibility gap is present between the end-member phases. In this phase separating regime, according to Gibbs phase rule, there is no degree of freedom in this two-composition system given a fixed temperature and pressure. The zero-degree freedom results in the aforementioned flat voltage curve of $LiFePO_4$. The partially charged (delithiated) $LiFePO_4$ nano-particles exhibit an inter-particle phase separation configuration, where each $LiFePO_4$ crystallite is comprised entirely of either Li-rich or Li-poor phases.

From an atomic configuration level, the origin for phase separation between the Li-rich and Li-poor phases lies in the interaction of Li^+ vs. neighbouring atoms, as well as the structure of olivine type $LiFePO_4$.[58,59] The very strong attractive force between Li^+ and e^- (Fe^{2+}) outweighs that from the repulsive Li^+ - Li^+ and e^- - e^- interactions, resulting in local ordering of Li^+ and e^-. The geometry of the olivine type structure has twice as many neighbouring Li^+/e^- pairs compared to Li^+/Li^+ pairing, further facilitating phase separation in this material. However, first principles calculations show that the free energy of the solid-solution single phases are only (at most) 15 meV per formula unit above the two-phase, equilibrium state for the same composition over the entire Li composition range, suggesting a small free energy difference between the thermodynamically stable phase separation state and the non-equilibrium solid solution state at RT.[58]

$LiFePO_4$ is commonly used as nanoparticles (less than 100 nm).[60] Equilibrium in a single particle becomes essential discussing the thermodynamics in this scenario. The miscibility gap of $LiFePO_4$ decreases with decreasing particle size. This can be rationalised considering the significant positive energy penalty from the surface and interface between the Li-poor and Li-rich phases in individual particles due to the two-phase coexistence in the same particle.

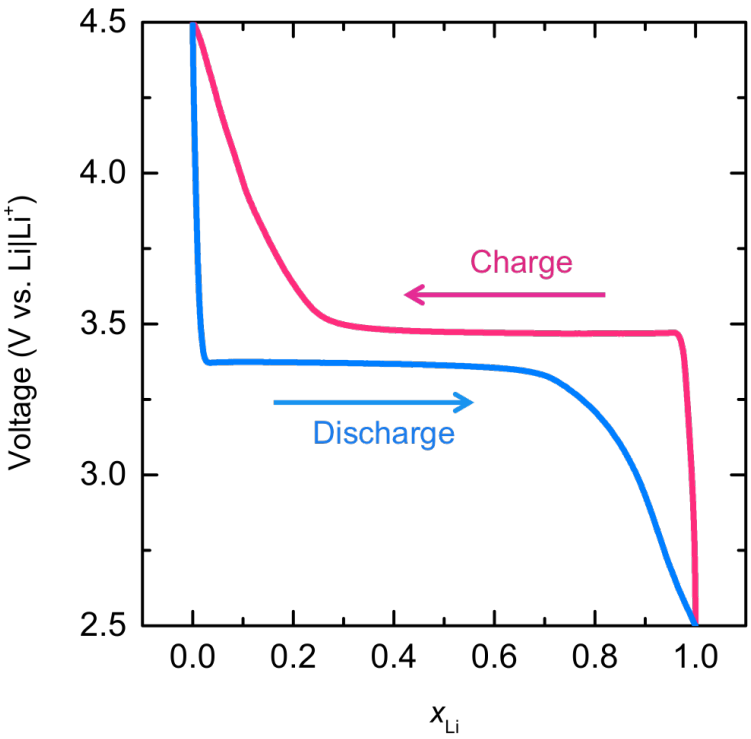

Figure 1.4. Typical charge/discharge voltage profiles of $LiFePO_4$ flat voltage curve, with voltage referenced to the redox potential of $Li|Li^+$. Voltage plateaus, characteristic of two-phase reactions, are observed in both the discharge and charge processes.

Both calculation[58] and experiments[61] have shown that a non-equilibrium, single-phase $LiFePO_4$ has a higher Gibbs free energy than the phase-separated state within the regime of the miscibility gap. When the particle size is significantly reduced, the interfacial energy, surface energy, and coherency strain all make greater contributions to the RT thermodynamic equilibrium of the $LiFePO_4$ system.[62,63] Van der Ven *et al.* have deduced the effects of the energy penalty due to the interface, surface [63] and coherency strain[62] on the free energy of the single particle system to maintain the $LiFePO_4/FePO_4$ interface. Such influence is schematically illustrated in Figure 1.5 as the single-phase (non-equilibrium), inter-particle separation and intra-particle separation scenarios of $LiFePO_4$ and their relevant free energy vs. Li composition are shown. The original miscibility gap of the inter-particle phase separation scenario is for $x_\alpha \le x_{Li} \le x_\beta$. In a single particle scenario, the single phase solid solution state becomes lower in free energy when $x_\alpha \le x_{Li} < x_\alpha'$ and $x_\beta < x_{Li} \le x_\beta'$. Therefore, the RT miscibility gap is reduced and is now at $x_\alpha' \le x_{Li} \le x_\beta'$. Particle size reduction influences the thermodynamics of Li_xFePO_4 and could contribute to the good rate performance of $LiFePO_4$ nanoparticles.

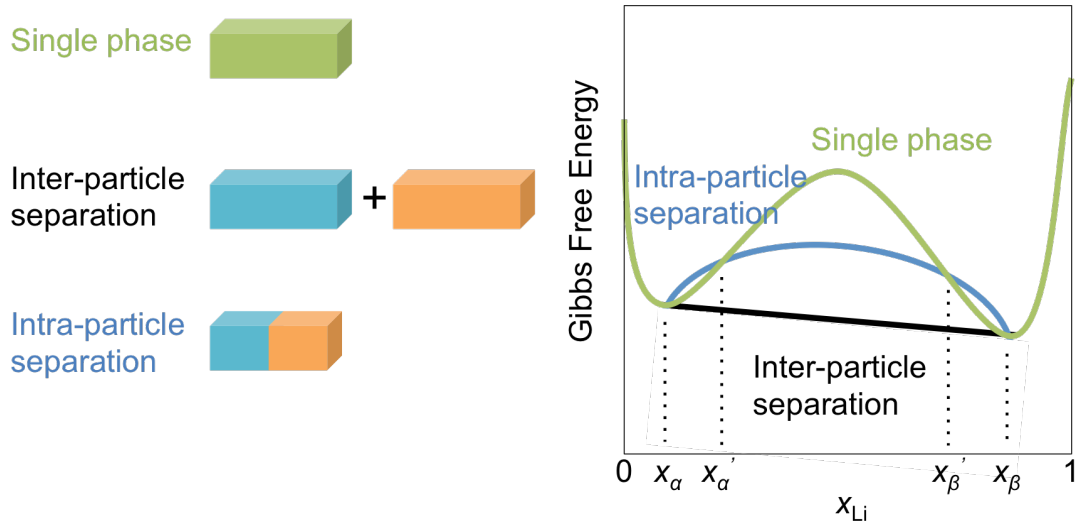

Figure 1.5. Schematic depictions (left) of three states Li_xFePO_4 ($0 \leq x \leq 1$) particles could be in. $FePO_4$ and $LiFePO_4$ particles are represented in cyan and orange blocks respectively; the single phase Li_xFePO_4 particle is described as the green block. The Gibbs free energy diagram of the three states is shown on the right. The green, blue and black curves represent the single phase, intra-particle separation, and inter-particle separation states respectively. The regions of solid solutions are extended when intra-particle separation is present in single particles.

1.3.3 Kinetic aspects

The diffusion of Li in $LiFePO_4$ is one-dimensional (1D), parallel to the *b* direction since the energy barrier for Li to hop between channels is predicted to be very high.[64,65] The electron conduction in the material is carried out by polaron hopping and the intrinsic electronic conductivity is low.[66] The PO_4 tetrahedra between neighbouring FeO_6 octahedra build up a high activation energy barrier along the *a*-axis. Therefore the electronic conduction is restricted in the two-dimensional (2D) *bc*-plane, consisted of FeO_6 octahedra (Figure 1.3). Nishimura *et al.* experimentally visualised the positions of Li ions and observed the 1D diffusion path by measuring the Li nuclear density through neutron diffraction experiment.[67] When defects are taken into account, Li diffusion pathway can be modified[68,69] and becomes particle size dependent.[70] The most common defect in this system is the neighbouring Li-Fe antisite, resulting in Fe^{2+} blocking and changing the 1D Li diffusion pathway.[70] When two such defects coexist in the same 1D channel, the capacity in between becomes blocked.

Both calculation[62] and *ex situ* experiments have demonstrated that intra-particle separation is present and the preferred phase boundary is along the *bc*-plane. When $LiFePO_4$ is cycled at normal conditions and transforms via a two-phase mechanism, the model that best

resembles the real phase transition is the anisotropic one, instead of the isotropic ones, such as the "core-shell" model which was first described by Padhi *et al*.[46] The $LiFePO_4/FePO_4$ interface of partially delithiated $LiFePO_4$ is found to orient along the [010] direction by high-resolution transmission electron microscope (HRTEM)[71,72] and electron energy loss spectroscopy (EELS).[71] The interface aligns along the *bc*-plane, maximising the fully occupied/unoccupied 1D Li channels and minimising the coherency strain energy.[62] However, the insights gained from chemically delithiated $LiFePO_4$ only resemble the single particle scenario at its best. $LiFePO_4$ particles are electronically and ionically isolated during the chemical delithiation, which does not correspond to the interconnected multi-particle scenario present in a cathode in electrochemical cells. The pathway Li^+ and e^- undertake toward/away from $LiFePO_4$ is also different in electrochemical and chemical processes. During electrochemical delithiation, Li^+ and e^- migrate separately within the electrolyte and current collector (to external circuit), while, during chemical delithiation, no inherent Li^+ and e^- separation is present.[73]

In a multi-particle $LiFePO_4$ system, calculations have shown that Li deintercalation in $LiFePO_4$ may proceed via a particle by particle approach.[48] Based on this observation, the most widely accepted phase transformation mechanism is the "domino-cascade" model proposed by Delmas *et al*.[74] In this model, the *bc* phase boundary plane moves quickly in the *a* direction once formed. The phase boundary propagation perpendicular to the *b* axis is energetically favoured over the nucleation from a new site on the same particle. The propagation process is extremely rapid compared to the initial nucleation, which explains the observation that the electrochemically delithiated *ex situ* $LiFePO_4$ samples are two-phase mixtures -- particles being either fully lithiated or delithiated.

1.3.4 Influence of cycling rate on the phase transformation mechanism

The phase transformation pathway of nanoparticulate $LiFePO_4$ changes during high-rate cycling. *Ab initio* calculations have shown that the delithiation of $LiFePO_4$ can proceed via a non-equilibrium single particle solid solution (Li_xFePO_4, $0 < x < 1$) mechanism instead of forming an interface.[58] By bypassing the nucleation event, the phase transformation happens at a much lower overpotential. This non-equilibrium solid solution phase relaxes to the two thermodynamically stable $LiFePO_4$ and $FePO_4$ end phases once the overpotential is removed. Based on this theory, continuum modelling shows that a larger portion of the electrode particles will be in the Li_xFePO_4 ($0 < x < 1$) single-phase state at high rates.[75] Another modelling argues that the dynamic stabilisation of the intermediate solid solution phases within single particles will lead to the absence of $LiFePO_4$ and $FePO_4$ phase

separation.[76] Liu *et al*. used *in situ* synchrotron X-ray diffraction (XRD) to capture the non-equilibrium solid solution Li_xFePO_4 phase and observed its existence during high-rate cycling.[77] Therefore, the exceptional high-rate capability of $LiFePO_4$ nanoparticles is explained by the formation of the non-equilibrium solid solution, bypassing the kinetically limited two-phase nucleation and growth process.

1.3.5 Influence of temperature on the formation of phases

Both computational[78] and experimental[79,80] characterisations have shown a HT solid solution phase that exists beyond a eutectoid transition temperature at 400 — 500K when the composition of x in Li_xFePO_4 is between 0.4 and 0.6 (Figure 1.6). Unlike in a conventional binary phase-separated system, where interactions between unlike species, such as Li^+ and vacancies, are repulsive, the localised 3*d* electrons in $LiFePO_4$ influence the interactions. In section 1.3.2, the ion interactions below the eutectoid point are discussed. At temperatures above the eutectoid point, first principle calculation shows that the increased disorder of Fe^{2+} and Fe^{3+} results in decreased Li^+ coalescing and diluting the number of Li^+/e^- pairs, supporting a solid solution formation instead of separated phases.[78] Ellis *et al.* also measured the electron hopping rates between Fe sites in the HT solid solution phase and found the rates to be substantially higher than those of the two end $LiFePO_4$ phases at RT.[81] Notably, the HT solid solution phase shows local ordering of Li and vacancies on a very limited length scale of a few Angstroms[82], being not totally random.[58] The HT solid solution phase that is quenched to RT is found to be stable in a few experiments for an extended period of time[60,80,83], suggesting once again that the thermodynamic driving force for the solid solution Li_xFePO_4 to phase separate is weak.

Below the eutectoid temperature, the phase diagram shows that Li_xFePO_4 will always consist of two phases. However, because the phase transition pathway at RT changes during high rates of cycling, it would be of interest to know whether the current-induced solid solution mechanism still dominates at elevated temperatures. Studies on the HT cycling of $LiFePO_4$ has so far focused on the cycling performance,[84–90] insights into the material phase change mechanism remain needed.

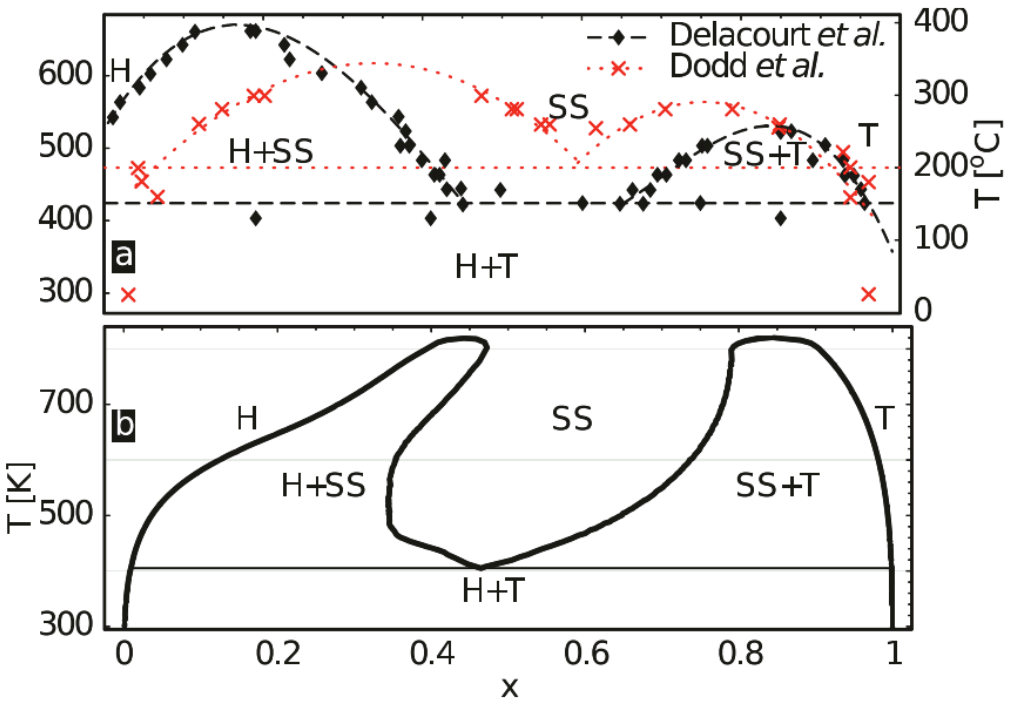

Figure 1.6. Phase diagrams of bulk Li_xFePO_4, determined experimentally by Delacourt *et al.*[79], Dodd *et al.*[80], and computationally by Zhou *et al.*[78] All three show a solid solution phase at an elevated temperature that is present beyond a eutectoid transition temperature between 400 and 500 K. Reprinted with permission from Ref[48], copyright Electrochemical Society 2013.

1.4 Vanadate materials: high capacity due to multivalence

Compared with $LiFePO_4$, the vanadium oxide batteries always have a lower cell voltage, but a larger capacity due to the multiple valence states bestowed by V^{5+} species. For a long time, vanadates attracted attention from the battery research community due to their high capacity and potentially high energy density.[91–96] Even though much of the research interest has been recalibrated on the high voltage materials and their application in LIBs, in areas where Li metal anode can be applied, and high capacity is desired, especially in batteries for HT applications, such as Li polymer batteries and all solid-state batteries, vanadate materials still have a large market for both research and industry.

1.4.1 V_2O_5 and other vanadates

V_2O_5 has been studied for more than 40 years and is the most well-studied vanadium oxide material.[97,98] It has a layered structure and is known to react with Li by an intercalation mechanism:

$$xLi + V_2O_5 = Li_xV_2O_5 \quad (1.4)$$

The crystal structure of pristine V_2O_5 can be described by an orthorhombic unit cell, (space group *Pmmn)* with unit cell parameters of $a = 11.512$ Å, $b = 3.564$ Å, $c = 4.368$ Å, (Figure 1.7).[98] The local structure of V^{5+} in V_2O_5 can be viewed as being in an off-centred position in a VO_6 octahedron (Figure 1.7).[96] Because V^{5+} has a d^0 configuration, the crystal field is very Jahn-Teller distorted. Along the *c* direction, the bond length of the shorter axial vanadyl bond is only 1.576 Å long, while the equatorial ones can be as large as 2.793 Å long. Infrared absorption frequency indicates that the short bond corresponds to a double bond.[98] The strength of the long bond is usually considered to be weak, so the vanadium oxide polyhedron is often described as a square pyramid. The VO_5 square pyramids alternate in an up-up-down-down sequence in one layer.

The lithiation process of V_2O_5 traverses a few different phases, as the voltage profile shows various plateaus and steep steps. Upon initial lithiation, about 1% of Li intercalates into the crystalline V_2O_5 to form α-$Li_xV_2O_5$ ($0 < x < 0.04$), where the host V_2O_5 structure remains intact.[99] The 3.4 V plateau reflects the α and ε phase two-phase reaction, and the ε phase is characterised to be for $0.35 \leq x < 0.7$.[95] The ε phase has increased puckering of the vanadyl layers, compared to the α phase [100] The material evolves through another two-phase region, corresponding to the 3.2 V plateau on the discharge curve.[101] The voltage drops precipitously to almost 2.5 V while the material is lithiated to the δ phase, which undergoes reversible layers gliding. Irreversible phase transformation happens at more than 1 Li per formula unit of V_2O_5 when the material evolves to the γ phase via a gradual two-phase nucleation and growth process during the 2.4 V plateau on the discharge profile.[102] The vanadium-oxygen bonds are broken in the γ phase to accommodate more Li intercalation. The square pyramids alternate in an up-down-up-down order in this phase and the layers are severely puckered.[103] The γ phase itself can be reversibly cycled, leading to an increase in cell voltage during the first part of discharge ($0 \leq x < 1$) compared with original V_2O_5.[104] The material can be further reduced to *ω*-$Li_3V_2O_5$, the formation of which corresponds to the 2.1 V voltage plateau.[105] Once formed, the material can be cycled in a large Li composition range via a wide solid solution process, reflected by the sloping voltage profile (lack of step-like feature) in Figure 1.8.[106] During charge (delithiation) of the *ω*-$Li_3V_2O_5$ phase, the voltage profile becomes increasingly steep with increasing level of delithiation, even exceeding 4 V when the material is delithiated to $Li_{0.1}V_2O_5$. Extraction of the remaining Li in the structure is very difficult by electrochemical approaches. Previous XRD study shows that the *ω* phase formed at the end of charge is completely different from all previous phases evolved during discharge and following charge process. The *ω* phase that is formed at the end of first

discharge can be indexed to a tetragonal crystal system with unit cell parameters of a = 9.2 Å, and c = 4.1 Å.[102] During the second electrochemical cycle, some of the diffraction peaks disappear and the crystal structure can be indexed to a cubic one with a = 4.1 Å, characteristic of a rock-salt type structure. Delmas attributed the high voltage of the low Li content ω phase to a highly defective rock-salt lattice, containing up to 60% vacancies on the cation sublattice.[94,104]

Other vanadium oxide materials, for instance, VO_2, V_6O_{13}, V_7O_{16}, and $Li_{1+x}V_3O_8$,[107] all have rich chemistries and are potential LIB cathode material. Chernova *et al*. have done a throughout review of vanadium oxide materials and their application in LIBs. Because of the high capacity, stable crystal structure, and good electrochemical performance, V_6O_{13} is one of the leading candidates for cathode materials.

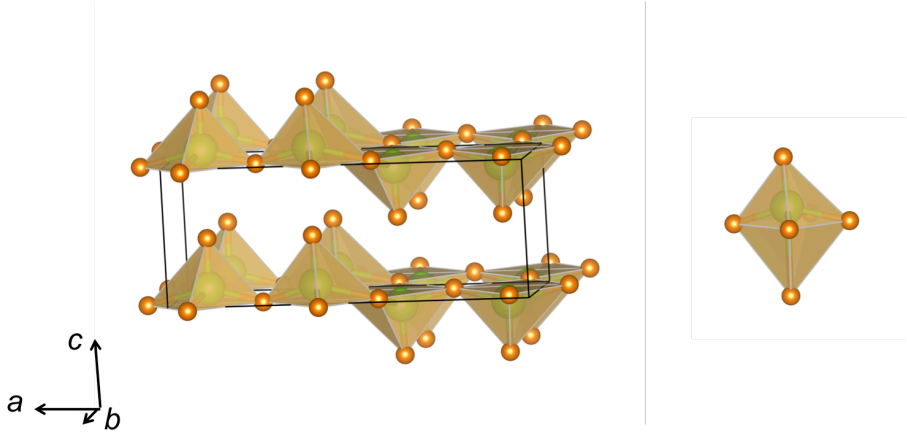

Figure 1.7. Crystal structure of orthorhombic V_2O_5 (*Pmmn*). One single vanadium with its neighbouring oxygen atoms is shown on the right, displaying the distorted octahedral environments (shown as square pyramids in the unit cell). Vanadium and oxygen atoms are represented by green and orange spheres respectively. The black lines show the unit cell. The V_2O_5 structure is composed of two layers of VO_5 square pyramids that alternate in an up-up-down-down sequence in the *ab*-plane.

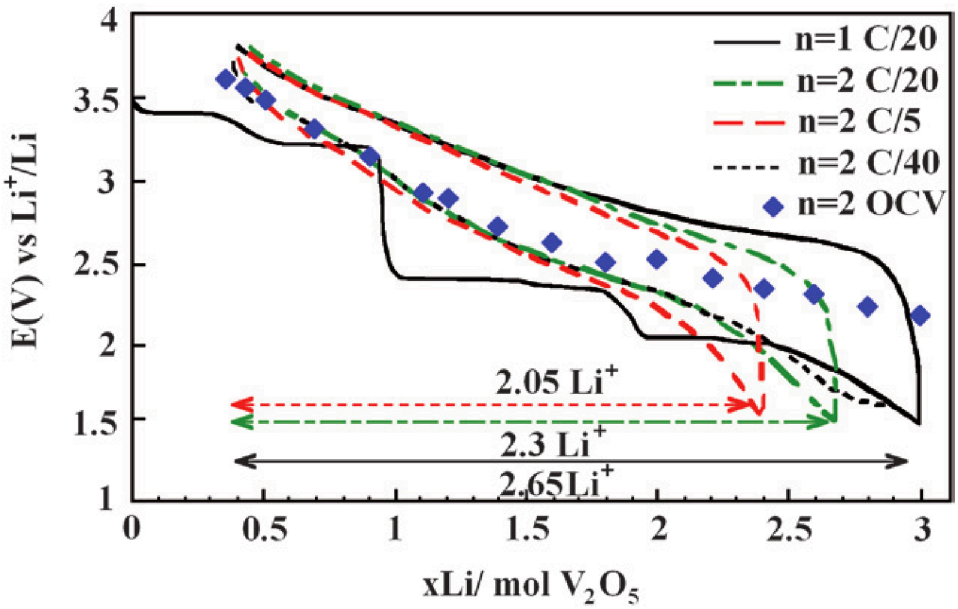

Figure 1.8. Electrochemical cycling of V_2O_5 (black lines) and ω-$Li_3V_2O_5$ (coloured and dashed lines at subsequent cycles and various rates). Reprinted with permission from Ref[106], copyright Electrochemical Society 2006.

1.4.2 V_6O_{13}

V_6O_{13} has been studied over the last 30 years as a battery cathode for rechargeable Li polymer batteries due to its high specific capacity, low cost and wide availability.[92,96,108–111] It has a theoretical capacity of 417 mAh/g,[112] corresponding to 8 Li per formula unit (vanadium being reduced from an average formal charge of +4.33 to +3), and a theoretical energy density of 890 Wh/kg.[113] Both stoichiometric and slightly oxidised V_6O_{13+y} with $y \leq 0.2$ have been prepared, resulting in differences in the maximum Li uptake and electrochemical capacity.[114] Chernova *et al*. suggested that the capacity is limited by the electron count, rather than the availability of Li intercalation sites.[96] West *et al*. were able to cycle V_6O_{13} in a prototype polymer battery for more than 130 cycles at 155°C, which demonstrates its suitability to be used as a HT secondary battery cathode material.[113] In recent years, different V_6O_{13} nano-sized structures with different morphologies were fabricated to enhance performance at high rates and capacity retention after many cycles.[115,116]

Crystal structure of V_6O_{13}

Extensive efforts have been made to understand the discharge mechanism of V_6O_{13} using crystallographic approaches. The crystal structure of V_6O_{13} was first studied by Aebi in 1948[117] and further refined by Wilhelmi *et al*. in 1971.[118] These studies show that V_6O_{13} is

monoclinic (space group *C*2/*m*) with unit cell parameters of *a* = 11.922(2) Å, *b* = 3.680(1) Å, *c* = 10.138(2) Å, and *β* = 100.88(1)°. The crystal structure comprises edge- and corner-sharing, distorted VO_6 octahedra, which form alternating single and double VO_x layers connected via shared corners (Figure 1.9). It should be noted that although it is convenient to discuss the crystal structure in terms of single and double layers, the structure is fully connected in three dimensions (3D). In particular, V_6O_{13} is not a 2D layered structure, which is adopted by many intercalation materials with strong bonding within layers and weak interactions between layers.

V_6O_{13} contains three crystallographically distinct vanadium atoms, V(1), V(2), and V(3), (Figure 1.9), with an average vanadium formal charge of $V^{4.33+}$. The valence state of V(1), V(2) and V(3), as estimated by Wilhelmi *et al.* are 4.20, 4.67, and 4.37, respectively, suggesting that the V^{5+} centres are mainly located in the $V(2)O_6$ octahedra.[118] In 1998, Bergström *et al.* performed a deformation electron density refinement on single crystal data and also assigned the oxidation state of V(2) to +5, based on the assumption of a simplistic model of integer oxidation states.[119] V_6O_{13} is metallic at RT but becomes less conductive upon lithiation.[113,120]

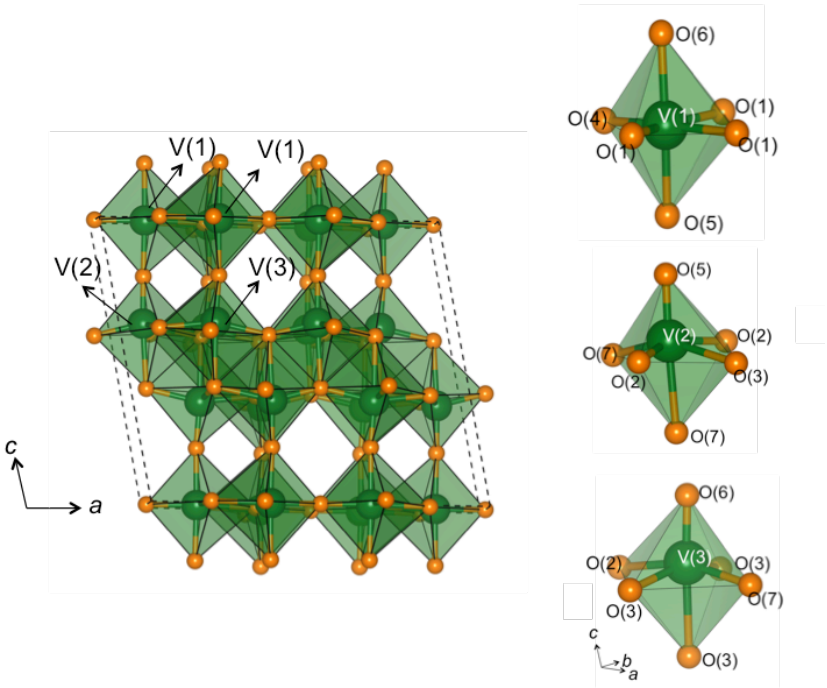

Figure 1.9. Crystal structure of monoclinic V_6O_{13} (*C*2/*m*). The three crystallographically non-equivalent vanadium sites in V_6O_{13} are shown separately, displaying the distorted octahedral environments. Vanadium and oxygen atoms are represented by green and orange spheres respectively. The dashed lines show the unit cell. The V_6O_{13} structure is composed of layers of edge- and corner-sharing distorted VO_6 octahedra that are stacked along the *c* axis. Infinite channels extend along the *b* axis and may facilitate intercalation and accommodation of Li ions.

Structural changes/phase transformation during lithiation of V_6O_{13}

When discharging V_6O_{13} as a cathode against a Li anode, the discharge curve shows various voltage plateaus corresponding to different $Li_xV_6O_{13}$ phases formed by Li ions intercalating in between the VO_6 slabs.[93,113] Several research groups have carried out detailed investigations to understand the intercalation mechanism. Impedance spectroscopy studies of different single crystal surfaces performed by West *et al*. showed that Li ion diffusion into single crystal V_6O_{13} is a 1D process along the *b* axis.[109] In 1992, Gustafsson *et al*. used *in situ* XRD to monitor the structural changes of V_6O_{13} in a polymer battery during discharge.[111] They observed substantial changes in both peak positions and intensities but reported only minimal details on the structural changes. Further single crystal XRD studies were performed on V_6O_{13},[119] as well as the Li-enriched phases $Li_{0.67}V_6O_{13}$,[121] LiV_6O_{13},[121] $Li_2V_6O_{13}$,[122] $Li_3V_6O_{13}$,[123] and $Li_{3.25}V_6O_{13}$,[124] which showed that Li ions occupy the Li(1) position (Figure 1.10) and form a square pyramidal coordination with the neighbouring oxygen atoms in $Li_xV_6O_{13}$ when $x \leq 2$. The Li(1) site is partially occupied in both $Li_{0.67}V_6O_{13}$[121] and LiV_6O_{13}[121], but long range ordering of the Li ions and vacancies occurs resulting in superstructures of the original V_6O_{13} phase. The Li(1) sites are fully occupied in $Li_2V_6O_{13}$, further Li insertion into the crystal structure resulting in a rearrangement of the Li ions to occupy sites in both the single and double layers (i.e., Li(3) and Li(4)). In 2001, Braithwaite *et al.* used a combination of classical pair potential method and density functional theory (DFT) to identify Li intercalation sites.[125] These calculations indicate that there are (at least) four sites within the cavities between the single and double layers (Figure 1.10), which includes the Li(1), Li(3) and Li(4) sites observed in the single crystal studies and one additional site, Li(2).

There is no structural information on the lithiated phases beyond $Li_{3.25}V_6O_{13}$, even though further lithiation to $Li_7V_6O_{13}$ is possible.[93] Schmitt *et al.* used soft X-ray absorption spectroscopy[126] and soft x-ray emission spectroscopy[127] to study the Li insertion, especially beyond $Li_3V_6O_{13}$, and found that $Li_4V_6O_{13}$ and $Li_5V_6O_{13}$ may be composed of two phases. Furthermore, the charging mechanism of V_6O_{13} remains unknown. An understanding of the whole series of structural changes of V_6O_{13} during discharge and charge underpins future studies aimed at improving the performance of this material in a LIB. Also, as a HT cathode material, the HT performance and the phase transition mechanisms of V_6O_{13} remains to be understood.

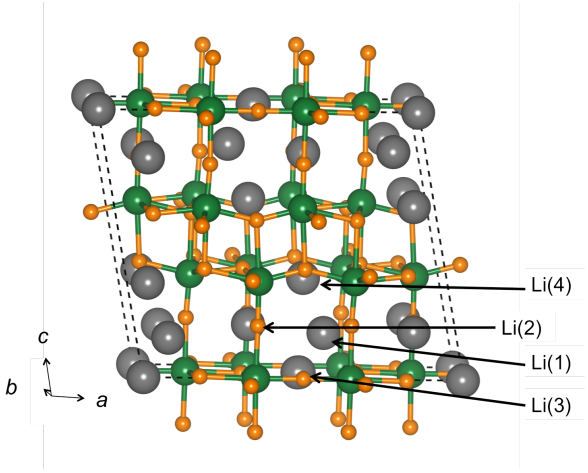

Figure 1.10. Possible Li intercalation sites in V_6O_{13} unit cell calculated using a combination of classical pair potential and DFT methods.[125] Vanadium, oxygen and Li atoms are represented by green, orange and grey spheres, respectively. Four possible low defect-energy Li sites were predicted in the V-O cavity; Li(1) is the lowest energy site, and the only site observed in previous single crystal studies of $Li_xV_6O_{13}$ for $x < 2$.[122,123,125]

1.5 Objectives of the thesis

This thesis aims to study $LiFePO_4$ and V_6O_{13} cathodes for LIBs at elevated temperatures by *in situ* synchrotron XRD (sXRD). The insights into the structural changes and working mechanisms are likely to address performance and safety issues of LIBs at HTs, which are inevitable in daily usage. This work is benchmarked by three objectives:

- Development of an HT *in situ* sXRD setup (Chapter 3)

  To study phase transition mechanisms of electrode materials at HTs, a technique that allows real-time investigation spanning a wide temperature range is needed. Currently, no *in situ* devices fulfil the temperature range of up to 150°C. Therefore, a new VT *in situ* battery characterisation setup should be developed first. The setup aims to utilise synchrotron XRD, a proven technique for real-time investigation of reactions in batteries. The high-flux synchrotron beam allows XRD pattern to be collected within seconds to allow time-resolved studies during battery discharge/charge.

- Application of this setup in HT sXRD studies on $LiFePO_4$ in LIBs (Chapter 3)

  Even though $LiFePO_4$ is deeply studied, the phase transition mechanism during high rate cycling at HT has not been studied before. With the development of the new HT in situ sXRD setup, the HT mechanisms are studied for the first time.

- *In situ* sXRD studies on V_6O_{13} (Chapter 4 and Chapter 5)

V_6O_{13} is a high capacity electrode material and promising candidate for LIB cathodes. However, its complex electrochemistry remains only partially understood throughout the past three decades. *In situ* synchrotron XRD is performed on V_6O_{13} at both RT and HT to study its complex (de)lithiation mechanism during discharge/charge. The real-time study is complemented by DFT calculations and solid-state nuclear magnetic resonance (NMR) investigations to gain insights into the crystal structures, electronic properties, and phase transformation mechanisms for the various $Li_xV_6O_{13}$ at RT (Chapter 4) and HT (Chapter 5).

2 Experimental

2.1 Material preparation

All the electrochemistry tests, including the *in situ* XRD tests, in this thesis, are performed in batteries with pellet-form cathodes, liquid-form electrolytes, glass fibre separators (Fisher Scientific) and Li anodes.

2.1.1 Cathode

$LiFePO_4$ synthesis

$LiFePO_4$/carbon composites (mean particle sizes 170 nm) were synthesized using the solid-state method developed by Kobayashi *et al*.[128] Mixtures typically of 1.11 g lithium carbonate (Li_2CO_3 Aldrich 99.997%), 5.36 g iron(II) oxalate dehydrate ($Fe(II)C_2O_4 \bullet H_2O$ Aldrich 99%), 3.44 g ammonium dihydrogen phosphate ($NH_4H_2PO_4$ Aldrich 99%) and 0.52 g Ketjen black (EC-600JD AkzoNobel) were high-energy ball-milled for 60 mins into homogeneous powder precursors. The precursors were pressed into pellets (13 mm diameter, 5 mm thick, applied loads of 0.9 tons) and sintered at 600^{o}C for 6 hours under high purity flowing Ar gas.

V_6O_{13} synthesis

The starting material V_6O_{13} (99.6%, 20 mesh) was purchased from EVRAZ Stratcor, Inc., USA. This material was thermally annealed at 500^{o}C under Ar for two hours, to decrease the amount of other vanadium oxide impurities and increase crystallinity (Figure 2.1). The thermally annealed V_6O_{13} sample was reported to have better cycle life performance and more clear features of stepwise electrochemistry.[129]

The annealed V_6O_{13} particulates are plate-like crystallites as seen by scanning electron microscopy (SEM, Hitachi S-5500 field emission) with the long side in a dimension of submicron to micron size and the short side shorter than 50 nm (Figure 2.2).

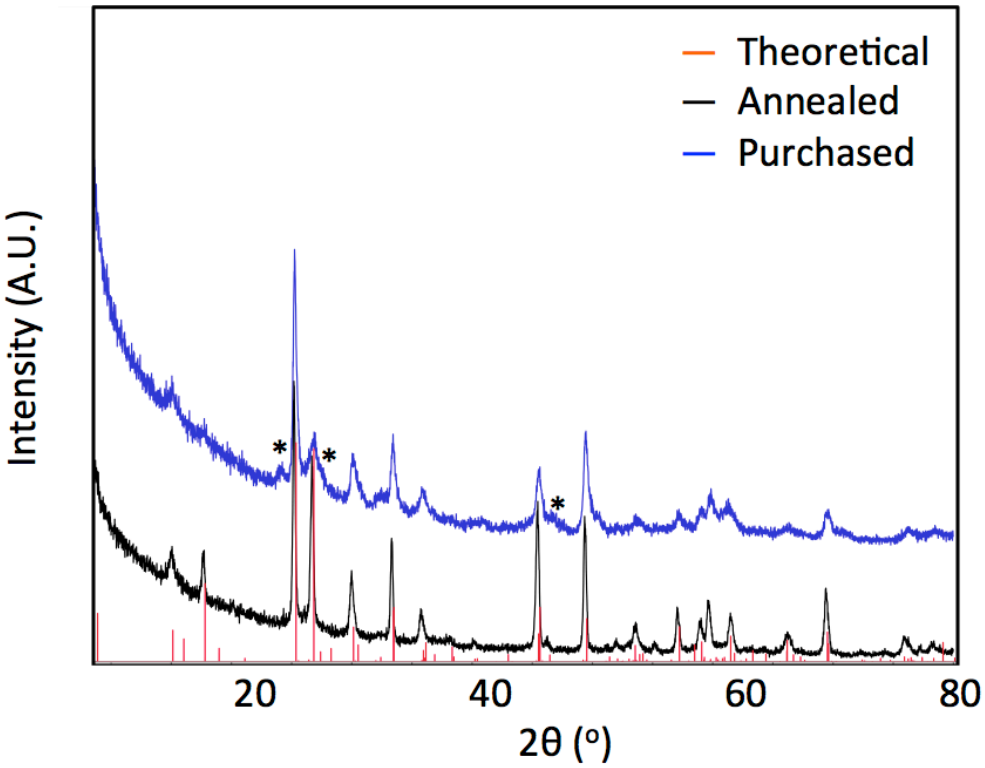

Figure 2.1. Powder XRD patterns of the purchased (blue) and annealed (black) samples. The patterns are aligned with the theoretical V_6O_{13} reflections calculated based on the single crystal data reported by Bergström, *et.al.*[119] The most prominent impurity phases are highlight by black asterisks. Crystalinity is found to be much improved in the annealed sample as the relection peaks are much sharper.

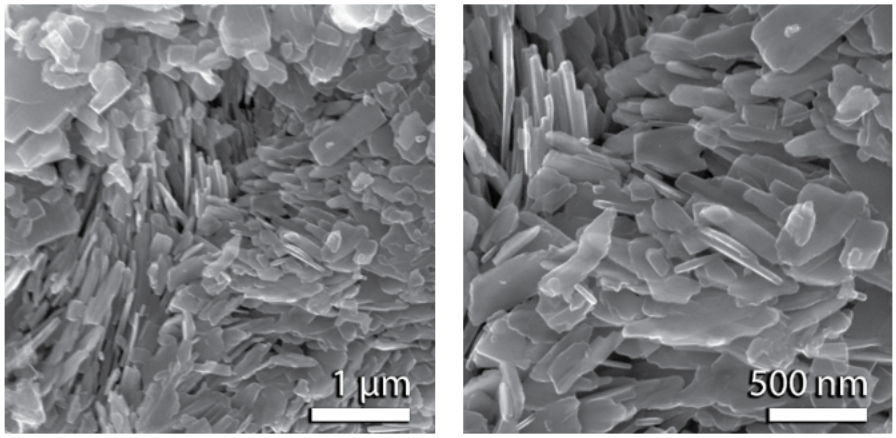

Figure 2.2. SEM picture of the ground V_6O_{13} powder (direct imaging, i.e., no coating) reveals the thin plate-like morphology of the individual crystallites, which leads to preferred orientation effects in the XRD patterns. Dr. Tao Liu (Department of Chemistry, University of Cambridge, UK) is gratefully acknowledged for taking these SEM images with a Hitachi S-5500 field emission SEM.[130]

Powder cathodes

For experiments benchmarking the electrochemical performance of the newly designed HT in situ XRD battery investigation setup (see Chapter 3), the as synthesised $LiFePO_4$/carbon composites were used.

Pellet cathodes

For all *in situ* experiments, $LiFePO_4$ (approximately 7 mg) was mixed with Super P carbon (Alfa Aesar), carbon Ketjen black (EC-600JD AkzoNobel) and polytetrafluoroethylene (PTFE) binder (Sigma-Aldrich) in the mass ratio of 3:3:3:1 and pressed into pellets (13 mm diameter, 230 µm thick, applied pressure of 12 MPa). The large amount of carbon was added to enable high rate cycling.[77]

For RT experiments, V_6O_{13} (approximately 15 mg) was mixed with Super P carbon (Alfa Aesar), carbon Ketjen black (EC-600JD AkzoNobel) and polytetrafluoroethylene (PTFE) binder (Sigma-Aldrich) in a mass ratio of 6:1.25:1.25:1.5 and pressed into pellets (13 mm diameter, 190 µm thick, applied pressure of 12 MPa).

For HT experiments, V_6O_{13} (approximately 7 mg) was mixed with Super P carbon (Alfa Aesar), carbon Ketjen black (EC-600JD AkzoNobel) and polytetrafluoroethylene (PTFE) binder (Sigma-Aldrich) in the mass ratio of 3:3:3:1 and pressed into pellets (13 mm diameter, 230 µm thick, applied pressure of 12 MPa). The larger amount of carbon is added to enable cycling with IL at HT.

2.1.2 Electrolyte

A mixture of Li salt and the organic solvent was used as the electrolyte for electrochemical experiments from 25°C to 75°C, and a mixture of Li salt and IL was used for experiments from 75 to 150°C. An amount of approximately 25 mL electrolyte per gram active material was used in the electrolyte for RT low rate tests, i.e. pellets with 60% active material. This amount was doubled for HT or high rate experiments.

Organic electrolyte

The organic electrolyte 1 M $LiPF_6$ in 1:1 EC : DMC (LP30) electrolyte was purchased directly from Sigma-Aldrich and used between 25°C and 75°C.

$LiPF_6$ was used as the Li salt, because it is highly soluble and stable in alkyl carbonate solvents and forms high conducting electrolytes.[26] However, the low thermal stability[131] and high susceptibility for hydrolysis[132] pose significant issues for $LiPF_6$ use at HT. At HT, $LiPF_6$ readily decomposes into LiF and PF_5.[17] As PF_5 is in a gas form, the accumulation of the gas phase results in a pressure rise in the battery that could ultimately cause hazards, such as explosion and releasing toxic gases.[131]

The EC and DMC mixture is the most commonly used organic solvent[26] but is only used between RT to 75°C in this study. Because of the low decomposition temperatures and high volatility,[24,25] it is not the ideal solvent for a HT battery normally operating up to 150°C, with a potential of going to 200°C. Instead, an IL electrolyte was used.

IL electrolyte

LiTFSI (99.9%) salt and [C_3mpyr][TFSI] (99.95%) IL solvent were purchased separately from 3M and Solvionic. LiTFSI and [C_3mpyr][TFSI] were vacuum-dried at 150°C and 25°C respectively for three days before mixing into the IL electrolyte (0.5 mol/kg LiTFSI in [C_3mpyr][TFSI]).

LiTFSI was used as a replacement of $LiPF_6$ above 75°C because of its good thermal stability. Thermogravimetric analysis (TGA) performed by Sloop *et al*.[131] found no weight loss at 300°C, while isothermal TGA on solid $LiPF_6$ showed evidence of decomposition at 50°C.[133] LiTFSI is also more conductive than $LiPF_6$ in the same binary solvent 1 M EC/DMC (1:1, wt:wt).[134].

2.1.3 Anode

Li ribbon

Li metal ribbon was purchased from Sigma Aldrich and disks of ½ inch diameters were cut and used as the anode in all electrochemistry experiments. Li provides the highest specific energy of all anode mateirals.[11,39] The principle of using an elemental Li anode is simple, for it in principle only involves extracting Li from the anode upon discharging, and electrodepositing Li from the electrolyte onto the anode surface upon charging.

2.2 Electrochemistry

2.2.1 Galvanostatic cycling

Galvanostatic cycling with potential limitation (GCPL) was the electrochemistry testing technique used in this study. A constant current is applied to the battery with limitations on the maximum/minimum of potential. The cell is either discharged or charged to a set potential limit. Then it stops or goes to the next sequence based on the program setup.

2.2.2 Battery assembly configurations

In work included in this thesis, all electrochemistry experiments are tested in either coin cells or Swageloks, unless elsewhere indicated.

Coin cells

Coin cells are made of eight parts, including three battery parts: cathode, electrolyte soaked separator, and anode, and five coin cell casings: a top casing, a spring, a gasket (plastic O-ring), one or two disks as current collectors, and a bottom casing (Figure 2.2). These parts are stacked together and pressed into an airtight button cell. The anode and cathode materials are in contact with the stainless steel top and bottom casings, electrically insulated by the gasket, which also seals the battery. The stainless steel spring is added to provide mechanical pressure inside the cell.

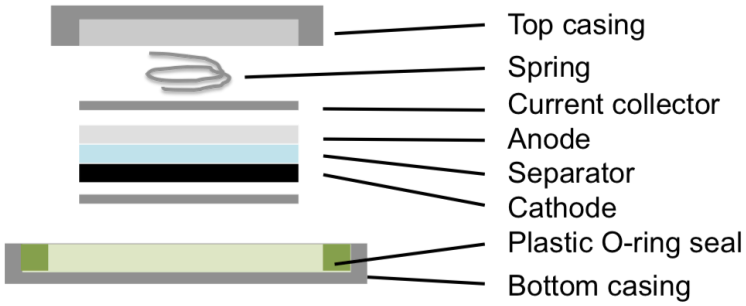

Figure 2.3. Schematic of a coin cell configuration. The top and bottom casings are in contact with the anode and cathode of the battery respectively. An electrolyte soaked separator separates the battery cathode and anode. A plastic gasket insulates the top and bottom casings from each other. The casings, spring, and current collector are all made of stainless steel. Coin cell is one of the most commonly used cell designs in battery research. The coin cell components are not reusable.

Swagelok cells

Swagelok cells consist of 14 parts, including three battery parts: cathode, electrolyte soaked separator, and anode, and 11 Swagelok casings: two plungers, two hexagonal nuts, two sets of front and back ferrules, a piece of Polyimide film, a spring, a pellet, one or two disks and a cell body (Figure 2.3). Each electrode consists of one plunger, one nut, one disk and one set of ferrules. The bottom electrode is in direct contact with the cathode, and the top electrode is in contact with the spring and pellet, which reaches out to the anode. These two electrodes and the cell body (with the inner surface covered by a sheet of polyimide film) together enclose the battery. The ferrules are made of plastic, sealing the cell and insulating the two electrodes.

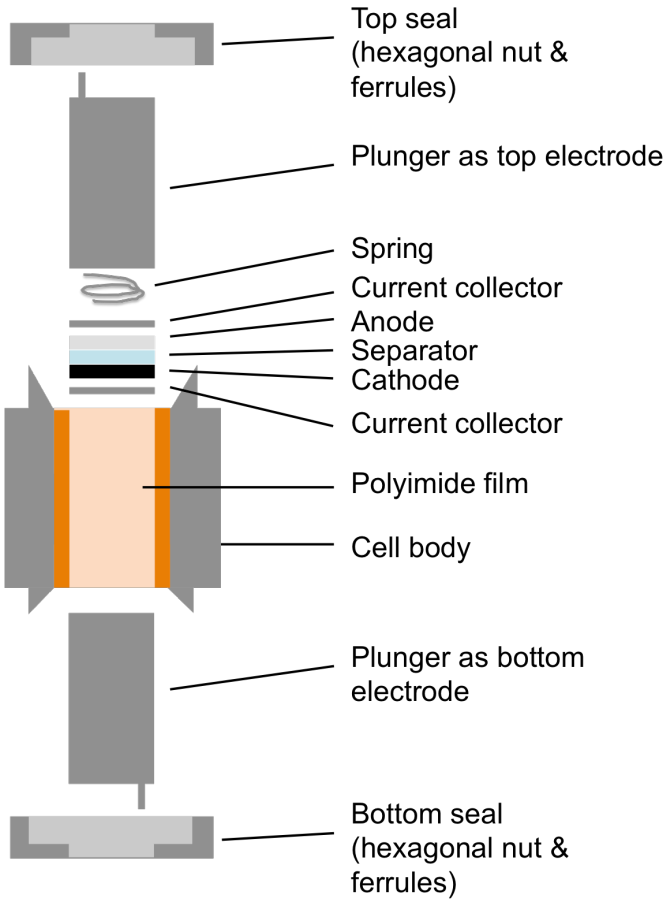

Figure 2.4. Schematic of a Swagelok cell configuration. The two plungers are used as top and bottom electrodes that are in contact with the anode and cathode of the battery respectively. An electrolyte soaked separator separates the battery cathode and anode. A cell body and two sets of nuts and ferrules enclose and seal the battery. The inner surface of the cell body is covered with a sheet of polyimide film to present short-circuiting when the battery is assembled. The plungers, nuts, spring, cell body and current collectors are all made of stainless steel. The Swagelok components are reusable.

2.3 X-ray diffraction

2.3.1 *Ex situ* XRD

RT *ex situ* XRD experiments were conducted on a PANalytical powder diffractometer, on a spinning sample stage with an X'celerator CCD detector. The source was CuK_α radiation. Goniometer scans were done in the range $5^o \leq 2\theta \leq 80^o$, with a step size of 0.0167^o 2θ. Air sensitive $Li_xV_6O_{13}$ (x > 0) samples were sealed between two polyimide films with polytetrafluoroethylene-O-rings. VT *ex situ* XRD from RT to 250°C was performed in a HT furnace with hot inert gas as the environment and heating source.

2.3.2 *In situ* synchrotron diffraction

RT *In situ* synchrotron XRD data on V_6O_{13} were acquired in transmission geometry at beamline 17-BM of the Advanced Photon Source at Argonne National Laboratory (wavelength 0.7295 Å, 500 µm diameter beam), using a 2D area detector (Perkin-Elmer).

Before the *in situ* experiments, polyimide capillaries containing a NIST LaB_6 standard, the active material, carbon additive, and PTFE binder were measured separately. The measurements of the active material were used to calibrate the position of the *in situ* cells before *in situ* experiments. The other measurements were for refinement purposes (section 2.3.3).

In situ measurements were performed at a sample-to-detector distance of 300 mm. Each pattern was collected for 10 seconds. The AMPIX electrochemical cells were used in this experiment as described in more detail elsewhere.[135] Six cells were placed in a flat 2 x 3 stainless steel multi-cell holder, which moved 2D to take XRD measurements of the six cycling cells in a subsequent order. This allowed more effective use of the beamtime and reduced the amount of excessive data generated for low rate cycling, as the cells were cycled at C/10 (low rate) using an external electrochemical cycler (Maccor).

HT *in situ* synchrotron XRD on $LiFePO_4$ and V_6O_{13} were done in transmission geometry at beamline I11 of Diamond Light Source (wavelength 0.825868 Å, spot size 2.5 x 0.5 mm). Again, reference samples of silicon (Si) standard, active materials, carbon, and binder were ground/ball milled before mounted into ϕ 0.3 mm quartz capillaries and the XRD patterns of active materials were used for sample position adjustment before *in situ* experiments. A newly developed HT *in situ* sXRD device was used in *in situ* experiments. The details of this setup will be discussed in Chapter 3. A position sensitive detector (Mythen) was used. Each pattern was collected for 30 seconds. Unlike using an area detector, the PSD only collected a strip of the diffraction rings. Therefore, to enhance the signal to noise ratio, a few patterns

were added up wherever possible. For experiments at low rates (C/10, C/5, C/2 and 1C), two cells were measured in parallel in a heat resistive sample holder. For each cell, patterns of three different spots were collected before switching to the other cell, for the purpose of (1) comparison and checking the homogeneity of various parts of the electrode, and (2) summation of three patterns for better signal to noise ratio. The sample holder moved mainly in 2D to change spots and switch between batteries. For experiments at high rates (5C and 10C), only one battery was measured at a time and the measurement spot was kept unchanged since no inhomogeneity were detected in all the *in situ* experiments and less time spent on non-exposure were preferred for the time resolved experiments at high rates (for example, only 12 patterns can be taken during a full discharge at 10C). The batteries were cycled using external electrochemical cyclers (Biologic) and temperature data was monitored by the controlling interface using Eurotherm modules. *In situ* experiments at temperatures only started when the temperature stabilised at the designated testing temperatures.

2.3.3 Refinement

Whole pattern fitting was performed using the Topas v4.1[136] and GSAS-II software packages[137]. The peak shape profile was determined by the modified Thompson-Cox-Hastings function;[138–140] either a NIST LaB_6 or a Si standard was run in a capillary and used to refine the instrument peak profile and the parameters, which were used for the whole dataset. A linear absorption correction and sample displacement were determined from one pattern (by comparison of the peak positions of the active material XRD pattern measured in capillaries and those of the major active material peaks in the *in situ* cells) and then fixed for the remaining scans.

To model the complicated background (which includes the contributions from polyimide film, glassy carbon window, glass fibre separator, carbon in the electrode, and air scattering), the patterns of carbon, binder and empty cells were used to identify the contribution of Bragg and diffuse scattering from any non-active material. A combination of log interpolation between 12 average values observed in regions well away from the peaks was used, along with 5 synthetic peaks to model features from these identified backgrounds.

XRD data collected at Diamond Light Source were summed up in datasets of either three consecutive patterns (low rate *in situ* data) or two (high rate *in situ* data) to enhance the signal to noise ratio. Ring patterns collected using the area detector in APS were processed

with the GSAS-II software packages[137] into powder patterns and each pattern was refined without further summation.

Unit cell parameters and isotropic strain were refined for all scans using the Pawley method[141]. The unit cell parameters were refined using the adjusted peak positions extracted from *in situ* datasets. Isotropic strain was determined by the modified Thompson-Cox-Hastings function.[138–140] Rietveld refinement[139] was performed to determine phase fractions for two-phase regions. Atomic positions were fixed to values reported in previous single crystal studies[119,121–123], and a preferred orientation correction was also added to account for the morphology of the material and the pellet electrode. Because the pristine V_6O_{13} used in this study is plate-like crystallites as seen by SEM (Figure 2.1), there is a tendency to align the normal of the material along the axis of pressed pellet electrode. A spherical harmonics model using a harmonic order of 4 was used to correct the preferred orientation effects.[142]

Sequential refinement with different strategies was applied depending on the amount of phases present. In solid solution regions, sequential refinement was conducted continuously on the whole dataset, starting from either the most Li poor or Li rich phases, and progressing to the other end of the solid solution region. In two-phase regions, one dataset was always divided into two parts, from the point where both phases are prominent, normally at 50% fraction of each phase. Sequential refinement on each of the divided dataset started from this dividing point and progressed in two directions until one phase disappeared and the other phase reached 100% phase fraction. In sequential refinement, XRD data were refinement one by one in one dataset, where the output of the refined parameters of the first data point were used as the input for the second one, and so on.

2.3 Solid-state magic angle spinning nuclear magnetic resonance

Solid-state magic angle spinning (MAS) NMR spectroscopy was used to investigate the Li environment and electronic properties of the $Li_xV_6O_{13}$ series.

2.3.1 NMR sample preparation

All sample handling was done under Ar atmosphere in a MBraun glovebox with water and oxygen levels below 0.1 ppm to avoid contamination and/or reaction with moisture and air, respectively. $Li_xV_6O_{13}$ powder samples were prepared by electrochemically cycling V_6O_{13} and

Super P carbon powder mixtures (approximately 20 mg, weight ratio 8:2) at C/10 in two-electrode Swagelok cells at RT using a Biologic VSP cycler. Cell cycling was stopped at Li uptakes corresponding to nominal compositions of $Li_{0.3}V_6O_{13}$, $Li_{0.6}V_6O_{13}$, $Li_{0.8}V_6O_{13}$, $Li_{1.0}V_6O_{13}$, $Li_{1.2}V_6O_{13}$, $Li_{1.5}V_6O_{13}$, $Li_{1.8}V_6O_{13}$, $Li_{2.0}V_6O_{13}$, $Li_{3.3}V_6O_{13}$, $Li_{3.8}V_6O_{13}$, $Li_{4.5}V_6O_{13}$, and $Li_{6.4}V_6O_{13}$ upon discharge as well as $Li_{6.7}V_6O_{13}$, $Li_{3.8}V_6O_{13}$, and $Li_{1.1}V_6O_{13}$ upon charge. The powder samples were collected from disassembled cells, washed in DMC for three times, and dried under vacuum overnight. Phase purity and crystal structures were confirmed by lab source powder XRD measurements before packing the samples into ZrO_2 MAS rotors inside an Ar glovebox for the NMR experiments.

2.3.2 Measurement techniques and line shape fitting

RT solid-state *ex situ* MAS ^{7}Li NMR experiments were performed on a Bruker AVANCE III spectrometer with a magnetic field of B_0 = 4.7 T. The corresponding resonance frequency of ^{7}Li is 77.74 MHz. The NMR signals were referenced to a 1 M solution of LiCl in D_2O.[31] MAS NMR experiments were carried out at a spinning speed of 60 kHz at ambient temperature using a ZrO_2 rotor (1.3 mm diameter) in a Bruker 1.3 mm double resonance MAS NMR probe. ^{7}Li NMR signal line shapes were acquired by single pulse experiments with high-power pulses of 2.12 μs in length.

VT experiments were performed on a Bruker AVANCE III spectrometer with a magnetic field of B_0 = 11.7 T. The corresponding resonance frequency of ^{7}Li is 194.32 MHz. The NMR signals were referenced to a 1 M solution of LiCl in D_2O.[31] MAS NMR experiments were carried out at a spinning speed of 14 kHz using rotors with ZrO_2 caps (4.0 mm diameter) in a Bruker 4.0 mm double resonance MAS NMR probe. Raw data handling and processing were done using Bruker Topspin 2.1.

2.4 Application of density functional theory calculation on V_6O_{13}

Spin-unrestricted solid-state DFT simulations of charge densities and density of states were performed in the Vienna *Ab initio* Simulation Package (VASP5.3).[143] The projector-augmented wave (PAW)[144] approach was used to describe the electron-ion core interaction. The plane-wave energy cutoff value was set to 520 eV. For the PAW sets, the *s* semicore states were treated as valence for Li and vanadium, and the standard PAW set was used for oxygen. The Brillouin zone was sampled using a gamma-centred k-point mesh of 4×10×4. Full optimization of the atomic positions and cell parameters and total energy calculations were performed in the absence of symmetry constraints, in which the energy and root-

mean-square forces was converged to 10^{-6} eV and 10^{-5} eV/Å, respectively. The Perdew−Burke−Ernzerhof (PBE)[145] exchange-correlation functional was used, applying a Hubbard U model[146,147] within the rotationally invariant formalism proposed by Liechtenstein *et al*.[148] to correct for the known deficiencies of pure functionals for highly localized 3*d* states. The on-site Coulomb (U) and exchange (J) parameters of 4.5 eV and 1 eV were chosen for vanadium in line with previous work on V_6O_{13}.[149]

The thermodynamical phase stability and structures of 10 discrete members of the $Li_xV_6O_{13}$ series (x = 0, 1, 2 .. to 9) were assessed by comparing the formation enthalpy of different phases. The $Li_9V_6O_{13}$ structure was included as a model structure to enable the generation of all possible configurations for the intermediate stages of lithiation, although its formation is thought to be electrochemically unlikely (Figure 2.4). The initial $Li_9V_6O_{13}$ structure was modelled with the *C*2/*m* space group, with two additional Li sites Li(5) (square pyramidal) and Li(6) (square planar LiO_4) included (Figure 2.4) in addition to Li(1) – Li(4). The Li(1) site was not directly included in the $Li_9V_6O_{13}$ structure due to the small distances between neighbouring Li sites at high degrees of lithiation. All intermediate Li compositions, $Li_xV_6O_{13}$ were derived by partially delithiating the $Li_9V_6O_{13}$ structure and enumerating all symmetrically distinct orderings using the Cluster-Assisted Statistical Mechanics (CASM) software.[150,151] The computed structures were generated from the primitive cell of $Li_9V_6O_{13}$, containing 28 atoms, in which the distortion in the vanadium octahedra was removed artificially. Consequently, the primitive cells computed with DFT contain half of the atoms of the cells reported in the single crystal studies.[121–124] A total number of 272 configurations were generated in total, with 1, 5, 20, 44, 66, 66, 44, 20, 5 and 1 configurations for V_6O_{13}, $Li_1V_6O_{13}$, $Li_2V_6O_{13}$, $Li_3V_6O_{13}$, $Li_4V_6O_{13}$, $Li_5V_6O_{13}$, $Li_6V_6O_{13}$, $Li_7V_6O_{13}$, $Li_8V_6O_{13}$, and $Li_9V_6O_{13}$, respectively. From the calculated DFT total energy, *E*, of each configuration, the formation energy per formula unit was calculated,[150] as

$\Delta E(x) = E(Li_xV_6O_{13}) - (1- x/9)\, E(V_6O_{13}) - x/9\, E(Li_9V_6O_{13})$.

NMR shifts are calculated to help determine the position of Li in $Li_xV_6O_{13}$ structures. The major contribution to the ^{7}Li NMR shift in these systems is considered to be the hyperfine Fermi contact shift, originating from the unpaired spin density transferred from the vanadium *d* orbitals to the Li s orbitals via the oxygen bond. The Fermi contact shift can be calculated from first principles by integrating the unpaired spin density at the Li centre, and converting it into a hyperfine shift as described in the work by Kim *et al*.[152]

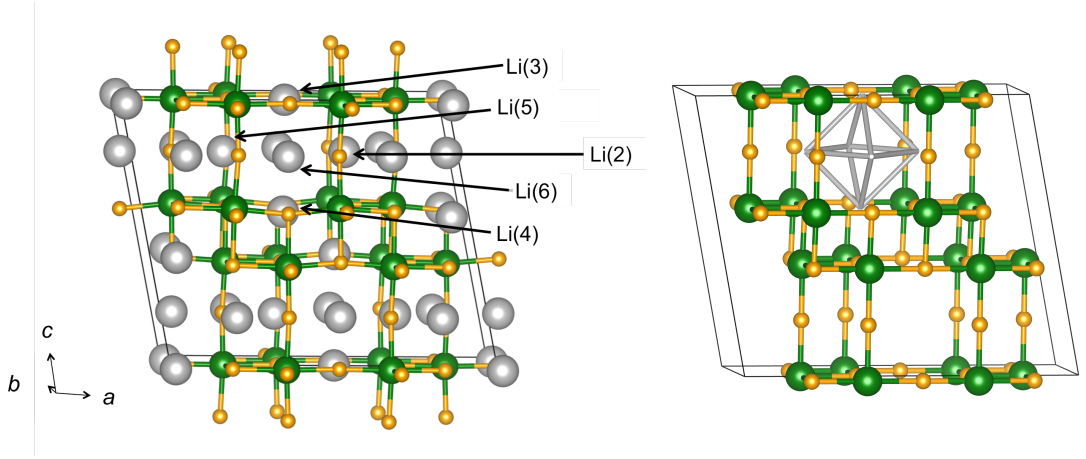

Figure 2.5. $Li_9V_6O_{13}$ structure (left) generated to enable all possible configurations of the intermediate stages of lithiation. All the Li(2) to Li(6) positions are at the corners of the octahedral cavity (right) between the single and double layers.

Preliminary calculations were performed on the LiV_6O_{13} system using the all-electron DFT code CRYSTAL14.[153] Two hybrid functionals were used, the B3LYP functional with 20% Hartree-Fock exchange[154], and a modified B3LYP with 20% Hartree-Fock exchange, hence for each Li site, two values of the calculated hyperfine shift will be reported hereafter. The Fermi contact shift was calculated for various LiV_6O_{13} orderings, each containing a different occupied Li site among the Li(1)-Li(6) centres.

3 A high-temperature *in situ* XRD cell setup for battery research

In the previous years, people have done HT work, for example, Mestre-Aizpurua *et al*. have studied the HT electrochemical performance of $LiFePO_4$ with a few different types of electrolytes.[90] They utilised a type of adapted Swagelok cell to perform HT cycling of $LiFePO_4$ up to 300°C.[155] This design has a good temperature range and good electrochemical cycling performance testing battery materials. In order to gain more insights into the material properties, such as phase transition mechanisms, other techniques need to be combined with electrochemically working cells. To probe the phase transformations of electrode materials at HTs, the first HT *in situ* synchrotron XRD battery characterisation setup that enables studying the material properties in cycling batteries in real time from RT to 250°C was developed in collaboration with DLS I11. Tests of the new setup were applied on $LiFePO_4$ from RT to 150°C. Insights into the HT phase transformation mechanisms of $LiFePO_4$ at high cycling rates were studied for the first time.

3.1 Introduction to current design of *in situ* XRD setups

In situ techniques play central roles in battery characterisation due to their advantages over *ex situ* techniques. *In situ* XRD is one of the most commonly used techniques in battery research. The core difficulty in realising *in situ* XRD experiments lies in the design of the *in situ* cells. Nowadays, there are already several designs for probing reactions in batteries at RT.[135]

3.1.1 *In situ* vs. *ex situ* techniques

In situ techniques in the battery research field refer to characterisation techniques that do not require disassembling battery cells, as opposed to *ex situ* techniques, which most often include cycling batteries to certain states of discharge/charge, disassembling the cells, extracting the materials and performing measurements.[8] The battery research community distinguishes between the terms *in situ* and *operando*, where the former means, in general, measurements done with batteries kept in position, and the latter means, specifically, measurements taken during electrochemical cycling. Therefore, *operando* can be considered as a special case of *in situ*. In this thesis, only the term *in situ* is used to describe experiments

without cell disassembly, which are also *operando* studies. *In situ* techniques become increasingly valued due to their significant advantages over *ex situ* methods, which include:

(1) Allowing materials to be probed in real time: *In situ* techniques enable direct material monitoring when the reaction happens, efficiently probing any short-lived intermediates and allowing no time for material relaxation if not desired.[77] The *in situ* characterisation process is like taking snapshots of reaction, so that, when the time interval is small, time dependent processes can be monitored. Sample relaxation between the end of the electrochemical process and the beginning of the characterisation measurements is difficult to avoid, making it almost impossible to conduct any time-resolved experiments on the ongoing electrochemical process.

(2) Improving consistency and saving time: In battery research, repetitive efforts are spent on extracting the materials from batteries, following appropriate sample treatment procedure before characterisation and measuring series of samples. *In situ* experiments avoid the several steps between reaction and characterisation, so that the consistency improves by measuring different Li compositions on the same sample rather than on different samples for *ex situ* measurements. Possible contamination issues that sometimes happen during sample treatments can also be prevented. Data collection is normally automated and continuously done once the experiment is set up.

In situ techniques have the aforementioned advantages over *ex situ* techniques, especially when short-lived phases are present and time-resolved experiments are needed. The application of diffraction methods have long been established since the early study of transition metal sulfides[156] and these methods remain the most powerful tool in unravelling the phase information, phase transition mechanism and dynamics in batteries for crystalline materials.[157,158]

3.1.2 State-of-the-art of *in situ* XRD setups

The basic requirement for an *in situ* XRD setup that works in transmission geometry is to allow X-ray transmission through the cell and diffraction on the sample, while the cell is cycled (Figure 3.1). In order to be electrochemical functioning, the cell needs to have a combination of conductive and insulating components to let the electrons and ions flow separately. The battery components need to be chemically inert against the electrolyte and other chemical species inside batteries. In addition, batteries are a closed system so that sealing must be airtight.[14] Stack pressure is important for most types of batteries so that springs, screws, and pressing are introduced. Different LIBs have various types of cell casings,

current collectors, and separators, which are not directly related to the chemistry but essential to battery performance.

In addition to the working battery itself, the special part of *in situ* XRD cell design is to allow X-ray to reach and interact with the material studied. There should also be no obstacle before the diffracted beams reach the detector. The materials used for X-ray transparent window include very light metal, such as beryllium (Be), and polymers, such as polyimide or amorphous substances.[159–163]

Be is the only metal that is suitable as a metal X-ray window in this case, because (1) it has a small X-ray absorption coefficient, with the first diffraction peak at 2θ = 46° $Cu_{K\alpha1}$, hence generating minimal background for the XRD patterns of the target materials, (2) it is chemically inert, which minimises side reactions, and (3) there is enough mechanical robustness to withstand the pressure needed in batteries. Therefore, from the first *in situ* XRD cells studying TiS_2,[156] to the recently adapted Swagelok-type design,[164] a Be window remains a widely accepted choice for X-ray windows.[159,165] However, because contact/inhalation of Be is fatal, the toxicity of Be is a big issue for inherently safe hardware designs.

Another type of X-ray window is polymer thin-film, which is amorphous and provides only diffuse background (no sharp Bragg peaks as opposed to crystalline Be). A few types of adapted cells have been developed using thin-film X-ray windows, for example, coin cells with holes formed at the centre and covered with polyimide thin fills[159] or aluminised Mylar®[166]; bag cells with layers of polymer films as both cell casing and X-ray window.[111] These mechanically 'soft' X-ray windows hardly provide enough stack pressure to batteries and are the main reasons behind the unreliable electrochemical cycling of these types of cells. Even in cases where the electrochemistry is fine, the area probed by the X-ray beam is highly unlikely to be representative of the whole electrode, since the stack pressure at the polymer site and the original hard cell casing site can be vastly different, leading to inhomogeneity in the electrode.[167] In addition to the pressure issue, the permeability of the thin films also results in O_2, moisture, and N_2 leaking into the cell and ultimately has a negative effect on the cell's electrochemistry.

Borkiewicz *et al.* (Argonne National Laboratory, US) have recently reported the application of a dense glassy carbon disk as the X-ray window for *in situ* cells.[135] This application offers an X-ray transmissive, mechanically robust, non-toxic and low gas permeability window. The only drawback of this X-ray window is its brittleness. Therefore, the diameter of the glassy carbon needs to be quite small in any incorporated design. It also reacts with Li

spontaneously, so a separating current collector needs to be present if metallic Li is to be used. The dense glassy carbon disks are successfully applied in Argonne's multi-purpose *in situ* X-ray (AMPIX) cells, collecting consistent electrochemistry and XRD data.

Most of the aforementioned designs report reasonable electrochemistry performance at RT, but none of them is capable of characterisation over a wide temperature range. The design by Borkiewicz *et al*. can be heated by thermal tapes to at least 80^{o}C without modification on the cell.[168] However, temperature sensing and the heat tolerance of some components, for instance, the polymer O-ring, may prevent the design from being used at higher temperatures.

3.2 Designing a new variable temperature *in situ* XRD cell

3.2.1 Objective of the new design

There is no *in situ* XRD device that is capable of measuring real-time reactions from RT to 250^{o}C, or at least to 150^{o}C on the first instance. The goal of this section is to design an *in situ* XRD battery system with a wide temperature range to tackle the phase transformation problems during HT cycling. Because the first applications of the setup are on I11 at DLS, the system is designed to work with transmission geometry.

3.2.2 Criteria for the new *in situ* cell design

The custom-designed VT *in situ* XRD cell (VATIC) aims to monitor the evolution of materials using XRD during electrochemical cycling at HT. Therefore, the cell needs to be (Figure 3.1):

(1) Properly designed with electronically conducting and insulating parts: The cell needs to be conductive to release the chemical potential stored in the cell in the form of electric energy. However, the two electrodes of the cell must be insulated from each other to avoid short-circuiting.

(2) Mechanically robust to provide stack pressure: The electrochemistry performance of batteries are heavily linked to their stack pressure inside the cells.[167] The amount and homogeneity of stack pressure is key to the full utilisation and homogenous reaction of electrode materials.

(3) X-ray transparent: The cell needs to be X-ray transparent through the part where the battery material is monitored, considering a transmission geometry. Therefore, the material chosen for X-ray windows is normally different to the other parts of the cell. Since the X-ray window is still an integral part of the cell, the mechanical strength and electrical conductivity are both material properties to be considered.

(4) Chemically inert: The electrolyte and electrode material, especially alkane metal, in the batteries can be corrosive/reactive. Hence, chemically inert cell parts are essential to the battery performance and long-term cycle life. The cell parts should be non-reacting to the battery materials so that the main reaction in the batteries is the electrochemical "Rocking Chair" process.

(5) Airtight: H_2O and O_2 destroy battery materials and reaction pathways and should be prevented from permeating into the cell. For instance, H_2O react with the most commonly used $LiPF_6$ in electrolyte and Li metal reacts with O_2.[17]

(6) Precisely temperature controlled: Because reactions in batteries always generate heat, the temperature monitoring and control system needs to be able to track the accurate temperature at battery materials in order to precisely study the temperature effect on battery reaction mechanisms. The cell also needs to be mechanically and chemically stable over long-term at elevated temperatures of up to 150°C, while remaining air-tightly sealed.

The heating and temperature control system is the main advantage of the VATIC, which gives the cell a wide temperature range for operation. Because HT may stimulate/accelerate the reaction of battery components and change the mechanical properties of the sealing parts, the materials need to be carefully chosen in order to function for the whole temperature range (RT to 250°C).

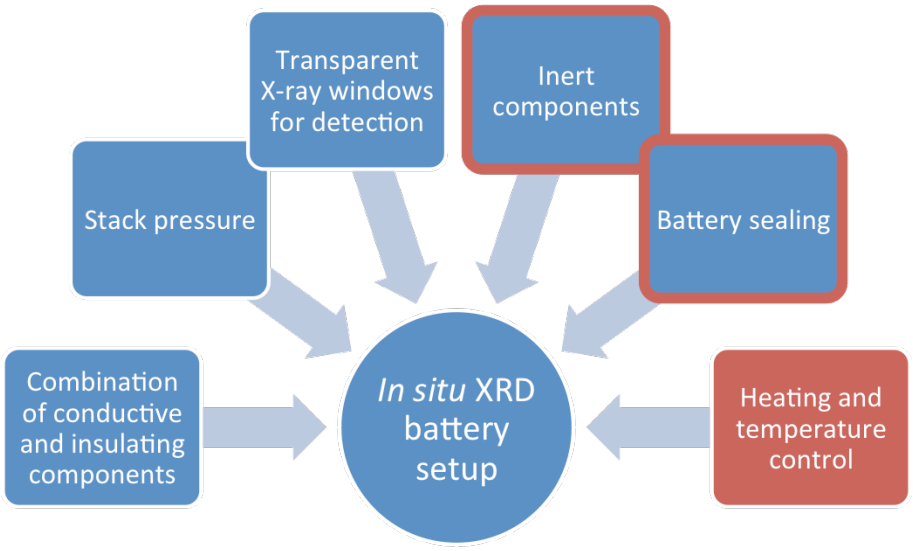

Figure 3.1. Important aspects to be considered for designing *in situ* XRD battery setup; blue blocks represent general requirements; red ones are for HT only, and the red-circled ones are HT related.

3.2.3 Design of the VATIC

The VATIC design is adapted from Swagelok-type cells, containing three main pieces: a top part, a cell body, and a bottom part (Figure 3.2).

The top part contains one stainless steel plunger, one spring, one stainless steel pellet and one hard carbon X-ray window. The top electrode is in direct contact with the current collector and one electrode of the battery, such as Li metal, sodium (Na) metal or graphite. The plunger is bored through to allow transmission of the X-ray beam. A rod points out on top of the plunger, serving as an electrical connection to the external circuit. A relatively thick stainless steel pellet with an 8 mm cavity in the middle, which is joined by a piece of hard glassy carbon before battery assembly, is added to support one electrode and provide homogeneous pressure. The spring between the pellet and plunger can be compressed to provide mechanical pressure inside the battery. The glassy carbon disk acts as both an X-ray transmission window and a hard support for the battery electrode, which is important for homogenised stack pressure inside the cell. The glassy carbon window is attached to the pellet with silver epoxy glue so that the glassy carbon window is electrically connected to the top electrode base. When Li or Na is used as the top electrode, a copper (Cu) current collector should be used to separate the pellet and the alkaline metal electrode to protect glassy carbon window from reaction with Li or Na. The centre of the Cu foil needs to be cut open to allow X-ray transmission and a polyimide tape covers the hole of and sticks the Cu foil to the current collector and pellet. The current collector also helps with alleviating the corrosion of the silver epoxy glue by the electrolyte.

The bottom part contains a base electrode, a hard X-ray window. The bottom electrode is in direct contact with the electrode material of the battery that is to be studied by XRD. It also contains a cavity for an 8 mm glassy carbon disc. A rod points out from the side of the bottom part to serve as a port for the electrical connection. There are, in total eight holes on the base, four of which are for screws and the rest are for cartridge heaters.

The cell body contains a cylindrical hole through the centre, which holds the electrode stack, including the battery anode, separator with electrolyte, cathode, current collector, stainless steel pellet, spring, and plunger. A sheet of polyimide film covers the inner surface, which is chemically inert and electronically insulating, preventing the cell from short-circuiting. The body also has eight holes that align with the holes on the base. One nut and a set of ferrules complete the components of the VATIC.

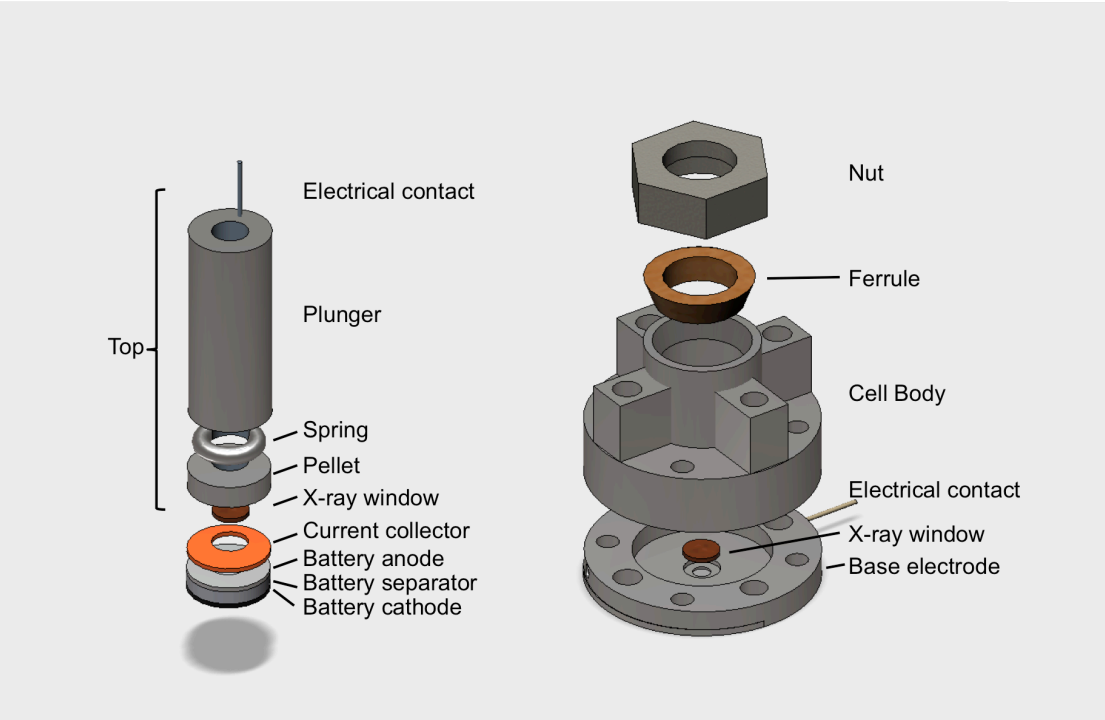

Figure 3.2. The breakdown schematic drawing of VATIC. The top part is in contact with one electrode of the battery and contains components shown to fulfil the mechanical and electrochemical requirements of the cell. The bottom part contains a stainless steel base pasted with an X-ray window to provide mechanical support to the other electrode and act as an X-ray transmissive current collector; a rod pointing out serves as a port for electrical connection to the out circuit. The cell body contains the battery components, which is capped by a nut and ferrule for sealing.

The VATIC assembly starts from the bottom electrode as shown in Figure 3.3. First, the battery stack, containing a cathode, an anode, and a separator is placed on top of the bottom part and aligned at the centre (assuming the cathode is the material to be studied). The potential of the whole bottom electrode is equal to that of the cathode. Second, the top part is placed on top of the battery to provide mechanical pressure. The potential of the top electrode equals that of the anode. Therefore, the voltage between the two electrical contacts is the same as the output voltage of the battery, neglecting the Ohmic resistance of the cell parts since they are all metal and most are made of 316 stainless steel. The cell body encases the battery with the ferrule and hexagonal nut topping and sealing the whole battery. Sufficient tightening of the top nut guarantees the sealing of the top part. Four screws hold the cell body and bottom together when the cell is assembled. In addition, a Viton® O-ring sits between the cell body and the base, providing the seal of the bottom once the screws are tightened. Finally, a polyimide tape, the last component of the sealing system (Figure 3.4), seals the hole on the plunger to keep the inner atmosphere of the battery from being contaminated by air.

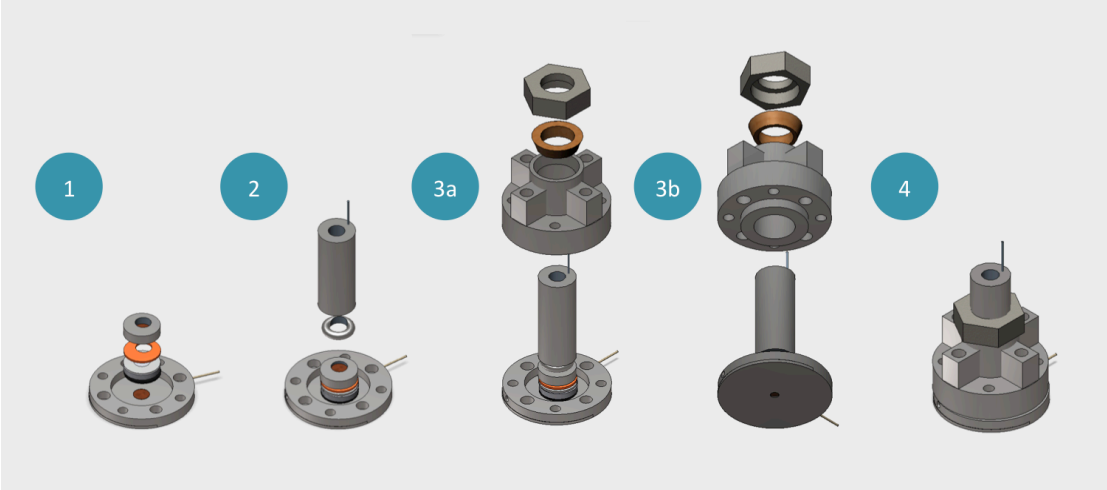

Figure 3.3. Cell assembly procedure of the VATIC. (1) The battery containing two electrodes and separator (soaked with electrolyte) is sandwiched between the bottom electrode and pellet/current collector set. (2) The plunger and spring are put on top of the pellet to provide pressure and serve as a long extension of the top electrode. (3) The body (with polyimide film on the inner surface), ferrule and nut assure that the battery is in an insulating and airtight environment. (3a) and (3b) are the top front and bottom front views of the cell, respectively. (4) The fully assembled VATIC.

3.2.4 Battery holder, electrochemical contacts and temperature control

The VATIC, the ceramic battery stand, Eurotherm® temperature controllers, and cycler are placed inside the experimental hutch (Figure 3.4). The batteries are held in a ceramic stand and positioned in parallel to the beam. The incident beam is directed to the materials studied, and the diffracted beams are collected by the detector. The ceramic stand thermally insulates the cells from the sample stage, which moves in 3D for cell alignment and to change the cell.

The VATIC is connected to the cycler via the two electrical contacts during cycling. Even though almost the whole cell is made of stainless steel, the polyimide film and plastic ferrules insulate the top and bottom electrodes (Figure 3.4).

The temperature control system consists of the Eurotherm®, heat cartridges, and K-type thermocouples. Four holes on the cell body, as mentioned before, are left for cartridge heaters. The cylindrical cartridge heaters fill in the holes and heat the cell from four sides to ramp up the temperature homogenously. There are also two small holes: one on the side of the bottom electrode and the other next to a screw hole (Figure 3.4). The hole on the bottom electrode is drilled almost to the centre of the base, so that a thermocouple can be inserted to measure the exact temperature of the battery electrode material. This temperature inputs into the Eurotherm® and controls the output power of the cartridge heaters. Furthermore, an independent temperature shutdown system is added as a safety precaution, which contains a K-type thermocouple that goes into the hole in the cell body. This thermocouple measures the temperature of the cell independently and inputs into another temperature feedback system, which is set to cut down the output power of all cartridge heaters once a temperature overshoot is detected.

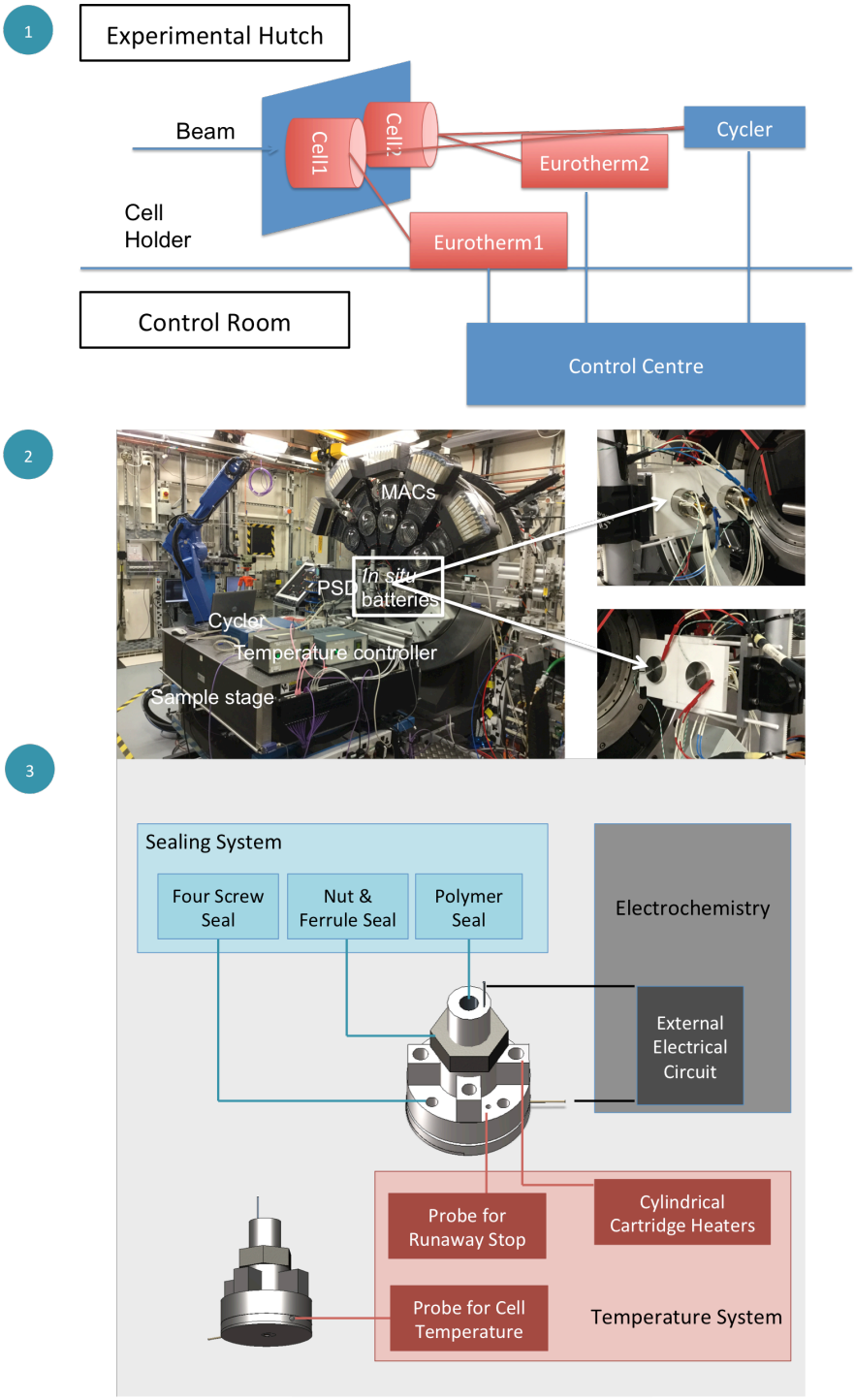

Figure 3.4. The schematic setup, photographs of the experimental hutch at DLS I11, and the various aspects of the battery. (1) The scheme of the VATIC setup including the cells, electrochemical devices, temperature controllers, X-ray facility and the digital control system, placed across the experimental hutch and the control room. Red items indicate devices that are related to the temperature system. (2) Photograph of the experimental hutch showing the X-ray detectors, battery cycler, temperature controller, sample stage and the *in situ* batteries (zoom in pictures show front and back view). (3) The sealing system of the VATIC and the connections to external devices. The VATIC needs to be sealed to complete assembly, which includes using four screws to tighten the bottom and using the nut/ferrule set and a polyimide film to seal the top. The two electrical contacts lead to the external cycler. The other holes are left for the heating system, of which four are for the heater cartridges, one is for the thermocouple, and the other is for the second thermocouple of the safety shutdown system.

3.2.5 Benchmarking the VATIC

Both electrochemical and thermal tests were done on the VATIC to benchmark this cell design. For electrochemical testing, $LiFePO_4$/carbon composite were used, as been introduced in Chapter 2. Rate dependency tests from C/10 to 1C were done in both Swageloks and VATIC (Figure 3.5). Comparison of the discharge capacities for the first 20 cycles at these rates shows barely any difference, demonstrating the electrochemical performance of VATIC being equally convincing as the proved Swagelok design, at least for the first 20 cycles.

Temperature data of the VATIC show that the cell temperature can increase to 150°C in less than half an hour and stay constant for the time measured (Figure 3.6). Once the Eurotherm controller is programmed with the optimised ramping rate and limit, temperature overshoot can be avoided. When the temperature reaches the plateau, it only fluctuates within 0.2°C at 150°C. At lower temperatures, because the temperature gradient across the cell body is less, it is even easier to control the temperature of the VATIC.

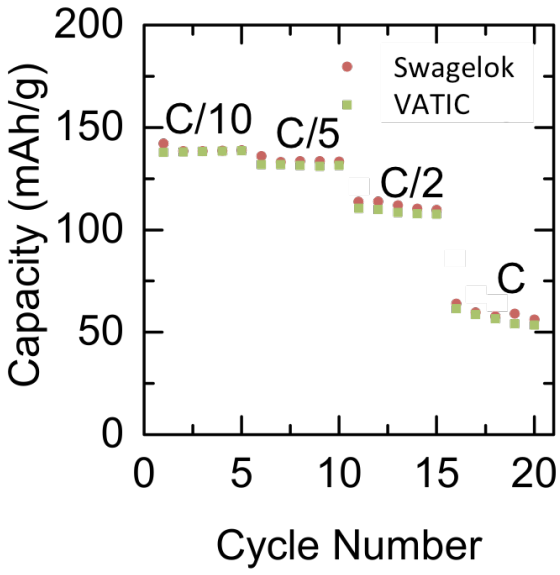

Figure 3.5. Comparison of discharge capacities of $LiFePO_4$ cycled in a Swagelok cell (red) and VATIC (green) configuration at C/10, C/5, C/2 and 1C. The discharge capacities at these rates show barely any differences for these two cell configurations, verifying the electrochemical performance of the new VATIC design.

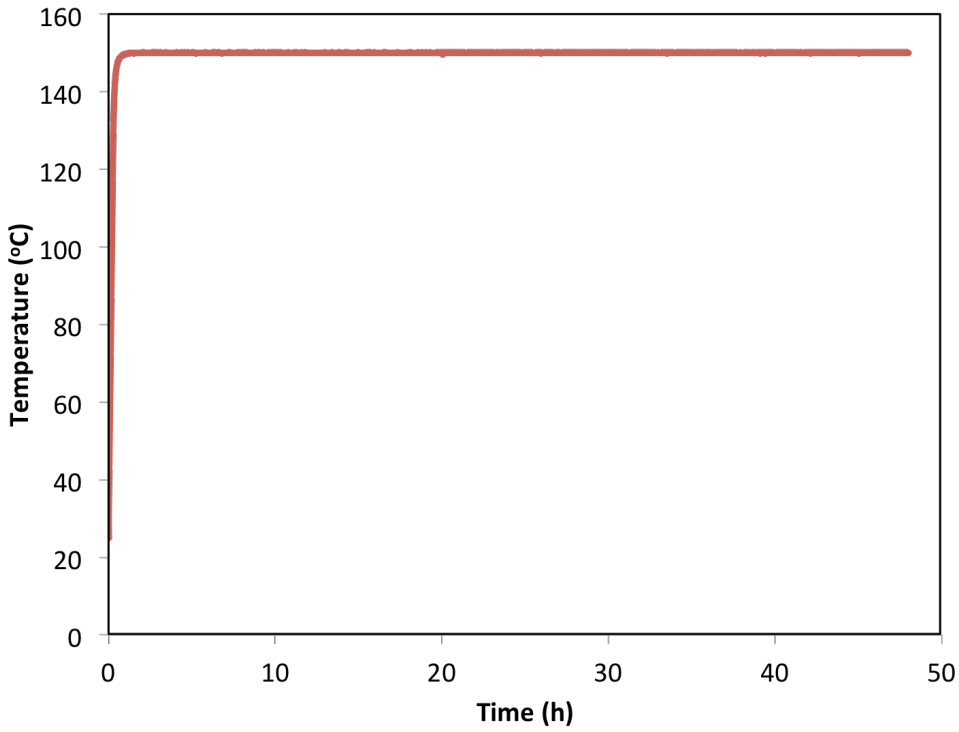

Figure 3.6. The VATIC temperature controlling system was tested at 150°C. The cell was heated to 150°C within less than half an hour. Temperature fluctuation can be kept within 0.2°C at 150°C.

The HT work studied in this thesis was done at constant temperatures. The cells were heated to a certain temperature and kept constant during each set of experiments. Therefore, each set of *in situ* experiments was accomplished at the temperature stated and constant temperature data were not shown in the rest of the thesis.

3.3 High temperature *in situ* XRD on $LiFePO_4$

$LiFePO_4$ is reported to undergo a non-equilibrium solid solution phase transition mechanism instead of a two-phase nucleation and growth mechanism when cycled at high rates at RT.[77] However, the HT phase transition mechanism of $LiFePO_4$ at high rates remains unknown. With the newly developed VATIC system, HT *in situ* XRD can be performed on $LiFePO_4$ to study its HT phase transformation mechanism. A set of high rate cycling experiments is performed on $LiFePO_4$ from 25°C to 150°C (Table 3.1).

Table 3.1. List of experiments performed on LiFePO4 from 25 to 150°C. The rate of cycling is represented in C-rate forms. Batteries with the organic electrolyte (1M $LiPF_6$ in EC/DMC) are tested at 25 and 75°C. Batteries with the IL electrolyte (0.5 mol/kg LiTFSI in [C3mpyr][TFSI] are tested from 75 to 150°C.

Temperature (°C)	Organic electrolyte	IL electrolyte
25	C, 5C, and 10C	No experiments
75	C, 5C, and 10C	C, 2C, 5C, and 10C
100	No experiments	C, 2C, 5C, and 10C
125	No experiments	5C, and 10C
150	No experiments	5C, 10C

3.3.1 Current induced solid solution (de)lithiation mechanism of $LiFePO_4$ at room temperature

$LiFePO_4$ is first cycled at a rate 1C at RT in LP30 (Figure 3.7, left). Bragg peaks at the start and the end of charge, i.e., the pristine cell and cycled for 1.9 hours, respectively, can be indexed to either the $LiFePO_4$ or $FePO_4$ phase in the space group of *Pnma*[46,169]. At the end of discharge, the overlapping (211) and (020) reflections at 9.42° 2θ indicate the formation of $LiFePO_4$. A two-phase reaction mechanism would result in peak intensities only in the $LiFePO_4$ (211), (020) and $FePO_4$ (211), (020) between 9.4 and 9.8° 2θ (Figure 3.7, left). However, a substantial amount of intensity between 9.45° and 9.65° 2θ range when the cell is cycled for 0.5 and 2.2 hours, corresponding to the plateaus of charge and discharge in the voltage profile (Figure 3.7, right). The intensities are asymmetrically broadened peaks, indicating the formation of intermediate phases with lattice parameters that deviate from $LiFePO_4$ and $FePO_4$. This evidence suggests that the phase transformation mechanism of $LiFePO_4$ at high cycling current differs from the two-phase nucleation and growth mechanism that normally appears to be present when $LiFePO_4$ is cycled at low rates.[77] The charging process took 1.9 hours even though, at a rate of 1C, this process is projected to be no more than 1 hour. A change of the slope of the voltage profile is also observed at 4 V during charge, which possibly relates to unexpected electrolyte decomposition at high voltage since the bulk electrode materials stay in the $FePO_4$ form.

The formation of intermediate phases is also observed at higher rates of 5C and 10C (Figure 3.7, right). At 5C, the (211) peak of $LiFePO_4$ continuously moves to higher 2θ angles as the

cell is charged, eventually stopping at 9.58° 2θ at the end of the charge when cycling time reaches 0.25 hr, at a smaller value than that of the (211) reflection of the fully delithiated $FePO_4$ phase. Meanwhile, $FePO_4$ (020) reflection deviates from the equilibrium value and becomes dominant at the end of charge, indicating that Li_xFePO_4 is delithiated to a Li poor phase and Li ions inside Li_xFePO_4 are not fully extracted. The end phases at each of the 10C charge show further deviation from the fully discharged $FePO_4$ phase, but the continuous change in (211) peak position is still present, showing once again the existence of the solid solution phase. For both the 5C and 10C cycles, the overvoltage is large compared to that seen with 1C cycling. The onset voltage of charge only starts from 3.75 V and 4.05 V for 5C and 10C cycles, respectively (equilibrium voltage is approximately 3.45 V), and the capacity only corresponds to 75% and 50% of the theoretical capacity for 5C and 10C, respectively. This overvoltage could either be due to the resistive elements inside the cell causing large Ohmic drop especially for the first few cycles, or the larger overpotential from $LiFePO_4$ at high rates at RT. Nevertheless, RT *in situ* diffraction on $LiFePO_4$ at high rates shows that the material transforms via a solid solution mechanism, in agreement with previous *in situ* XRD studies.[77]

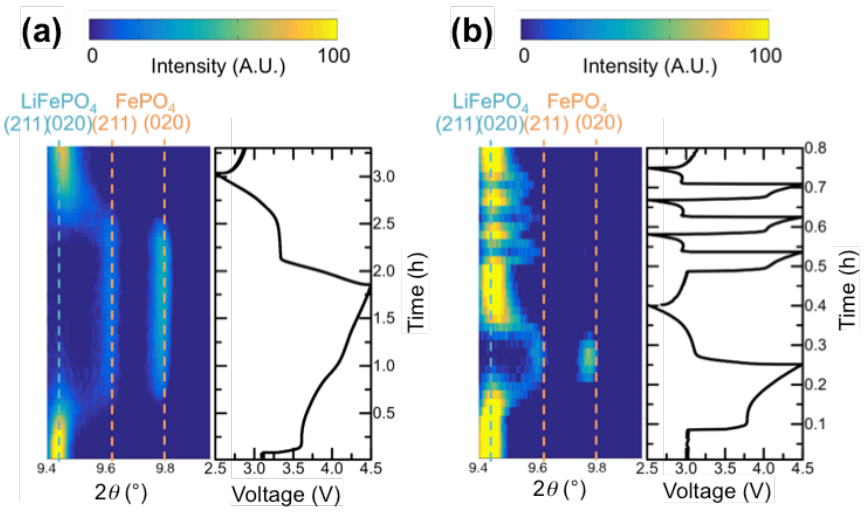

Figure 3.7. *In situ* XRD patterns collected during galvanostatic charge/discharge at (a) a rate of 1C at RT (organic electrolyte cell), and (b) 5C rate for one cycle and 10C rate for three cycles at RT (organic electrolyte cell). The contour plot of diffraction patterns for (211) and (020) reflections during the first charge and discharge cycle is plotted on the left. The intensities of the diffraction peaks are colour coded referring to the scale bar on top, where A.U. mean arbitrary units. The peaks highlighted in cyan represent $LiFePO_4$, and those highlighted in orange represent $FePO_4$. The horizontal axis is the selected 2θ region, and the vertical axis is the time. The corresponding voltage profile is plotted to the right.

3.3.2 Cycling $LiFePO_4$ with organic electrolyte at 75 °C

At 1C rate at 75°C, the discharge and charge profile of $LiFePO_4$ shows a flatter plateau compared to that at ambient temperature (Figure 3.8, left). The intensity between the $LiFePO_4$ and $FePO_4$ (211) reflections seems to be less pronounced than at RT, which indicates that the current-induced solid solution mechanism is suppressed and a two-phase mechanism takes place at the same time. However, the formation of intermediate solid solution phases becomes more pronounced when the material is cycled at 5C and 10C, than at 1C (Figure 3.8, middle and right). The voltage profiles show sloping effects at 5C and 10C, corresponding to the solid solution mechanism (Figure 3.8, middle and right). The voltage differences between charge and discharge plateaus at 75°C are 0.2 V and 0.35 V at 5C and 10C, respectively, much smaller than those of 0.7 V (5C) and 1 V (10C) at RT. The elevated temperature enhances the Li diffusion in the bulk electrode and reduces the overpotential to drive Li diffusion, decreasing the overall overvoltage. The electrochemistry data show that the full capacity is achieved at 1C, 5C, and 10C (Figure 3.8) and XRD data show that Li_xFePO_4 is either fully delithiated/lithiated at the end of charge/discharge.

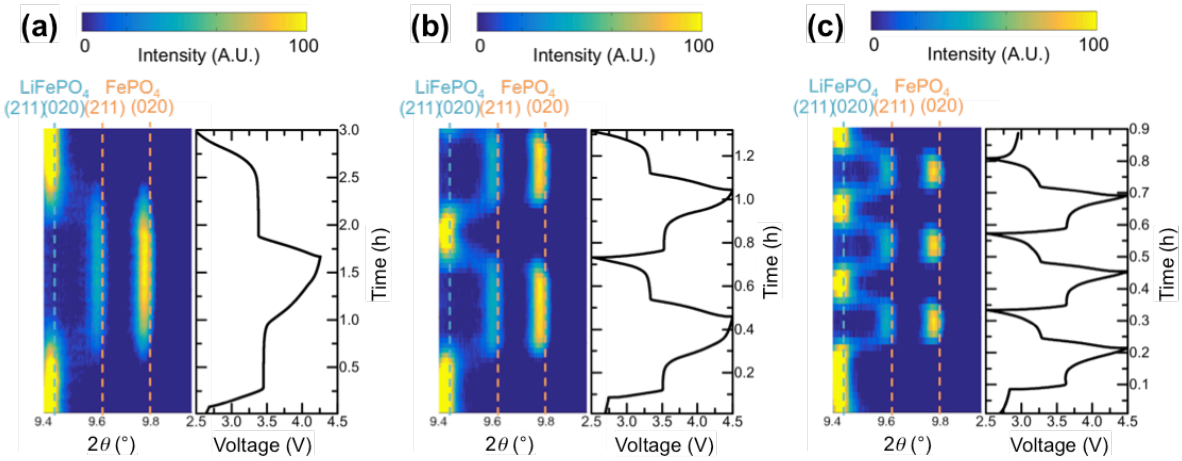

Figure 3.8. *In situ* XRD patterns collected during galvanostatic charge/discharge at (a) 1C rate for one cycle at 75°C (organic electrolyte cell), (b) 5C rate for two cycles at 75°C (organic electrolyte cell), and (c) 10C rate for three cycles at 75°C (organic electrolyte cell). The contour plot of diffraction patterns for (211) and (020) reflections during the first charge and discharge cycle is plotted on the left. The intensities of the diffraction peaks are colour coded referring to the scale bar on top, where A.U. mean arbitrary units. The peaks highlighted in cyan represent $LiFePO_4$, and those highlighted in orange represent $FePO_4$. The horizontal axis is the selected 2θ region, and the vertical axis is the time. The corresponding voltage profile is plotted to the right.

3.3.3 Cycling $LiFePO_4$ with IL at 75°C

The electrochemical performance depends highly on the cycling rate at 75°C when an IL electrolyte is used. At cycling rates of 1C and 2C, both the electrochemistry and diffraction show result that the battery cycles with full theoretical capacity and the end phase $LiFePO_4$ and $FePO_4$ are always formed (Figure 3.9, left). The sloping discharge and charge plateaus have small voltage differences, and the cell registers almost 100% theoretical capacity at both rates. The electrode material transforms in a solid solution mechanism based on the intensity between $LiFePO_4$ and $FePO_4$ (211) peaks. At 5C, the cell only utilises 40% of the theoretical capacity, and the XRD patterns show that a large portion of $LiFePO_4$ is not transformed into $FePO_4$ even at the end of the charging process (Figure 3.9, middle). Since the solid-state Li diffusion is not a problem for the electrode material at this temperature[48], the cause of the insufficient utilisation of $LiFePO_4$ is likely to be due to the electrolyte or solid electrolyte interface. As discussed in Chapter 1, the IL electrolyte is very viscous, and Li transport in the electrolyte is slow. At rates beyond 5C at 75°C, the Li ion conductivity in the IL might be difficult to match that required by the current flow. At 10C, the requirement of fast ion conduction far beyond the ion conduction capability of this IL at 75°C, therefore a large proportion of $LiFePO_4$ is barely accessed and little is transformed into $FePO_4$ or any intermediate states, resulting in the reduced capacities of these cells at high rates (Figure 3.9, right).

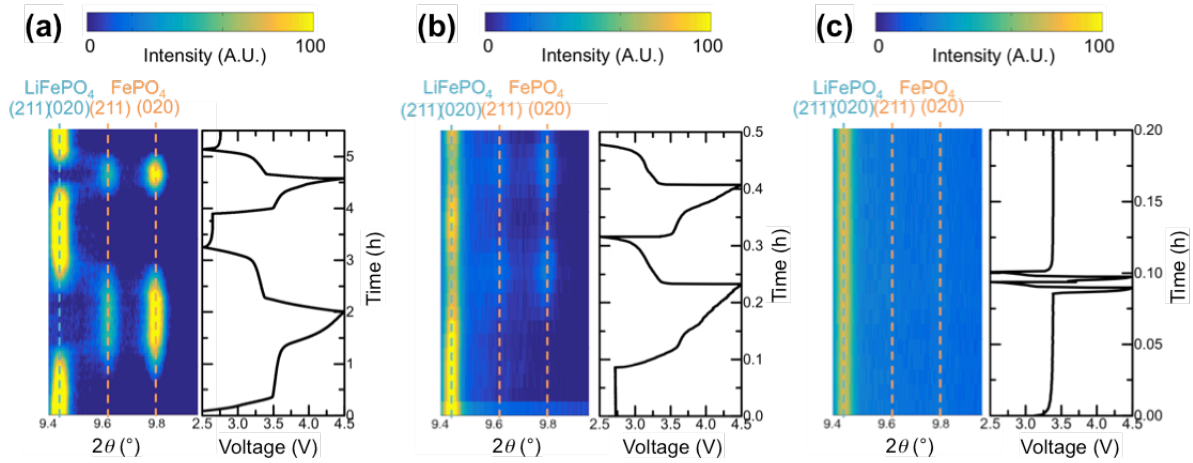

Figure 3.9. *In situ* XRD patterns collected during galvanostatic charge/discharge at (a) 1C rate for one cycles and 2C rate for one cycle at 75°C (IL electrolyte cell), (b) 5C rate for two cycles at 75°C (IL electrolyte cell), and (c) 10C rate for two cycles at 75°C (IL electrolyte cell). The contour plot of diffraction patterns for (211) and (020) reflections during the first charge and discharge cycle is plotted on the left. The intensities of the diffraction peaks are colour coded referring to the scale bar on top, where A.U. mean arbitrary units. The peaks highlighted in cyan represent $LiFePO_4$ and those highlighted in orange represent $FePO_4$. The horizontal axis is the selected 2θ region, and the vertical axis is the time. The corresponding voltage profile is plotted to the right.

3.3.4 Cycling $LiFePO_4$ with IL at 100°C

The ionic conductivity of the electrolyte increases with increasing temperature. At 100°C, apart from 1C and 2C (Figure 3.10, left), the IL cell works at 5C, realising 85% of the theoretical capacity, with XRD showing that the $FePO_4$ phase is fully formed (Figure 3.10, right). The Li transport in the electrolyte is the rate-limiting factor for cycling at 10C, reaching less than 20% of the theoretical capacity. It seems the cell stopped responding to the electrochemical stimuli, as evidenced by the almost stagnant XRD pattern (Figure 3.10, right).

3.3.5 Cycling $LiFePO_4$ with IL at 125°C

Cycling experiments at 125°C were solely performed with 5C and 10C rates due to the already successful results at 1C and 2C at 75 and 100°C. 10C cycling at 125°C with IL electrolyte yields more than 70% theoretical capacity (Figure 3.11, left). Both voltage profiles at 5C and 10C adopt the sloping feature at 125°C, but there is little evidence of a current-induced solid solution from the *in situ* XRD data. There is only trace, if any, the intensity between the $LiFePO_4$ and $FePO_4$ (211) peaks, indicating the presence of little intermediate solid solution phases during cycling (Figure 3.11, left).

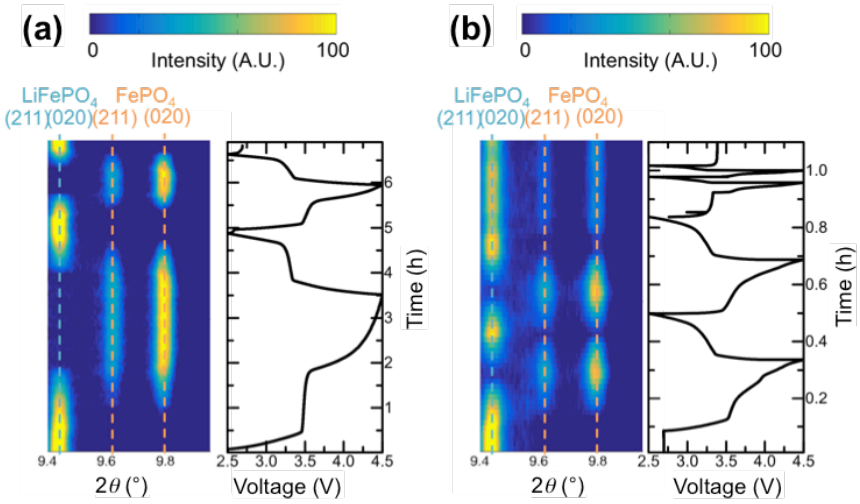

Figure 3.10. *In situ* XRD patterns collected during galvanostatic charge/discharge at (a) 1C rate for one cycles and 2C rate for one cycle at 100°C (IL electrolyte cell), and (b) 5C rate for two cycles and 10C rate for two cycles at 100°C (IL electrolyte cell). The contour plot of diffraction patterns for (211) and (020) reflections during the first charge and discharge cycle is plotted on the left. The intensities of the diffraction peaks are colour coded referring to the scale bar on top, where A.U. mean arbitrary units. The peaks highlighted in cyan represent $LiFePO_4$ and those highlighted in orange represent $FePO_4$. The horizontal axis is the selected 2θ region, and the vertical axis is the time. The corresponding voltage profile is plotted to the right.

3.3.6 Cycling $LiFePO_4$ with IL at 150°C

Cycling experiments at 150°C with IL electrolyte show similar results as the ones at 125°C. The continuous change in the two-theta position of the (211) reflection, indicating a solid solution phase transformation, is insignificant at 150°C, even at a rate of 10C (Figure 3.11, right). This indicates the suppression of a solid solution mechanism and the dominance of a two-phase mechanism. The discharge and charge capacities for the 10C cycles reaches 100% of the theoretical capacity, implying almost full utilisation of the theoretical capacity. The charging process for the 5C cycle stops and discharging starts at 4.1 V as a precaution to minimise the electrolyte decomposition at high voltages.

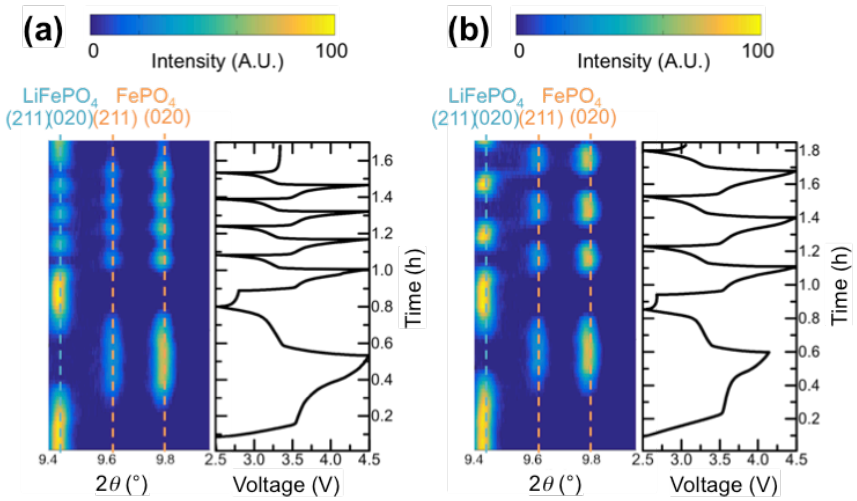

Figure 3.11. *In situ* XRD patterns collected during galvanostatic charge/discharge at (a) 5C rate for one cycle and 10C rate for four cycles at 125°C (IL electrolyte cell), and (b) 5C rate for one cycle and 10C rate for three cycles at 150°C (IL electrolyte cell). The contour plot of diffraction patterns for (211) and (020) reflections during the first charge and discharge cycle is plotted on the left. The intensities of the diffraction peaks are colour coded referring to the scale bar on top, where A.U. mean arbitrary units. The peaks highlighted in cyan represent $LiFePO_4$ and those highlighted in orange represent $FePO_4$. The horizontal axis is the selected 2θ region, and the vertical axis is the time. The corresponding voltage profile is plotted to the right.

3.3.7 Intensities of the solid solution phase at variable temperatures

The series of high-rate cycling studies on $LiFePO_4$ from 25°C to 150°C show a general trend of decreasing amount of the current-induced metastable phase with increasing temperature, as shown in Figure 3.12. The *in situ* XRD patterns of full discharge and charge, cycled at 5C at VT, are added up and stacked together, so that the intensities of the intermediate solid solution phase at VT can be directly compared. At 25°C, the accumulated (211) peak show significant asymmetric broadening, which indicates the formation of the solid solution. Also the Li poor end phase is still in the solid solution region instead of the totally delithiated $FePO_4$ as the summed XRD pattern show that the (211) and (020) peaks sit at lower angles. At 75°C, the accumulated intensity of the solid solution phase decreases. At 125 and 150°C, little amount of solid solution phase is observed. Instead, a two-phase nucleation and growth mechanism seems to dominate the phase transformations of $LiFePO_4$ at HTs when cycled at all rates explored in this study.

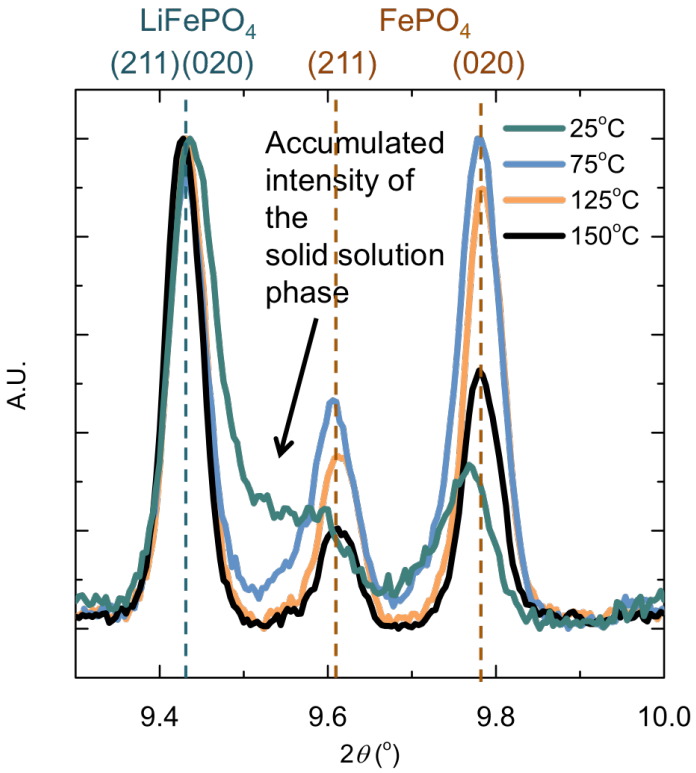

Figure 3.12. Summed *in situ* XRD patterns collected during full galvanostatic charge and discharge cycles at 5C rate at 25, 75, 125, and 150°C. The (211) and (020) reflections of $LiFepO_4$ and $FePO_4$ are highlighted in blue and brown, respectively. Asymmetric broadening is found at 25 and 75°C, corresponding to the accumulated intensity of the metastable solid solution phases.

3.3.8 Discussion of variable temperature *in situ* XRD on $LiFePO_4$

The large current during RT high rate cycling induces a high overpotential on $LiFePO_4$ particles to transform via dynamic single-phase solid solutions rather than forming phase boundaries. The high currents "force" enough particles to transform via this route that the intermediate solid solution state is detectable using XRD. This results in particles of different Li compositions being present during charge and discharge. The distribution of Li compositions leads to distributions of lattice parameters for the respective Li_xFePO_4 phases and causes asymmetric peak broadening. Reflected in the XRD patterns is the continuous change of peak positions of Li_xFePO_4.

The two-phase mechanism competes with the aforementioned metastable single-phase mechanism at high rates at all temperatures. At 125 and 150°C, the number of particles at the intermediate metastable phase is smaller than that at RT, leading to less XRD intensity. Given that there is enough energy in the system to activate the non-equilibrium solid solution phase transition of $LiFePO_4$ at RT, HT should further aid the system to surpass the energy difference between single particles and particles with phase separation. Therefore, it should be kinetic arguments that play a role in the enhanced phase separation at HT. One possible explanation is that Li diffusion at 125 and 150°C is much faster than that at RT and, therefore, Li-ion diffusion and a clustering to particles happens at a faster rate. Because of the faster diffusion rate, the metastable single-phase particles are easier to phase separate into either $LiFePO_4$ or $FePO_4$, reducing the number of XRD detectable particles at the metastable state at HT. As a result, the current induced solid solution mechanism of $LiFePO_4$ is suppressed at 125 and 150°C. This is comparable to the temperature effect on the lithiation process of anatase TiO_2, in which the rate-induced Li solubility is also found to be less pronounced at higher temperatures and the reason is attributed to the finite Li diffusivity in the TiO_2 phases.[168]

Notably, a second sloping plateau during charge is present in many cases for temperatures from ambient to 150°C, in both organic and IL electrolyte. This phenomenon is due to the electrochemical window of the electrolyte and related to the electrolyte decomposition, and, therefore, does not influence of the XRD result since the phase transformation is associated with voltages below 4.0 V.

3.4 Conclusions and outlook

The new VATIC system is designed to perform HT *in situ* XRD experiments on batteries. The wide temperature range of this design massively expands the temperature range that *in situ*

XRD measurement can be carried out, complementing existing *in situ* XRD sample environments that are designated for RT use only.

The VATIC setup proves to be a powerful tool to study the phase information, phase transformation mechanism and dynamics of battery electrode. It has good electrochemical performance, good sealing, homogeneous stack pressure, and is X-ray transmissive at VT.

RT high rate cycling of $LiFePO_4$ in the VATIC has reproduced the asymmetric broadening observed by Liu, et al. in the state-of-art RT *in situ* XRD cell,[77] verifying the cell performance. The suppression of the current induced metastable phase at elevated temperatures was observed utilising the VT capability of VATIC. The suppressed solid solution behaviour implies a possible competing phase transition mechanism between the current induced single-phase solid solution and two-phase nucleation and growth, governed not by thermodynamics but by kinetics, possibly Li diffusion rate.

At the same time, the cause of the IL $LiFePO_4$ battery failure at 75 and 100^{o}C was identified using the VATIC setup. The majority of the bulk electrode is not accessed at these temperatures at very high rates due to the insufficient ionic conductivity of the IL electrolyte at these temperatures, and therefore, the battery exhibits very little capacity.

Note that the HT *in situ* XRD system is also compatible with other X-ray techniques, for instance, absorption, total scattering, and pair distribution function. Nevertheless, these application scenarios have not been tested on the newly designed system and thus out of the scope of this thesis.

4 Complex (de)lithiation mechanism of V_6O_{13} at room temperature

The high capacity material V_6O_{13} remains a candidate of great potential in the field of Li polymer and all solid-state batteries utilising Li anodes. Therefore, comprehensive knowledge on the complex phase transformation mechanisms during discharging and charging this material in a LIB is of great interest. *In situ* synchrotron XRD was carried out to probe this phase transformation mechanism of V_6O_{13} at RT. DFT calculations and NMR spectroscopy were used to complement the XRD techniques, and give more insights into the structural and electronic changes in the material during (dis)charge. Roberta Pigliapochi is greatly acknowledged for doing the DFT calculation that is shown in Section 4.3.

4.1 Complex electrochemistry

4.1.1 First cycle discharge/charge at room temperature

The first galvanostatic discharge and charge cycle of V_6O_{13} against Li, performed at a rate corresponding to C/10 during the *in situ* XRD experiment, is shown in Figure 4.1 along with the d*Q*/d*V* plot. Both the discharge and charge voltage profiles contain multiple plateaus, which indicates multiple intercalation and deintercalation processes. The d*Q*/d*V* plot shows four reductive peaks at 2.70, 2.54, 2.47, and 2.10 V upon discharge, and only three oxidative peaks at 2.22, 2.64, and 2.78 V upon charge, suggesting an asymmetric (de)lithiation process. Vanadium is reduced via at least four stages and oxidised via three, which suggests that the Li insertion and extraction processes do not simply involve redox steps between redox couples V^{5+}/V^{4+} and V^{4+}/V^{3+}.

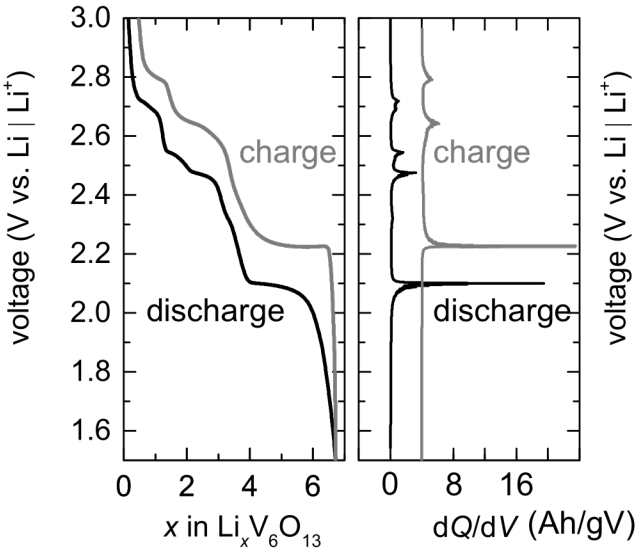

Figure 4.1. Voltage profile (left) and d*Q*/d*V* plot (right) of V_6O_{13} during first discharge (black) and charge (grey) cycle. The absolute value of d*Q*/d*V* is shown (i.e., negative for discharge) and the d*Q*/d*V* of charge is offset by 4 Ah/gV. The battery is cycled in an AMPIX cell[135] at a rate of C/10 at room temperature. Plateaus in the voltage profile correspond to reductive/oxidative peaks in the d*Q*/d*V* plot. Four stages of intensive Li intercalation appear at 2.70 V, 2.54 V, 2.47 V, and 2.10 V, while deintercalation only exhibits three stages at 2.22 V, 2.64 V, and 2.78 V.

4.1.2 Cycle life and rate dependency tests

The capacity of V_6O_{13} keeps deceasing during cycle life tests, and the rate dependency tests show that the material is not ideal for high rate cycling (above 1C). The highest capacity V_6O_{13} can achieve at low rates (C/20) at RT is 375 mAh/g. The capacity decays by 13% to 325 mAh/g in the first 15 cycles (Figure 4.2). The stepwise electrochemistry remains but each plateau shortens during these cycles. Blockage of Li ion channels in the crystal structure, electrode active material dissolution and side reaction product blockage can possibly result in this kind of capacity decay. The capacity drops discontinuously between C/20 and C/10 and reaches only 250 mAh/g by the end of the 25th cycle at C/10. In the latter cycles, higher rates result in more capacity drops. While cycling at C/5 can still achieve 50% of the theoretical capacity, further increasing the cycle rate to 1C leads to only 17% of the capacity retention. When cycling at 2C, less than 10% of the theoretical capacity can be achieved. The cycle rate was reset to C/20 after the 55th cycle (at 2C). The cell was able to gain a discharge capacity at 275 mAh/g in the 57th cycle, dropping quickly to 200 mAh/g in 5 more cycles. The quick capacity decay suggests that there is possibly irreversible structural change in the material when being cycled at high rates and over a long period of time.

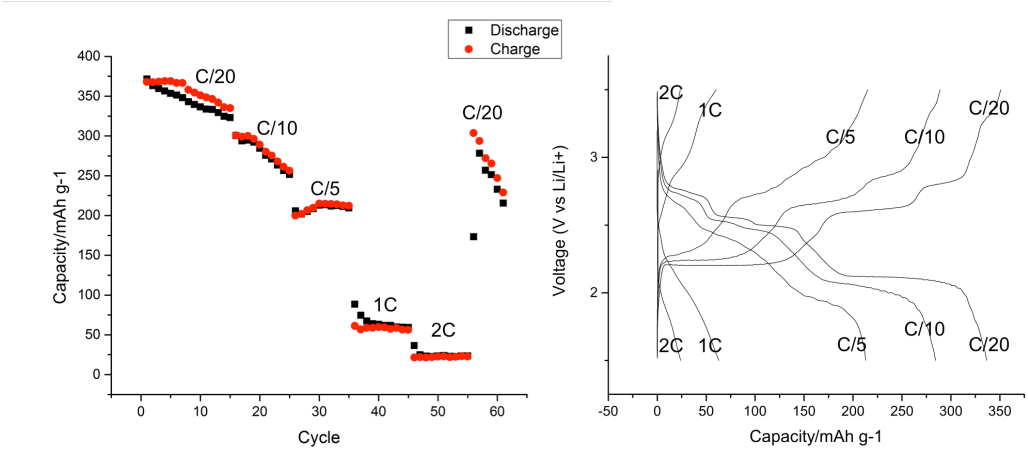

Figure 4.2. Cycle life and rate dependency test of V_6O_{13}. The specific capacity vs. cycle number plot (left) and voltage vs. specific capacity plot (right) of V_6O_{13} during the first 60 cycles suggest that the capacity of V_6O_{13} decays with cycling and the specific capacity decreases drastically during high rate cycling.

The stepwise electrochemistry at C/20 and C/10 show similar features. When the cycle rate reaches C/5, the clear-cut electrochemistry starts to smear out. Further increment to the cycle rate results in further smearing out of the voltage profile, suggesting changes in battery working mechanism or electrode morphology such as particle sizes.

However, the high capacity and medium voltage range of V_6O_{13} still makes it a good contender for electrode material in polymer or all solid-state batteries. The cycle rate retention issue can be addressed by more careful electrode composition and morphology optimisation. The only criteria remains is the performance of V_6O_{13} at elevated temperature.

4.1.3 Electrochemical tests at high temperature

Cycling V_6O_{13} at C/10 at HT (100^{o}C) leads to a higher specific capacity (430 mAh/g). The underlying mechanism of the extra capacity at HT will be analysed in Chapter 5. The HT cell is able to achieve 90% cell capacity retention after 30 cycles (Figure 4.3). However, the stepwise electrochemistry also smears out after the 20th cycle.

The HT discharge and charge multicycle test proves that V_6O_{13} is indeed a promising candidate for polymer or all solid-state batteries working at HT. Even though the electrochemistry features change over extended cycles, the cycle life retention HT is quite satisfactory and a specific capacity of 385 mAh/g (better than the highest specific capacity gained at RT) can still be achieved after 30 cycles.

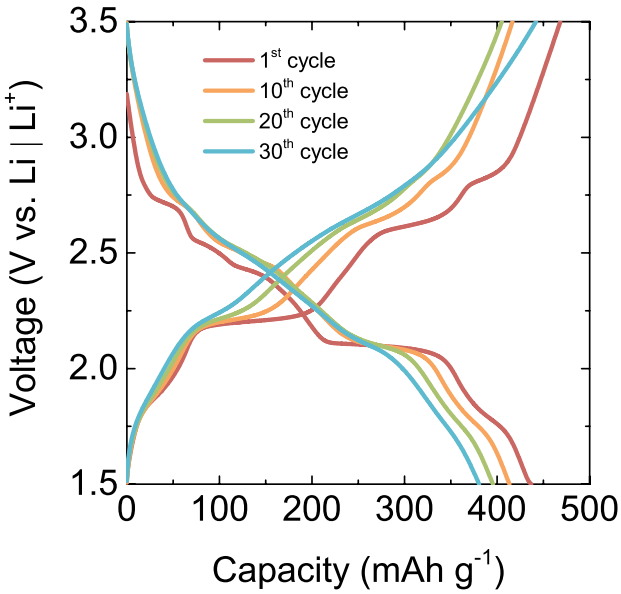

Figure 4.3. Voltage profile of the first 30 cycles of V_6O_{13} batteries at C/10 at 100°C. The first cycle (red) has a discharge capacity of 430 mAh/g, 15% more than that of the specific capacity gained at RT. The stepwise electrochemistry smears out from the 20th cycle (green) but the cell is able to retain 90% of its original capacity after 30 cycles.

4.2 Phase transformations revealed by *in situ* XRD

In situ XRD patterns collected during the first discharge and charge cycle of V_6O_{13} at a rate of C/10 reveal the various phases the material evolves through, as shown in Figure 4.4. The background contributions from the conducting carbon, PTFE binder and cell are subtracted for clarity. In single-phase regions, all diffraction peaks can be indexed to a space group of *C2/m*. The highlighted reflection (110), (003) and (020) in Figure 4.4 are representative of the structural change of the material. In regions (a), (c), (e), (g), and (i), these three peaks shift continuously, indicating a single-phase solid solution mechanism; in regions (b), (d), (f) and (h), they show discontinuous behaviour, where the respective peak of the existing phase disappears while that of the incipient phase grows indicating a two-phase nucleation/growth mechanism.[46] This analysis suggests an alternating single-phase interstitial solid solution and two-phase nucleation/growth mechanisms which involves at least four different phases. Using the nominal compositions calculated from electrochemical data, the single-phases contain phase 1 ($0 \leq x < 1.7$), phase 2 ($1.7 \leq x \leq 2.1$), phase 3 ($3.0 \leq x \leq 4.6$), and phase 4 ($6.2 \leq x \leq 6.7$), and the two miscibility gaps are at $2.1 < x < 3.0$ and $4.8 < x < 6.2$, between phases 2 and 3 and phases 3 and 4, respectively.

The lattice parameters extracted from *in situ* XRD data using Pawley refinement confirm the aforementioned alternating structural evolution mechanism and provide more details on the

intercalation and deintercalation asymmetry (Figure 4.5 and Figure 4.6). They are also in line with the previous $Li_{0.67}V_6O_{13}$,[121] LiV_6O_{13},[121] $Li_2V_6O_{13}$,[122] $Li_3V_6O_{13}$,[123] and $Li_{3.25}V_6O_{13}$,[124] single crystal studies (Figure 4.6) at the relevant specific points on the discharge curve. Because the change of lattice parameters are very sensitive to the Li positions and the Li position refinement using our powder XRD data is not feasible, the following discussions regarding the Li positions are based on the knowledge of previous single crystal data for $Li_xV_6O_{13}$ ($x \leq 3.25$) and our DFT calculations for $Li_xV_6O_{13}$ with higher Li-content.

4.2.1 First discharge

During the discharging process, as much as 6.7 Li can be inserted into one unit formula V_6O_{13}, which results in cell volume expanding by 14.8% (Figure 4.5). As Li is intercalated into phase 1, the volume, *Vol,* change is negligible for $0 \leq x < 0.75$ but increases significantly by 3.9% for $0.75 \leq x < 1.7$, suggesting it may be appropriate to subdivide the phase 1 Li intercalation process into two sub-processes (which are named as phase 1a and phase 1b). The voltage in phase 1a remains almost constant at 2.7 V but drops noticeably from 2.7 to 2.5 in phase 1b region. This is also consistent with the splitting in the dQ/dV peak at 2.7 V, and the prior crystal structures where the compositions x = 2/3 and 1 were associated with different Li-vacancy orderings and superstructures[121]. Between phase 1a and phase 1b, there is no discontinuity in the volume expansion, but a discontinuity in the first-order derivative of the volume vs. composition, d*Vol*/d*x.* The same change happens beyond $x = 1.7$, where a second sharp increase in volume is seen for $1.7 \leq x < 2.1$, (of 2.7%). On this basis, it is suggested that there is another second order phase transition between phase 1 and a second phase (phase 2), at approximately x = 1.7. The diffraction changes lag slightly behind the electrochemical signatures, which is a phenomenon that is often observed when cycling under non-equilibrium conditions.

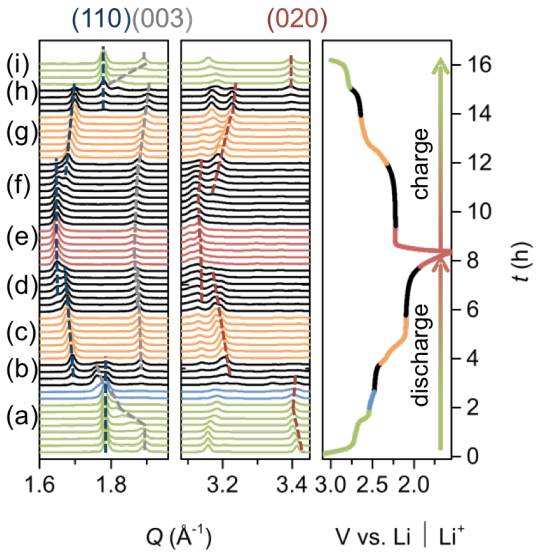

Figure 4.4. *In situ* synchrotron XRD of the first discharge and charge cycle of V_6O_{13}. Coloured lines correspond to single-phase regions, and black lines correspond to two-phase regions. The different states of discharge and charge are denoted as (a) – (i). The (110), (003) and (020) reflections can be tracked to monitor the structural changes during electrochemical cycling. Continuous shifts in peak positions are characteristic of single-phase solid solutions (a, c, e, g, i), while the growth and disappearance of peaks are characteristic of two-phase nucleation and growth (b, d, f, h). The asymmetry in the discharge and charge profiles is demonstrated by the fact that (003) reflection crosses (110) on discharge but does not cross on charge.

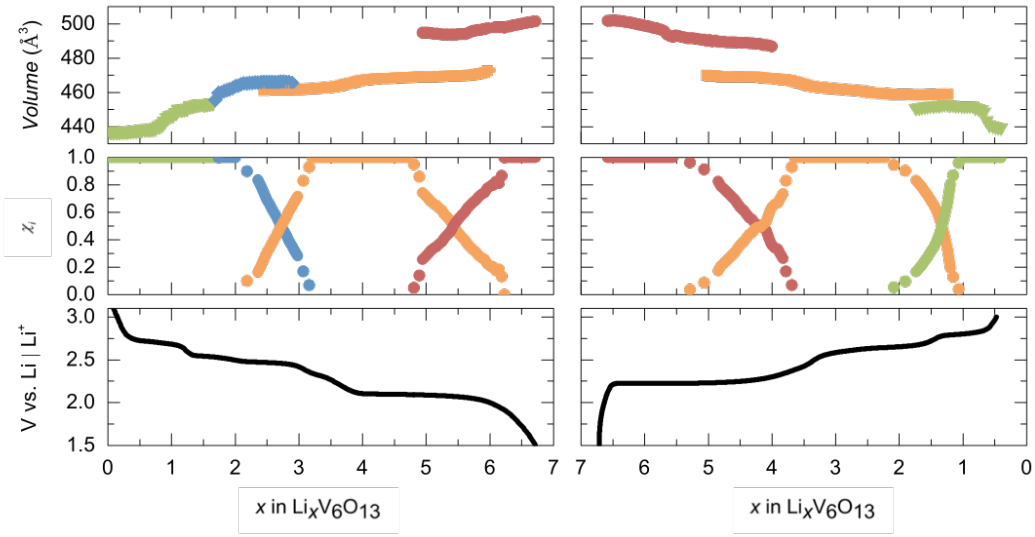

Figure 4.5. Evolution of unit cell volumes and phase fractions χ_i of the four observed phases during the first discharge (left) and charge (right) cycle of V_6O_{13}. The unit cell volume progressively increases upon discharge as Li is incorporated, and decreases upon charge. The continuous change in unit cell volume from phase 1 (green) to phase 2 (blue) on discharge is characteristic of a second order phase transition; phase 2 is not observed on charge. The orange points correspond to phase 3 and red to phase 4. The discontinuous change in volume and growth of new phases is characteristic of a nucleation and growth mechanism, which operates in all other transformations. Phase fractions determined by powder XRD analysis are unreliable at low χ_i, though estimates are shown using sparse dots.

A first order phase transition from phase 2 to phase 3 takes place at x = 2.1 and continues to x = 3.0, which is indicated by peaks of phase 2 diminishing and those of phase 3 increasing. This first order phase transition is associated with a flat potential profile at approximately 2.45V, characteristic of a two-phase reaction. In phase 3 region until approximately *x* = 5, the volume change is small. (Similar to the structural transformations in phase 1, while continuous, those of phase 3 could potentially be divided into two regions, phase 3a and b, on the basis of the distinct change in both voltage and cell volume at approximately x = 3.5). Phase 4 is formed from phase 3 in a second first order phase transition from 4.8 to 6.2, which is associated with a flat potential region at 2.10V and discontinuity of the volume.

4.2.2 First charge

Li is deintercalated from $Li_{6.7}V_6O_{13}$ and $Li_{0.4}V_6O_{13}$ is formed at the end of charge, where the Li composition is determined by assuming all current measured during discharge/charge corresponds to insertion/extraction of Li into the material. By the end of charge, the unit cell volume determined by XRD is restored to the same value as that of pristine V_6O_{13}. Based on the knowledge that up to 0.7 Li insertion into V_6O_{13} formula unit does not cause much volume change, this 0.4 Li may be trapped in the V_6O_{13} lattice. However, since this is a first cycle performance test and the cell is not rested for long to allow time for the surface reaction that takes place at the solid electrolyte interface after cell assembly. This residue 0.4 Li may also be associated with the solid electrolyte interface formation during the first discharge.

During charging, the material evolves through five steps, which include three single-phase solid solutions (Figure 4.5), namely phase 4 ($5.6 \leq x \leq 6.7$), phase 3 ($2.3 \leq x \leq 3.8$), and phase 1 ($0.4 \leq x \leq 1.4$) and two miscibility gaps ($1.4 < x < 2.3$, $3.8 < x < 5.6$). Both transitions from phase 4 to phase 3 and phase 3 to phase 1 are first order. One notable feature on charge is that phase 2 is not observed, which results in an asymmetric electrochemical cycling mechanism. The reasons for this asymmetry are discussed below.

4.2.3 Sequential change of lattice parameters

Further analysis of lattice parameters reveals in detail its sequential change and the reasons behind as shown Figure 4.6 and Figure 4.7. Two features are present:

1) *Each solid solution phase expands/shrinks in a preferred direction.*

The light lithiated phases, phase 1 and phase 2, change along the *c* direction when (de)lithiated. The *c* lattice parameter of phase 1 expands by 4.5% on discharge and shrinks by 3.6% on charge. Phase 2 elongates in *c* by 2.5% on discharge, while it is bypassed entirely

on charge. The *b* lattice parameter of phase 3 increases by 1.6% on discharge and decreases by 1.9% on charge. In phase 4, the *a* lattice parameter expands by 1.2% on discharge and shrinks by 2.4% on charge.

2) *First order phase transitions are accompanied by abrupt changes of lattice parameters in one or more directions.*

The first-order phase transformation between phase 2 and phase 3 on discharge and its counterpart on charge (phase 3 to phase 1) result in lattice parameters *b* and *c* to change abruptly in opposite directions. For example, compared with phase 2, phase 3 is 6.1% larger in *b* and 6.8% smaller in *c*. The first-order transition between phase 3 and phase 4 causes abrupt change only along the *a* direction, either 3.3% longer on discharge or 2.4% shorter on charge. The changes in unit cell parameters extracted from our *in situ* powder XRD data are consistent with previous single crystal studies (Figure 4.6),[119,122,123] and the evolution in unit cell parameters is attributed to changes in V–O bond distances with incorporation of Li in between the VO_6 layers (Figure 1.9) and the concomitant addition of electrons to the different t_{2g} orbitals, which is analysed using DFT calculations and prior single crystal studies.

4.3 Linking structural changes with electronic structure via DFT

The low energy structures from V_6O_{13} to $Li_9V_6O_{13}$ predicted by the computational structural search, as detailed in Chapter 2, Section 2.4, show correlation between the Li positions and formation energy of different structures (Figure 4.8). The availability of a series of low energy structures with the same composition allows the effect of Li positions and electronic structure on the V-O distances and cell parameters to be explored, and the lattice parameters of $Li_xV_6O_{13}$ are found to be highly sensitive to the Li positions. Although the Li(1) site was not directly included in the initial enumeration of the DFT structures, it was found to be present in a number of the structures after geometry optimization.

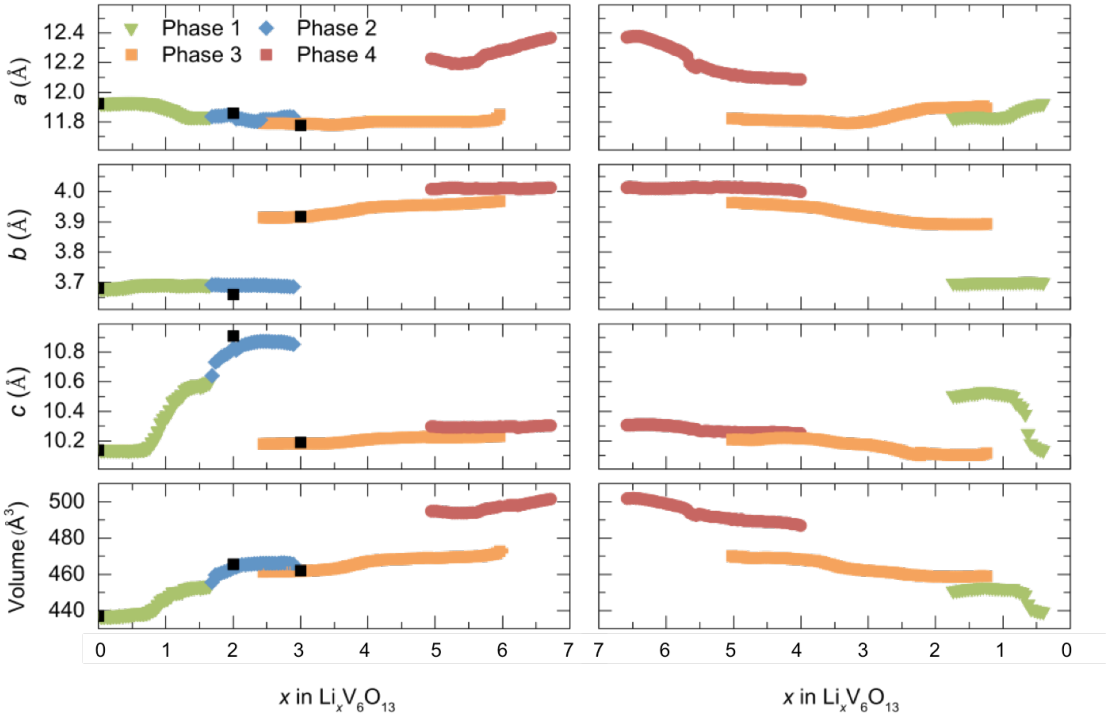

Figure 4.6. Evolution of lattice parameters of the four phases observed during the first discharge (left) and charge (rig). The unit cell expansion is driven by sequential growth along a preferred direction of the unit cell. The black dots are lattice parameters from single crystal studies.[119,122,123] While one unit cell parameter increases dramatically; the others remain relatively unchanged. Li incorporation upon discharge is accommodated first by elongating the *c* lattice parameter by 7.0%, after which expansion occurs predominantly in the *b* lattice parameter (1.6%), and finally the *a* lattice parameter (3.3%). The reverse process is mirrored upon charge.

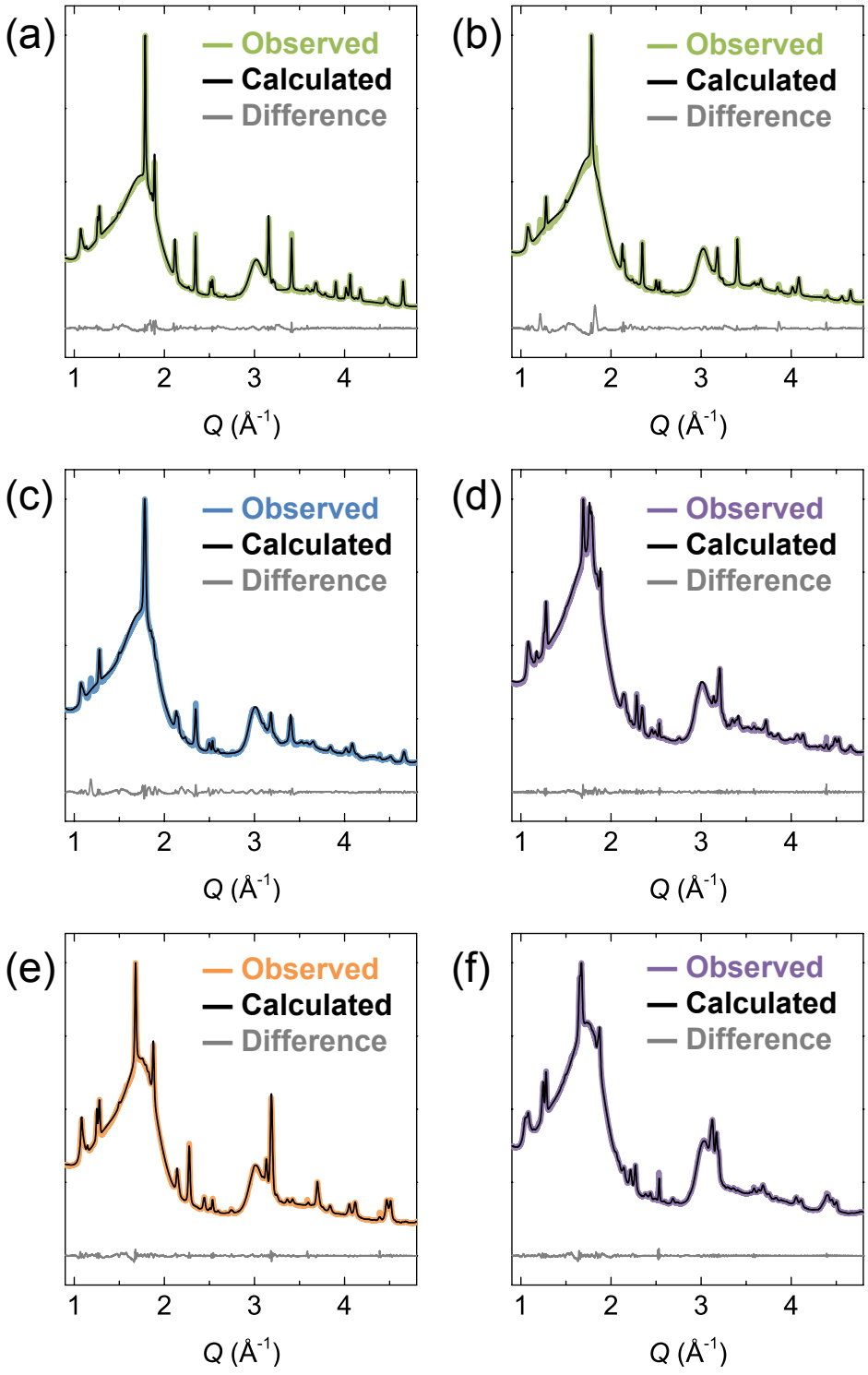

Figure 4.7. Typical whole powder fitting results of *in situ* XRD patterns of $Li_xV_6O_{13}$ formed on discharge, with (a) x = 0, (b) x = 1.2, (c) x = 2.0, (d) x = 2.6, (e) x = 3.8, (f) x = 5.5. Experimentally observed patterns of phase 1, phase 2, and phase 3 are colour coded green, blue, and orange respectively, while patterns within two-phase regions are colour coded purple. All fitted patterns are in black and the differences between observed and calculated patterns are in grey.

4.3.1 Phase 1

Both the LiV_6O_{13} structures built initially containing 1 Li atom per cell in either the Li(3) or Li(5) sites relaxed after structural optimization (and energy minimization) to cells containing Li on the Li(1) sites; this indicates that the calculated lowest energy structure of LiV_6O_{13} contains Li only on the Li(1) sites and is in agreement with the single crystal study (Figure 4.8).[121] Note that the primitive cells computed in the DFT analysis contain only one Li atom per LiV_6O_{13} formula unit and the specific alternation of Li(1) occupancy reported in the single crystal study could not be captured in our DFT analysis, which would require a doubling of the unit cell in the *a*-direction.[121] Our results nonetheless confirm that the Li(1) position is the one that is preferentially occupied at this early stage of lithiation.

4.3.2 Phase 2

In $Li_2V_6O_{13}$, (i.e., a composition within phase 2), the lowest energy DFT structure shows half occupancy in both Li(2) and Li(5) sites, which varies from the single crystal structure where only Li(1) sites are fully occupied. Full occupancy of the Li(1) site results in a significant expansion of the cell along the *c* axis of 8.5% in the DFT-derived structure, which is in agreement with the lattice parameter changes obtained experimentally in our *in situ* XRD. The lowest energy structure found with DFT, on the other hand, shows a much-reduced expansion along the *c* axis (2.7%). The single crystal derived (Li(1) containing) DFT-structure and the lowest energy structure differ in energy per atom by only 5 meV. This energy difference is within thermal energy at room temperature (k_BT = 26 meV), and the structures are both considered accessible at room temperature, as well as within DFT error. A more careful analysis of the effect of temperature, using, e.g. phonon calculations within the harmonic approximation, would be needed in order to fully assess the relative stability of these structures with temperature. Given the subtle energy differences, the kinetics associated with Li reorganization and concomitant distortions of the VO_6 layers (as discussed below) may also play a role in dictating the observed Li-ordering schemes.

The single crystal diffraction studies of V_6O_{13} and $Li_2V_6O_{13}$[119] show that the space between single and double VO_6 layers increase upon initial Li insertion. The Li ion is inserted into Li(1) (Figure 1.10) closest to the V(1) site, which accommodates the Li ion insertion by changing from an octahedral VO_6 geometry to a square pyramidal VO_5 geometry. It is proposed that electrostatic contributions are the dominant contributions to these changes in vanadium environment. V(1) in the single VO_6 layers is reduced upon lithiation, resulting in an increase in the average V(1)-O bonding distance. Secondly, V(1) moves away from the centre of the

VO_6 octahedron to minimize the electrostatic repulsion from the nearby Li ion, leading to increased vanadium site distortion and ultimately a change to 5-coordinate vanadium. When probed using *in-situ* XRD, the long range structure exhibits a progressive lengthening in *c.* Therefore, in phases 1 and 2, Li ions likely diffuse through the channels in the *b* direction, as proposed by previous impedance studies,[109] and sit in Li(1) sites located in these channels *between* the layers, as shown in Figure 4.9.

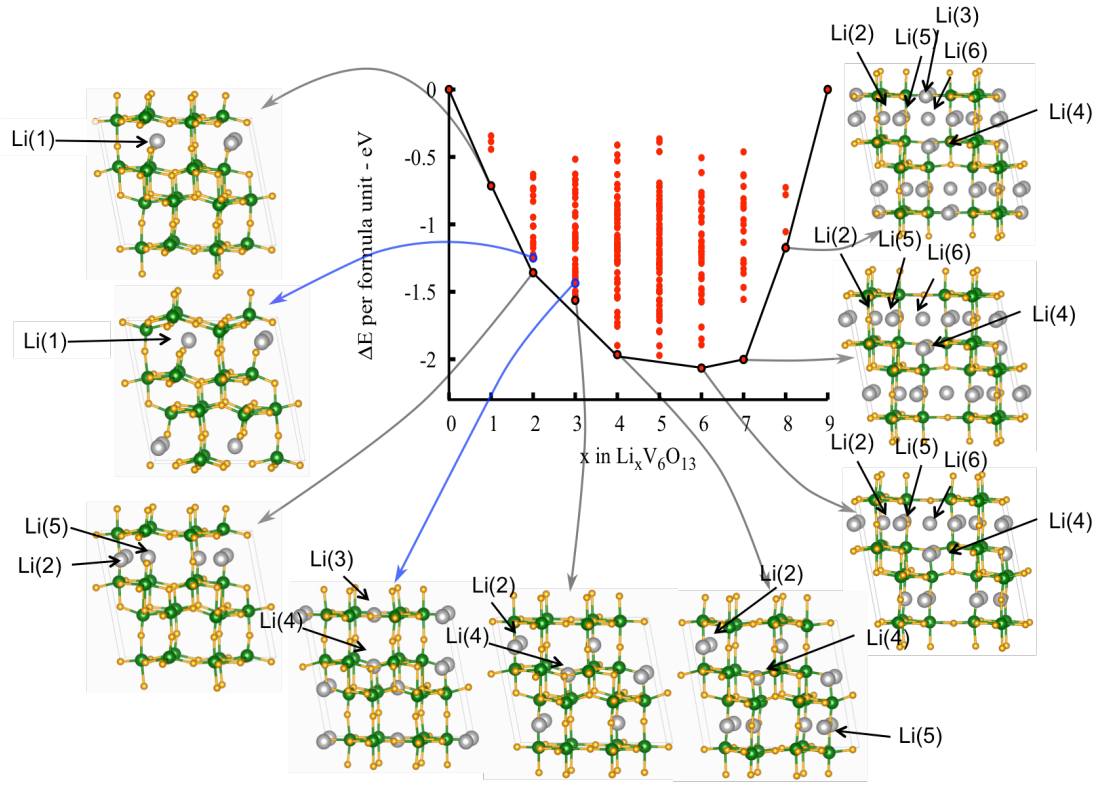

Figure 4.8. Formation enthalpy per formula unit versus the fractional Li concentration in $Li_xV_6O_{13}$. The convex hull, indicated by the line, is constructed by joining the stable structures obtained by the searches. The grey, green and yellow spheres in selected structures represent Li, vanadium, and oxygen centres respectively. The structures with the lowest energy for LiV_6O_{13} to $Li_9V_6O_{13}$ (circled by black), as well as the structures with the single crystal Li-site occupancies for $Li_2V_6O_{13}$ and $Li_3V_6O_{13}$ (indicated by blue circles and arrows) are shown.

4.3.3 Phase 3

When all the Li(1) sites are filled at around x = 2, a phase transition occurs to form phase 3 which is associated with the abrupt rearrangement of the Li ions in the structure to sit within new sites in the single and double layers according to single crystal diffraction data for $Li_3V_6O_{13}$ (Li(3) and Li(4) sites in Figure 4.9).[123] The lattice parameters of this new phase (phase 3) are substantially different from the previous one (phase 2): the Li ions no longer sit between the planes along the *c* direction, which leads to an abrupt decrease in the *c* unit cell parameter. The single-crystal derived VO_x structure of phase 3 is very similar to that of the pristine V_6O_{13} material, except for a substantial elongation in *b* direction. Li ions form square planar geometries with surrounding oxygen ions in Li(3) and Li(4) sites and this causes an expansion along *b* (Figure 4.9), the distance between the diagonal oxygen ions along *b* on the edge of the cavity in layer A expanding from 3.66 to 3.92 Å from phase 2 to phase 3, on the basis of the single crystal studies.[122,123] This approximately 6.5% change matches well with the expansion of the *b* unit cell parameter observed using *in situ* XRD (6.1%). Further lithiation into phase 3 causes further expansion along the *b* direction.

As shown in Figure 4.8, all of the low energy structures of $Li_3V_6O_{13}$ predicted with DFT contain occupancy of the Li(4) site, and they all show more than 4% elongation along *b,* with respect to the *b*-parameter of V_6O_{13}. Among these structures, the $Li_3V_6O_{13}$ configuration that resembles the lattice parameter changes derived from the *in situ* XRD (only *b* changes by almost 6%, while *a* and *c* remain unchanged) is the DFT structure having full occupancy of the Li(3) and Li(4) sites. This configuration also corresponds to the Li occupancy obtained from the single crystal study. However, the lowest energy structure calculated with DFT is found to have half occupancy of the Li(4) sites and full occupancy of the Li(2) sites. Again, the difference between the lowest energy structure and the configuration that reproduces both the in situ XRD refinement and the single crystal study is minimal (6 meV), and the two structures are considered within DFT error as well as within thermal energy.

Of note, the structural rearrangements upon lithiation are associated with a redistribution of electrons within the vanadium *d* orbitals, shown by our DFT calculations and illustrated in Figure 4.10 for x = 0, 1, 2 and 3 (for the DFT structures with Li site occupancies and cell parameters that are closest to those of the single-crystal derived structures). Spin density maps were generated from the (spin-polarised) DFT calculations and illustrated with isosurfaces, spin-density illustrating reduction of the diamagnetic V^{5+} ion. The change in oxidation states of the vanadium sites on lithiation was analysed by comparing charge density of the different $Li_xV_6O_{13}$ systems with those of the starting material V_6O_{13}. In the

pristine V_6O_{13} phase, the V(2) sites are all V^{5+}, as previously reported[119], while the unpaired electron on each of the V(3) sites is localized in the d^1_{xy} orbital. The orbital ordering of the V^{4+} V(1) centres, on the other hand, shows an alternation of d^1_{xz} and d^1_{yz} orbitals along the single layer. A previous study has shown that V_6O_{13} has a metal insulator transition at 150 K and the symmetry is lower in the low temperature phase.[170–172] Given this material is metallic at room temperature, it is likely that this orbital ordering does not persist at ambient temperatures. During the next stages of lithiation to LiV_6O_{13} (within phase 1), the V(2) sites close to the Li inserted in Li(1) remain V^{5+}, while the other V(2) sites, opposite to the inserted Li, are reduced to V^{4+}, with the unpaired electron localised on a d^1_{yz} orbital. Similarly, the V(1) sites close to the occupied Li(1) site now show d^1_{xy} orbital occupancy, while the remaining V(1) remains d^1_{yz} , as in pristine V_6O_{13}. In the next stage of lithiation to $Li_2V_6O_{13}$ (within phase 2), the V(2) sites are reduced to V^{4+}, resulting in an alternation of V(2)-d^1_{xy} and V(3)-d^1_{yz} orbitals in the vanadium double layer, which is related to the different distance of V(2) and V(3) to the fully occupied Li(1) sites. The V(1) sites, now all at equal distance from the Li(1) centres, contain their unpaired electrons localized on the d^1_{xy} orbitals. These changes in the distribution of the electron density determine the elongation of both the V(1)-V(2) distance and even more so the V(1)-V(3) distance, reflecting the *c*-expansion reported for the whole range from V_6O_{13} to $Li_2V_6O_{13}$. In the next step of lithiation (to form phase 3, $Li_3V_6O_{13}$), calculations show that the V(1) sites are preferentially reduced from V^{4+} to V^{3+}, resulting in an alternation of d^2 (d^1_{xy}-d^1_{yz} or d^1_{xy}-d^1_{xz}) and d^1_{yz} orbital ordering along the single layer. The V(2) and V(3) centres are now both of d^1_{xy} configuration. The redistribution of charge density determines an elongation of the V(1)-V(1) distance along *b*, and a contraction of the V(1)-V(2) distance along *c*, consistent with the lattice expansion associated with this transition, as described earlier. The alternation of d^2 and d^1_{xz} in the V(1) single layer is very sensitive to the position of the Li(3) sites, as shown in detail in Figure 4.11. The $Li_3V_6O_{13}$ single crystal X-ray refinement[123] showed disorder on the Li atom situated on the inversion centre in the single layer – the Li(3) site, and the structure was modelled with a split position generating sites 0.3Å above and below the single layer. Different $Li_3V_6O_{13}$ structures with Li(3) off-centred within this range were simulated with DFT. Following geometry relaxation, the change in the unit cell parameters is less than 1%, and the difference in energy per atom is less than 8 meV, suggesting that these configurations are degenerate at room temperature.

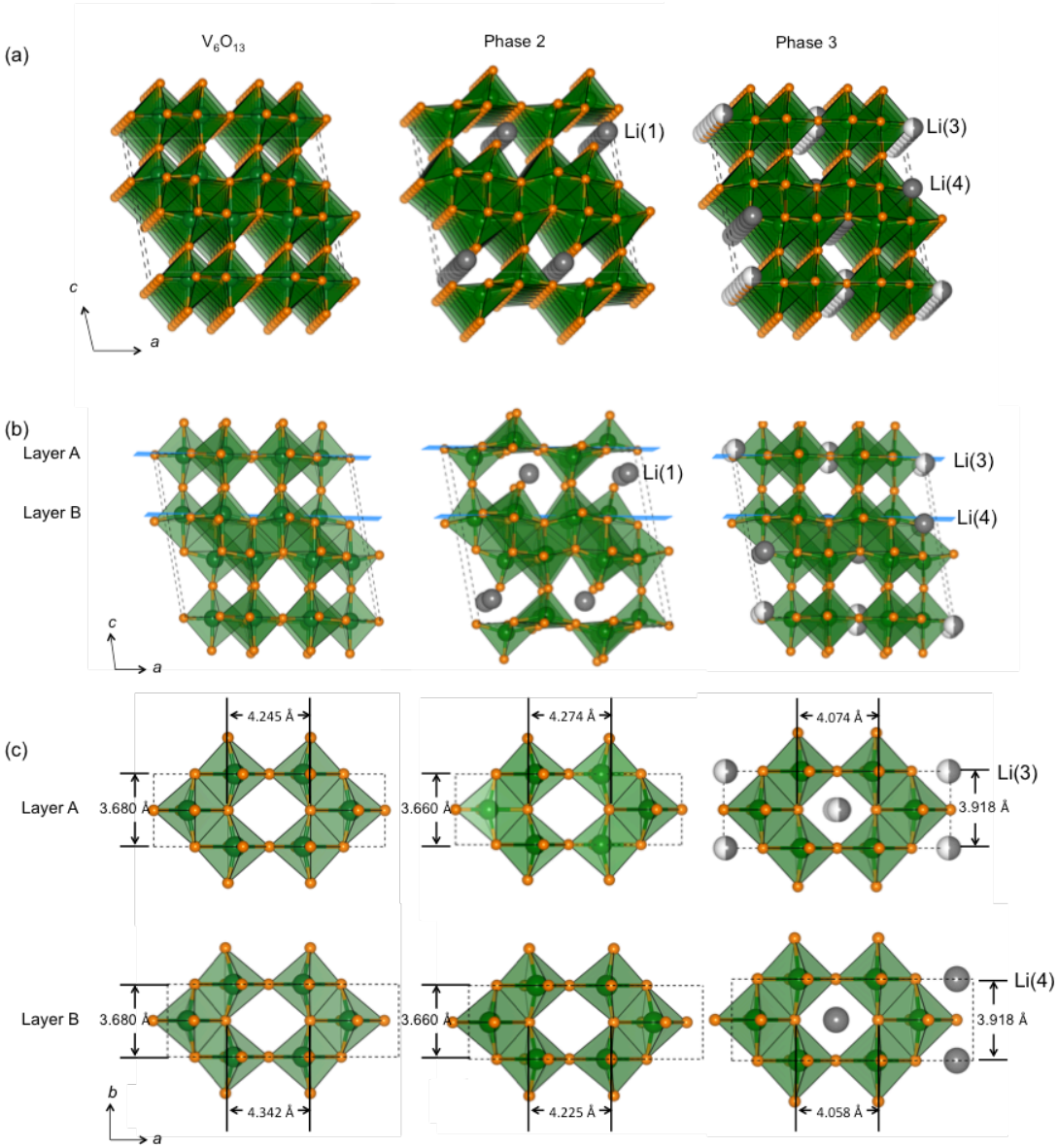

Figure 4.9. VO_x structure and Li ion positions of the single crystal XRD determined pristine, unlithiated structure[119], phase 2[122] and phase 3[123]. Vanadium, oxygen, and lithium atoms are represented by green, orange and grey spheres, respectively. Black and dashed lines indicate the edges of polyhedra and unit cells. **(a)** The Li ions diffuse along the *b* direction and sit between layers in phase 2 in the Li(1) site. In phase 3, Li ions rearrange and sit within both single and double VO_x layers. **(b)** The positions of the single (Layer A) and one of the double layers (Layer B) of phase 1 (pristine), phase 2, and phase 3, and **(c)** the *ab* plane view of them. The interstitial cavity inscribed by planes of oxygen atoms has a high aspect ratio of approx. 1.17 (1.15 for single layers and 1.18 for double layers) prior to lithiation, which decreases to 1.04 in phase 3. According to simple geometrical principles, the structure expands along the short *b* axis and shrinks along the long *a* axis in order to obtain the maximum interstitial cavity volume with minimum necessary structural distortion.

Upon further lithiation in the whole phase 3 region from $Li_3V_6O_{13}$ to $Li_{4.8}V_6O_{13}$, *in situ* powder XRD shows that *b* expands continuously by 1.6%. Based on the DFT results on the $Li_4V_6O_{13}$ structures, the cells that show a major expansion along *b* (about 5% with respect to V_6O_{13}),

and minor changes along *a* and *c* (below 2% with respect to V_6O_{13}) are the ones having full or partial occupancy of Li(2), and full or partial occupancy of Li(3), Li(4) or Li(5), with the lowest energy structure having full Li(2) and half Li(4) and Li(5) occupancy. Among the other low energy structures, isotropic expansion along *a*, *b* and *c* of around 3% is observed for partial occupancy of Li(2), Li(5) and Li(6), while significant expansion (around 5%) of the *a* axis is observed when Li is present on the Li(1) site, trends which are not consistent with the *in situ* XRD results.

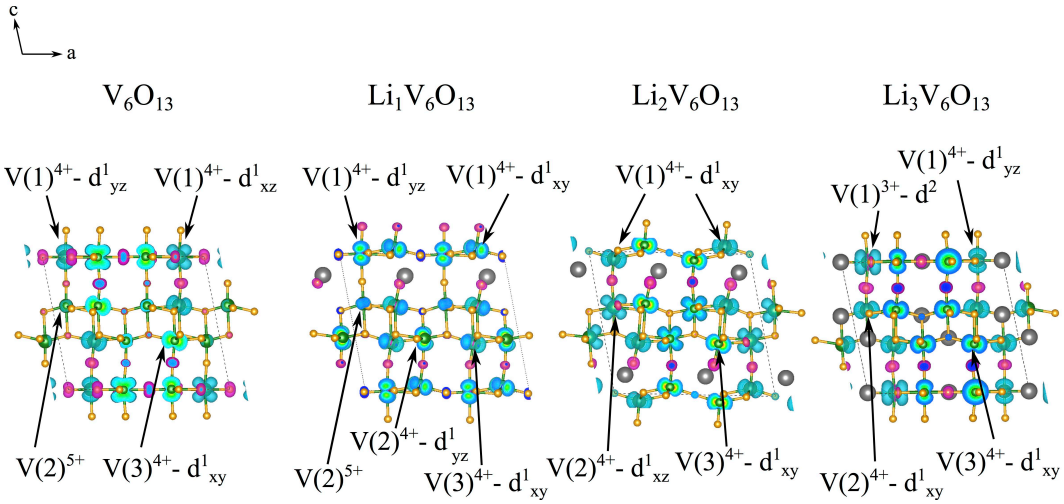

Figure 4.10. Isosurface of the unpaired electron distribution in V_6O_{13}, LiV_6O_{13}, $Li_2V_6O_{13}$ (phase 2), and $Li_3V_6O_{13}$ (phase 3) calculated with DFT. Vanadium, oxygen and lithium centres are shown with green, orange and grey spheres, respectively. In V_6O_{13}, the V^{5+} ions are located in the double layer and the unpaired *d* electrons occupy different t_{2g} orbitals in the V^{4+} atoms. All the V^{5+} sites are reduced to V^{4+} when two Li ions are inserted into V_6O_{13} and a redistribution of the occupancy of the t_{2g} orbitals occurs for all the vanadium atoms, indicating a substantial change in electronic structure. $Li_3V_6O_{13}$ has a similar charge distribution to that found in V_6O_{13}, except for the vanadium sites ($V(2)^{5+}$ to $V(2)^{4+}$, $V(1)^{4+}$ to $V(1)^{3+}$) that are reduced. Blue and magenta isosurfaces correspond to positive and negative unpaired spin density, respectively, and are plotted with an isosurface level of 0.008.

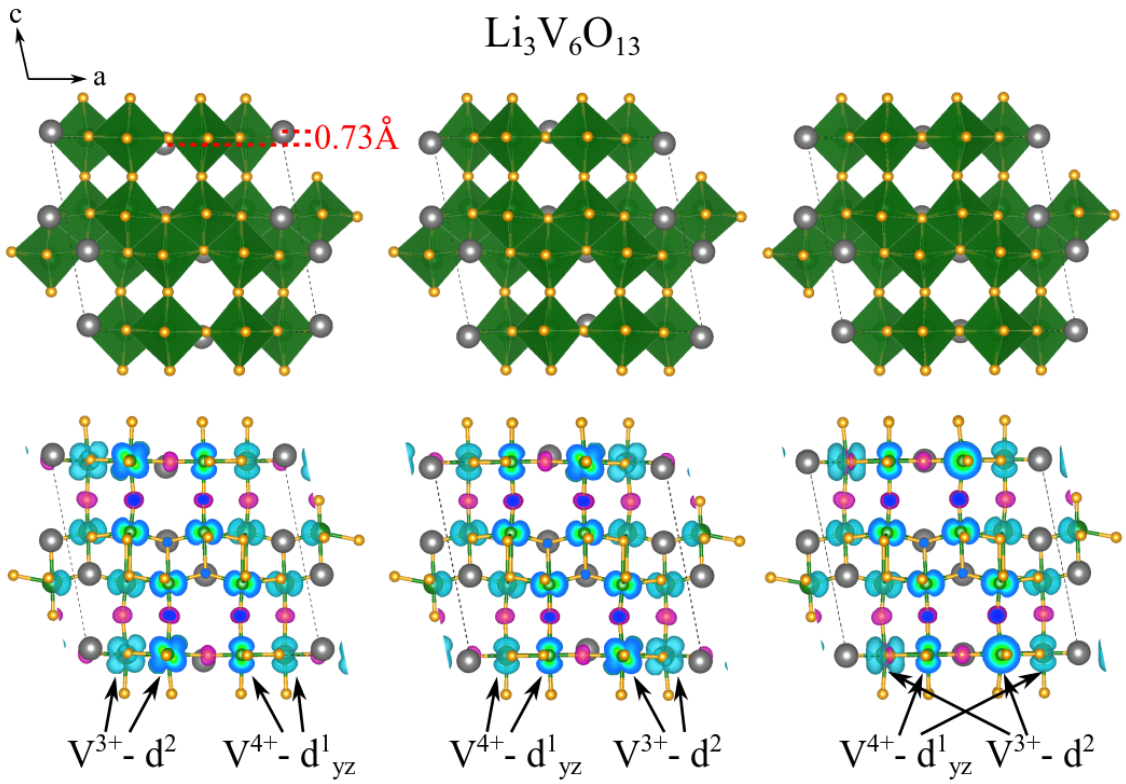

Figure 4.11. DFT derived structures of $Li_3V_6O_{13}$. Since the prior single crystal study found Li sites disordered 0.3 Å above and below the single layer,[5] $Li_3V_6O_{13}$ cells were generated for different Li(3) site positions within the refined distribution, and the structures were optimized with DFT (above). Structures generated with Li ions either all located on the single layer or all above or below all relaxed to a structure close to that shown on the far rig with the Li ions sitting on the plane. Structures with alternating Li ions above and below the plane resulted in stable geometries, as shown in the left and middle figures, with displacements above and below the plane of 0.365 Å(i.e., 0.73/2 Å) and noticeably different occupancies of the t_{2g} V^{3+} orbitals. The top structures show the Li positions (grey balls) and the resulting charge density maps are shown below, clearly illustrating that the orbital occupancy of the V(1) site in the single layer is sensitive to the Li(3) position

Comparing the single crystal $Li_{3.25}V_6O_{13}$[24] structure with that of $Li_3V_6O_{13}$[23], further lithiation results in partial occupancy of the Li(2) (in addition to the already fully occupied Li(3) and Li(4) positions) and a negligible change in volume. The lowest energy $Li_4V_6O_{13}$ configuration that retains full occupancy of Li(3) and Li(4) and partial occupancy of Li(2) indeed shows a 5% expansion along the *b* axis, and a more limited 1-2% expansion along *a* and *c*. This configuration is 21 meV higher in energy per atom from the structure on the hull, the energy difference that is close to the thermal energy at room temperature (k_BT = 26 meV).

4.3.4 Phase 4

The noticeable change in the *a*-parameter between phase 3 and phase 4 indicates that the Li ions redistribute again at this first order phase transition. Based on the analysis of the lowest

energy structures up to $Li_7V_6O_{13}$, following the labelling scheme in Figure 2.4, the Li(6) site is most likely to be occupied for the first time in phase 4 ($5.6 \leq x \leq 6.7$).

The lattice parameters extracted from *in situ* XRD indicate that, upon lithiation to phase 4, while the *b* and *c* lattice parameters remain similar to the values of phase 3, *a* expands up to almost 4%. From our DFT analysis, the majority of the lowest energy structures of $Li_6V_6O_{13}$ show half occupancy of the Li(6) site, with the associated increase in the *a* lattice parameter. The only low energy configuration with zero Li(6) occupancy - and full occupancy of Li(2), Li(3) and Li(5) – shows a more limited expansion of *a* and instead a more prominent increase along *b*, a trend which is not seen from the *in situ* XRD results. Moreover, the lowest energy structures of $Li_7V_6O_{13}$ all have half or full occupancy of the Li(6) site, in the latter case showing an additional expansion of another 1-2% along *a*. This trend reflects the changes of the lattice parameters seen from *in situ* XRD, confirming the effect of Li(6) occupancy on the expansion along *a*.

4.4 Linking structural changes with Li ion positions via ^{7}Li NMR

A combination of *in situ* XRD and calculation is used to deduce a wealth of mechanistic information. However, direct information concerning Li is difficult to obtain using XRD methods due to the low scattering cross-section, and due to the disorder inherent to intercalation of a parent crystal structure. ^{7}Li NMR is thus a valuable complementary technique, as it provides direct information regarding the local chemical environment of Li. The ^{7}LI NMR is consistent with XRD and calculation with distinct resonances being observed for each of the phases: phase 1, 2, 3, and 4 (Figure 4.12). Phase 2, phase 3 and phase 4 all show characteristic features that correspond with our definition of various phases. However, the changes of the main resonances are more complicated in phase 1, which supports the subdivision into phase 1a and phase 1b. Because the ^{7}Li NMR experiments are done *ex situ*, they best represent the Li environments of specific compositions in their equilibrium states, which do not necessarily reflect the Li positions and dynamics during the discharge/charge process.

4.4.1 Phase 1

The most prominent peaks in phase 1 are the ones at 39 and -16 ppm. For $Li_xV_6O_{13}$ with x = 0.6, 0.8, and 1.2, the 39 ppm peak corresponds to more than half of the total intensity of each spectrum. The shift of the Li(1) site in LiV_6O_{13} was calculated with DFT to be in the range of 46 – 57 ppm (see Chapter 2, Section 2.4 for more details), which is very close to the

measured value. Hence, the peak at 39 ppm in the experimental NMR spectrum is assigned to Li(1). However, for *x* =0.3, 0.6, 0.8, 1.2, and 1.5, the peak at -16 ppm is also pronounced in each spectrum, taking up more than 20% of total intensity (up to 78% in $Li_{0.3}V_6O_{13}$). DFT calculations indicate that the Li(2) site gives a shift in a range of -23 to -35 ppm, and the Li(5) site between 4 to -17 ppm. Hence, the peak at -16 ppm is assigned to either of these Li sites between the single and the double VO_6 layers. The peak at -23 ppm, even though it looks pronounced, only accounts for less than 5% of the total intensity in most spectra as it is extremely sharp and possibly corresponds to a more mobile Li environment.

The LiV_6O_{13} spectrum is noticeably different to the other ones from *x* = 0.3 to 1.5. The only dominant peak for this composition has a shift of -3.9 ppm, which, based on the DFT calculations, is assigned to the Li(5) site, as previously discussed. This spectrum with one dominant peak corresponds well with the LiV_6O_{13} single crystal study, which shows Li ordering and superstructure formation with strictly one Li environment.[121]

In the previous section, XRD experiment as well as DFT calculation show that Li(1) is the only site that gets occupied during Li intercalation into phase 1, which somewhat contradicts the NMR findings of this section. However, the DFT analysis of the formation energies shown in Figure 4.8 is performed at 0 K (Chapter 2, Section 2.4), and it does not account for the kinetic effects due to higher experimental temperatures or to Li reorganisation during cycling. Moreover, the energy difference between various configurations of LiV_6O_{13} is within thermal energy at room temperature, and it is within DFT error. Also, a more careful investigation into the phase 1 region of *in situ* XRD shows a large broadening of the (003) peak (Figure 4.13). *Ex situ* XRD also shows broadening in various states apart from *x* = 0.3, when Li only starts to intercalate into the host structure and, *x* = 1, when Li ions order in the lattice. This peak broadening indicates that there may be various configurations coexisting at compositions between *x* = 0.3 and 1.5. Therefore, when snapshots are taken, i.e. *ex situ* compositions are made, and NMR spectra are acquired, more than one site may be observed.

To rationalise the process of Li intercalation in phase 1, Li ions insert into the Li defect sites between the VO_6 single and double layers. Li(1) is the site that is lowest in defect energy and gets mostly occupied. However, since the energy taken to occupy Li(2) and Li(5) sites are similar to that of Li(1), some Li ions also intercalate these sites during the discharge process, which is a non-equilibrium one at a temperature much higher than 0 K. At least two configurations coexist in phase 1 until the second order phase transformation.

4.4.2 Phase 2

In phase 2, the main resonance shifts from 39 ppm to about 14 ppm, which can be due to the change in electronic structure, possibly due to a reduced hyperfine shift effect. There are multiple features clearly visible in the spectrum (Figure 4.12), indicating the presence of multiple Li sites. This is not altogether unexpected given the more complicated framework and the multiple vanadium environments (square pyramidal and octahedral). Strain analysis has shown that phase 2 is a high strain phase (Figure 4.14) and the source of the strain could be from the coherent interfaces of even more coexisting configurations, which again are close enough in formation energy and are accessible at room temperature.

4.4.3 Phase 3

Phase 3 shows mainly two resonances at around 7 and -60 ppm. The site occupancy of Li environment that the 7 ppm peak corresponds to exceeds 100% for x = 3.3 and 3.8, which indicates that the 7 ppm peak may be resolved into two peaks. Referring to the predicted Li positions within this phase (Section 4.3.3), this 7 ppm shift may correspond to Li(3) and Li(4) sites which are within the single and double VO_6 layers in phase 3. The peak at -60 ppm can then be related to the Li(2) site that gets further paramagnetically shifted in phase 3 region. More calculation is underway to confirm this preliminary peak assignment in this phase.

4.4.4 Phase 4

In phase 4, the Li uptake determines that there have to be at least three Li sites, consistent with the NMR spectrum of this phase. The ^{7}Li NMR spectrum of phase 4 shows a much greater broadening of spectral features, which is likely due to either a through space dipolar interaction or through bond Fermi contact interactions that significantly decreases the relaxation of Li. Since the conductivity decreases with Li composition increasing, this is possibly related with more localised electrons. The spectrum also shows a third and much broader peak at higher positive shift (highliged in Figure 4.12). Previous single crystal XRD studies were unable to determine Li crystallographic sites in phase 4,[18] though the NMR spectra collected in this work suggests the presence of at least three crystallographic positions for Li insertion.

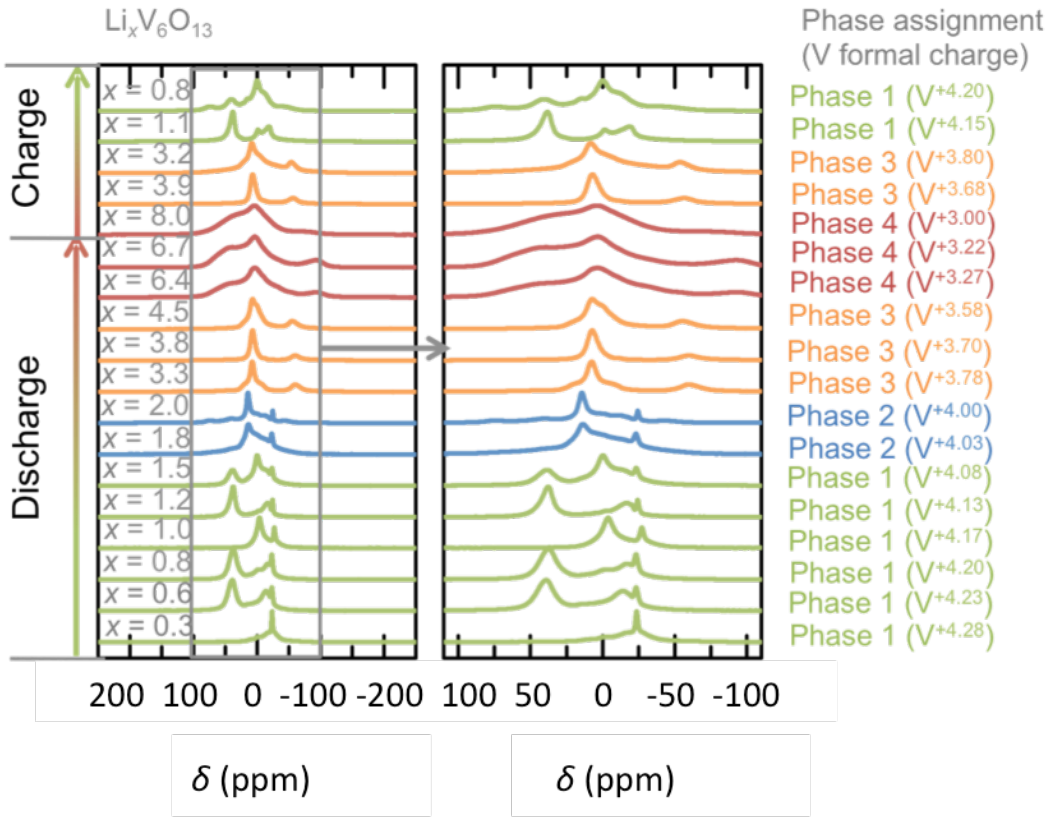

Figure 4.12. ^{7}Li *ex situ* MAS NMR spectra (RT, B_0 = 4.7 T, MAS spinning speed 60 kHz) of $Li_xV_6O_{13}$ with room temperature electrochemically lithiated compositions on the first discharge up to x = 6.7 (x = 8.0 composition was lithiated at 75°C)., and *x* = 3.9, 3.2, 1.1, and 0.8 on the first charge process. The rig figure shows a zoom of the -110 to 110 ppm frequency range. The vanadium formal charges are calculated based on the nominal Li composition.

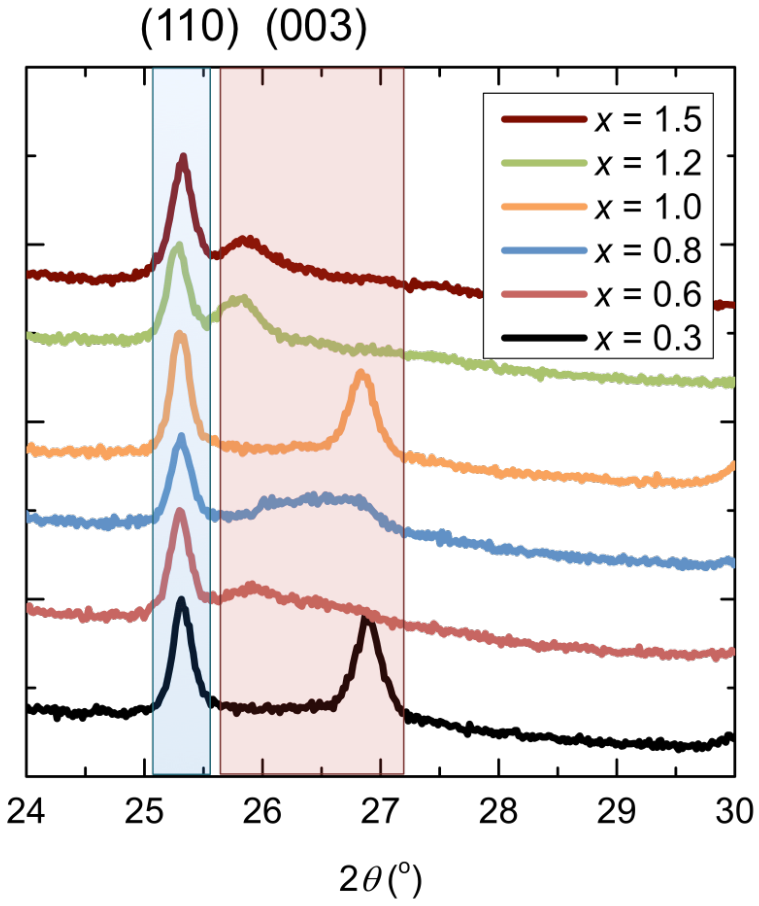

Figure 4.13. *Ex situ* XRD of $Li_xV_6O_{13}$ (x = 0.3, 0.6, 0.8, 1.0, 1.2 and 1.5) collected in the phase 1 region of first discharge. The (110) and (003) reflections are shaded in blue and red respectively. Only a 2θ region from 23 to 29 ° is shown for clarity. The (003) peaks in $Li_{0.6}V_6O_{13}$, $Li_{0.8}V_6O_{13}$, LiV_6O_{13}, $Li_{1.2}V_6O_{13}$, and $Li_{1.5}V_6O_{13}$ all show broadening to a different extent, which indicates coexistence of various configurations in that phase.

4.5 Asymmetry of discharge and charge

The mechanism of phase transformation determined by *in situ* XRD is summarised in Figure 4.15, with the nominal compositions calculated from the first discharge and charge cycle of the *in situ* battery. The asymmetry of discharge and charge is highliged by the omission of phase 2 upon charge. It is interesting to note the $Li_xV_6O_{13}$ system is unable to nucleate a phase with such a large change in *c* (+6.8%) and *b* (-6.1%) parameter within phase 3 upon charge, the formation of a phase with such a large discontinuous volume change clearly being too energetically unfavourable. Instead, Li is continuously extracted until phase 1 is nucleated (with a smaller (but not insignificant) +4.2% and -5.3% change in *c* and *b* parameters).

The asymmetry can be explained by the theory of coherent interface in homogeneous nucleation. In a solid-solid transformation, the strain energy effect must be included with

the volume free energy and interfacial energy changes to count the free energy change. The formation of a coherent interface raises the free energy of the system accounting the elastic strain fields that arise. In other words, a larger change of the dimensions of two-phases implies a larger energy barrier to overcome in order to nucleate one phase out of another. Therefore, the strain accumulates in phase 2 to gain enough free energy to initiate a first order phase transformation with large changes in two dimensions during discharge (Figure 4.14). As a proxy, the average strain is used, which in phase 2 is 0.25 ppm, being 3.5, 1.5, and 1.2 times of the averages of that in phase 1, phase 3, and phase 4, respectively. Upon charging, the system does not have enough energy at $Li_3V_6O_{13}$ to nucleate $Li_2V_6O_{13}$ because the energy barrier caused by the large change of dimensions is too large to overcome. Therefore, Li continues to be extracted from phase 3 until it reaches the composition $Li_{2.3}V_6O_{13}$, where cell parameter change is such that the energy barrier caused by the coherent interface has decreased to a point where first order phase transformation is likely.

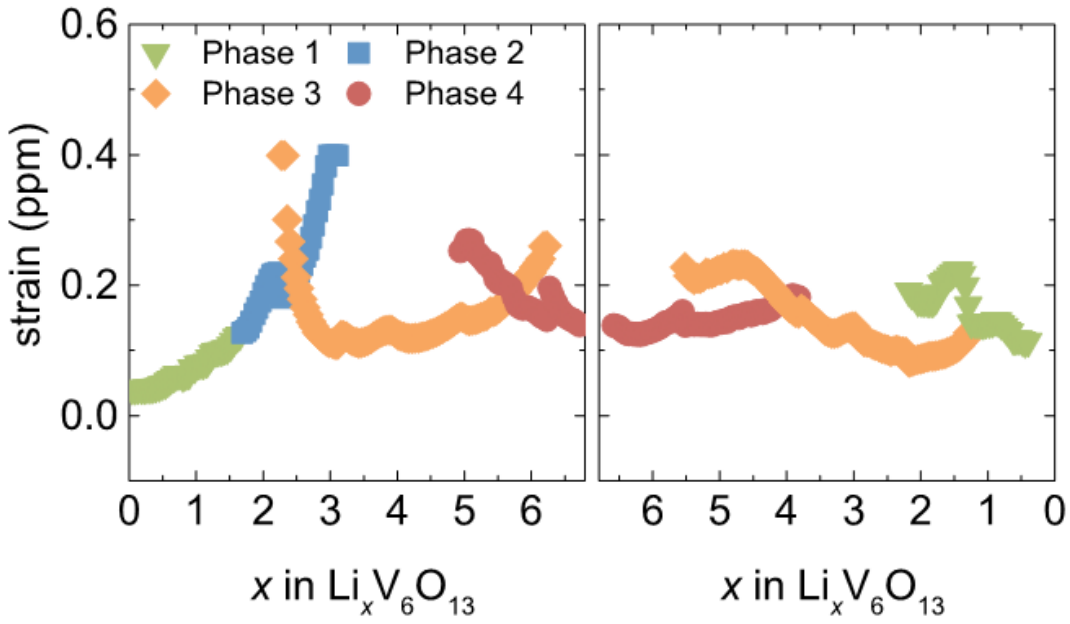

Figure 4.14. Evolution of strain in various single-phases of $Li_xV_6O_{13}$ upon discharge (left) and charge (rig). First order phases transitions are accompanied by an abrupt change in strain, while second order phase transitions (green to blue) have smooth (and continuous) change in strain.

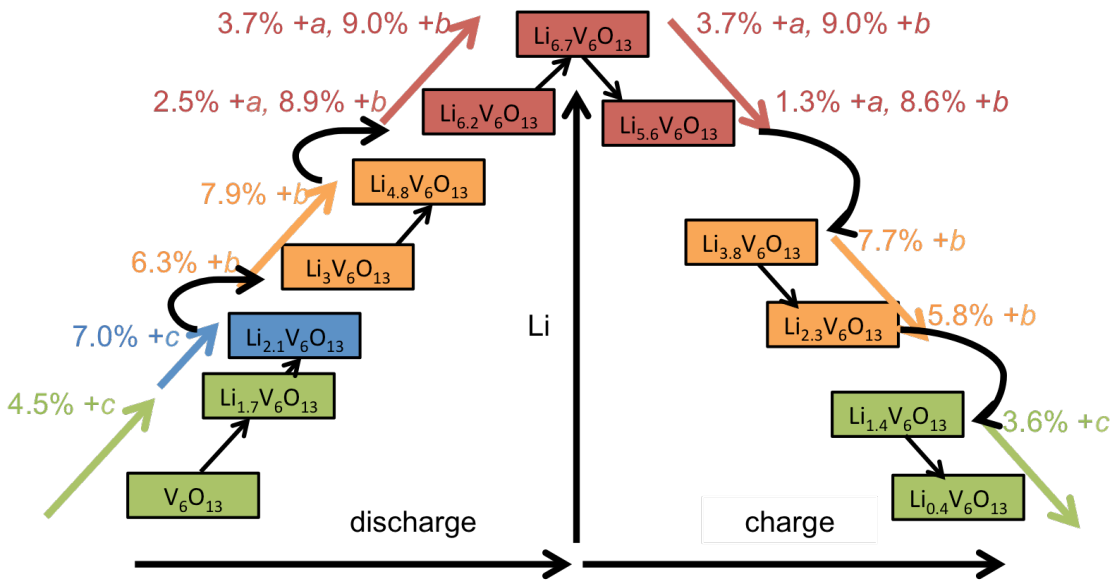

Figure 4.15. The proposed mechanism of the first discharge and charge process of V_6O_{13} determined by *in situ* XRD. The most significant change in lattice parameters of phase 1 (green), phase 2 (blue), phase 3 (orange) and phase 4 (red) are shown in arrows above corresponding phases, where the %s correspond to changes within the phase and between phases. Solid solutions are represented by arrows pointing from the starting phases to the end phases, while miscibility gaps are shown by blanks between two-phases.

From an atomic level, upon lithiation, the lowest energy location in the crystal structure to accommodate Li ion is in the Li(1) interstitial voids between the VO_x single and double layers (Figure 13). Without further structural data, the driving force for the second-order transition between phase 1 and phase 2 is not clear, but on the basis of the crystal structure it appears to be related to the formation of five-coordinated vanadium ions. DFT results suggest that it is also electronic in nature and involves occupancy of the d_{xz} and d_{yx} orbitals at the V(1) sites in phase 1 and 2, respectively, although this phenomenon is likely coupled to the distortion that leads to five-coordinated V(1) sites. Lithiation continues until the Li(1) sites are fully occupied and *c* is stretched by 7% in total compared to V_6O_{13}. At which point the system accumulates enough strain on a particle level to push through a first order phase transition to phase 3, where the Li ions are now located *within* the VO_x layers. This is accompanied by a large change in cell parameters, as the *c* parameter shrinks because the structure is no longer supported by Li ions in interstitial sites *between* the layers, and the *ab* plane is expanded by placing Li ions *within* the layers.

4.6 Conclusion

In conclusion, the first discharge and charge process of cathode LIB material V_6O_{13} is studied using electrochemistry, *in situ* XRD, DFT calculations and NMR. An alternating solid solution

and two-phase mechanism has been proposed. The material features an asymmetric six-step discharge and five-step charge, and expands/shrinks in a sequential order along *a*, *b* and *c* axes. This sequential change, accompanied by significant electronic rearrangements, is related to changes in the occupancy of Li ions in different Li sites in the unit cell and charge ordering. The asymmetry comes from phase 2, which has a more distorted V—O framework compared with phase 1 and phase 3. It is formed through a second order phase transition on lithiation during discharge, but is not reformed on delithiation during charge, which is due to the energy barrier generated by the coherent interface between the two-phases. Apart from this asymmetric electrochemistry, the ranges of the single-phase regions as well as miscibility gap regions are similar upon charge and discharge, and the overall discharge and charge are reversible.

Via a combined analysis of the *in situ* XRD data and the DFT-calculated cell parameters of a variety of different structures constructed with different Li occupancies and arrangements, possible sites for Li beyond the composition $Li_{3.25}V_6O_{13}$ are proposed, where no prior single crystal XRD data exists. NMR spectra show possible coexistence of various configurations within phase 1 and phase 2, suggesting that the structures with sligly higher formation energies are also present at room temperature and various sites can get occupied in different composites in phase 1 and phase 2. In this shear structure of V_6O_{13}, every V_6O_{13} unit contains two perovskite type cavities and each cavity is able to host more than three Li atoms The space group of the structure and main V—O framework remain unchanged although the material evolves through various phases caused by Li insertion and rearrangement. This may be the reason behind the extraordinarily high capacity of this material.

5 High temperature (de)lithiation mechanism of V_6O_{13}

Because both applications in Li polymer and all solid-state batteries require battery operation at elevated temperatures, further knowledge on the phase transformation mechanisms of V_6O_{13} during discharging and charging is critical. *In situ* synchrotron XRD was carried out to probe the phase transformations from 25°C to 125°C. Two temperatures, 25°C (RT) and 100°C, are showcased at the start of this chapter to highlig the change between RT and . The phase compositions and lattice parameters are extracted from the set of *in situ* synchrotron XRD experiments from 25°C to 125°C. The comparison of these data at VT reveals the major changes of lithiation mechanisms of V_6O_{13} at . DFT calculations were used to complement the XRD techniques, and give more insights into the structural changes in the material during (dis)charge. Roberta Pigliapochi is greatly acknowledged for doing the DFT calculation that is shown in Section 5.4.

5.1 Cycling V_6O_{13} at different temperatures

The organic electrolyte used for RT cycling (LP30) cannot be used at HT due to its volatility and reactivity that causes gaseous phase formation and pressure accumulation inside the cell.[28] An IL electrolyte (0.5 mol/kg LiTFSI in [C_3mpyr][TFSI]) is therefore used at temperatures above 75°C due to its negligible volatility, good chemical and thermal stability.[37] A more detailed description of these two types of electrolytes can be found in Chapter 2, Section 2.1.2. A set of VT experiments is performed on the first cycle of V_6O_{13} (Table 5.1), with a temperature step of 25°C from 25°C to 125°C. Both organic and IL electrolytes are tested at 75°C to investigate the influence of electrolyte on the cycling performance.

The first cycle voltage profile is found to be different at HT. For instance, comparison of first cycles of V_6O_{13} against Li at 25°C and 100°C, performed at a rate corresponding to C/10 (assuming a theoretical capacity of 417 mAh/g), show a more sloping discharge profile and extra capacity at HT (Figure 5.1). At 100°C, the 2.47 V plateau is shortened compared to that at 25°C; a plateau at 1.75 V, which is not present at 25°C, adds 12% more discharge capacity to the 375 mAh/g specific capacity of V_6O_{13} achieved at RT. On charge, the overall stepwise electrochemistry does not change significantly at 100°C, apart from the plateau at 1.8 V, which represents the reversible oxidative process to the new reductive process

corresponding to the 1.75 V plateau on discharge. The electrochemistry data suggest that (1) there might be a change in the Li intercalation mechanism on discharge between $Li_{1.6}V_6O_{13}$ and $Li_{2.4}V_6O_{13}$, (2) more Li can reversibly intercalate into the $Li_xV_6O_{13}$ host material at elevated temperatures.

Table 5.1. List of experiments performed on V_6O_{13} from 25 to 125°C. The rate of cycling is represented in C-rate forms. GCPL on the first discharge of batteries with the organic electrolyte (LP30) are tested at 25, 50, and 75°C. GCPL on first discharge of batteries with IL electrolyte (0.5 mol/kg LiTFSI in [C3mpyr][TFSI] are tested from 75 to 125°C.

Temperature (°C)	Organic electrolyte	IL electrolyte
25	C/10	No experiments
50	C/10 (part)	No experiments
75	C/10	C/10
100	No experiments	C/10
125	No experiments	C/10

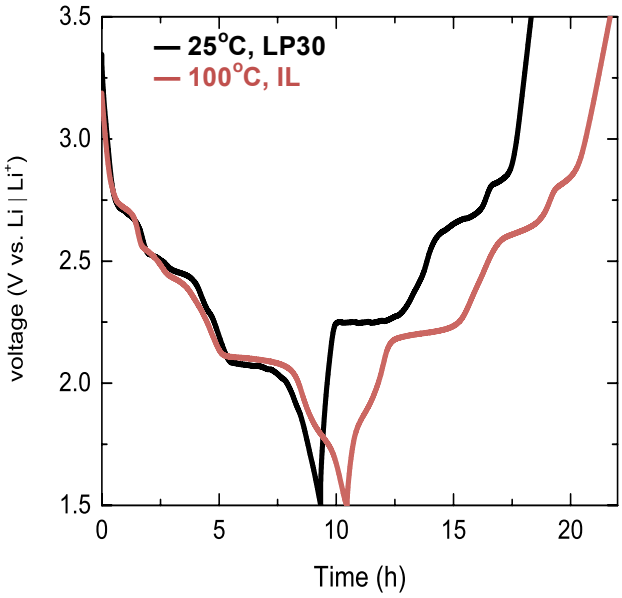

Figure 5.1. Comparison of first discharge and charge voltage profile of V_6O_{13} at RT (black) and 100 °C (red). Both batteries are cycled in Swagelok cells at a rate of C/10. The discharge profile show smearing of the step-wise electrochemistry and extended regions on discharge at 100°C. The discharge capacity reaches 420 mAh/g at 100°C, 12% more capacity than that observed at RT.

5.2 *In situ* XRD results

5.2.1 High temperature *in situ* XRD

The complex evolution of $Li_xV_6O_{13}$ crystalline phases is suited to *in situ* XRD, which allows us to track phases and their evolution with satisfied resolution. VT *In situ* XRD experiments are performed at a rate of C/10 from 25°C to 125°C. The patterns collected at 100°C are shown in comparison with those at 25°C (Figures 5.2 and 5.3) to present the phases available at HT. There are regions of single phases as well as two-phase as highlighted in Figure 5.2, which suggests that the alternating single-phase interstitial solid solution and two-phase nucleation/growth mechanisms still take place at HT.

First discharge at 100°C

The lattice parameters extracted from *in situ* XRD data using Pawley refinement confirm the formation of phase 1, phase 3 and phase 4 at 100°C (Figures 5.3 and 5.4), using the phase naming convention from the RT study presented in Chapter 4. The Li composition is determined by assuming all current measured during discharge and charge corresponds to intercalation and extraction of Li into the material. At 100°C, single-phase regions are at

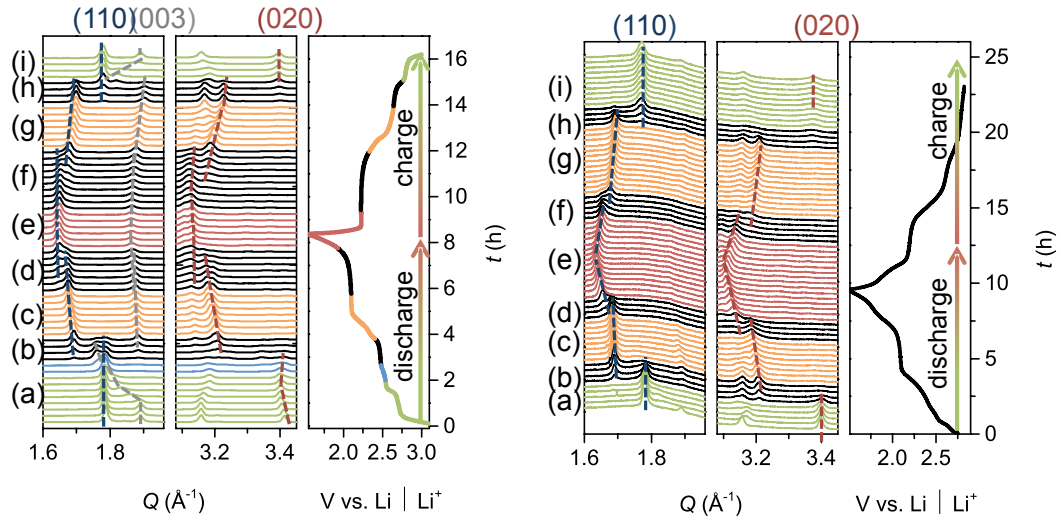

Figure 5.2. *In situ* synchrotron XRD of the first discharge and charge cycle of V_6O_{13} cycled at 25°C (left) and 100°C (right). Colored lines correspond to single-phase regions and black lines correspond to two-phase regions. The different states of discharge and charge are denoted as (a) – (i). The (110), (003) and (020) reflections can be tracked to monitor the structural changes during electrochemical cycling. Continuous shifts in peak positions are characteristic of single-phase solid solutions (a, c, e, g, i), while the growth and disappearance of peaks are characteristic of two-phase nucleation and growth (b, d, f, h). The asymmetry in the discharge and charge profiles at 25°C is demonstrated by the fact that (003) reflection crosses (110) on discharge but does not cross on charge, but not observed at 100°C. The discharge of the 100°C cell starts from 2.8 V due to self-discharge of the battery that occurs during the long shelf time from assembly and transportation to the beamline.

phase 1a ($0 \le x < 0.4$), phase 1b ($0.4 \le x < 1.1$), phase 3 ($3.0 \le x \le 4.6$), and phase 4 ($5.6 \le x \le 8.0$), and the two miscibility gaps are at $1.1 < x < 3.0$ between phases 1 and 3 and $4.6 < x < 5.6$ between phases 3 and 4, respectively. No evidence of phase 2 was found during discharge at 100°C, which is strikingly different from RT,

During the discharging process, as much as 8 Li ions can be inserted into one unit formula V_6O_{13} at 100°C, which results in cell volume expansion of 15.3% (Figure 5.4). At 25°C, the overall unit cell volume expansion is 14.8%, which corresponds to a total of 6.7 Li ions inserting into one unit formula V_6O_{13}. As Li is intercalated into phase 1, the cell volume changes in a similar way to that seen at RT, staying unchanged for $0 \le x < 0.4$ (phase 1a) but increasing significantly by 2.5% for $0.4 \le x < 1.1$ (phase 1b). The voltage drop from 2.7 to 2.5 is in line with the subdivision of phase 1a and phase 1b, taking place around 0.4. Phase 1b mainly changes along *c*, expanding by 3.1% at 100°C, 1.4% smaller than that at 25°C, resulting in the overall volume expansion of phase 1b at 100°C being 1.4% smaller compared with 25°C (Figure 5.3).

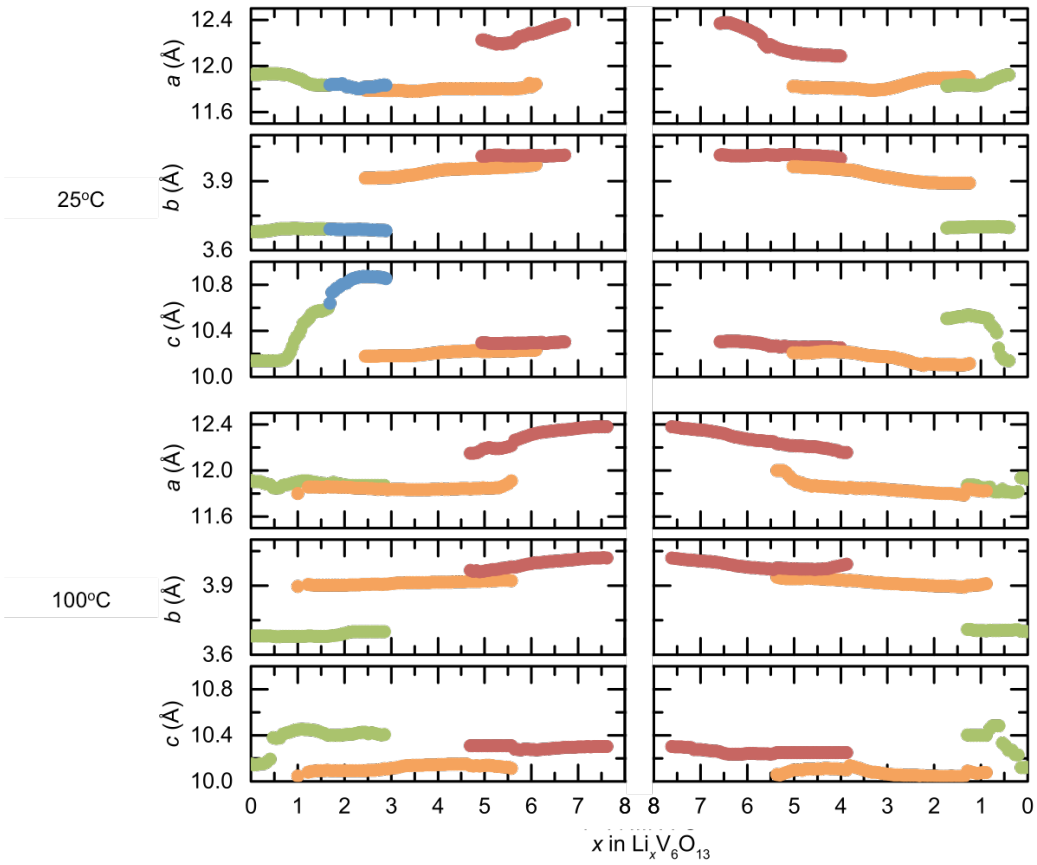

Figure 5.3. Evolution of lattice parameters of the four phases observed during the first cycle at 25°C (up) and 100°C (down). The unit cell parameters change in a sequential order, with *c*, *b*, and *a* expanding one by one during discharge and shrinking back during charge. While one unit cell parameter increases dramatically, the others remain relatively unchanged. No evidence of phase 2 is observed at 100°C.

Unlike at 25°C, *in situ* XRD measurements at 100°C reveal that phase 3 directly nucleates within phase 1b. The lattice parameters of phase 3 at 100°C are similar to those at 25°C (Figure 5.3). For instance, $Li_3V_6O_{13}$, the incipient composition of phase 3 in the single-phase region, has a unit cell parameter of a = 11.789 Å, b = 3.913 Å, and c = 10.179 Å at 25°C, and a = 11.834 Å, b = 3.906 Å, and c = 10.106 Å at 100°C, the largest difference being only 0.7% along c. Phase 3 nucleates from phase 1b at 100°C, where the microstrain (see Chapter 2 for more details) is only half of that at the nucleation point at 25°C, indicating that HT aids the first-order phase transition (Figure 5.4). When Li is inserted at 100°C until the end of solid solution phase 3 region ($Li_{4.6}V_6O_{13}$), the lattice parameter changes in all directions are less than 0.5%. The uniaxial expansion along b at RT is not observed at 100°C.

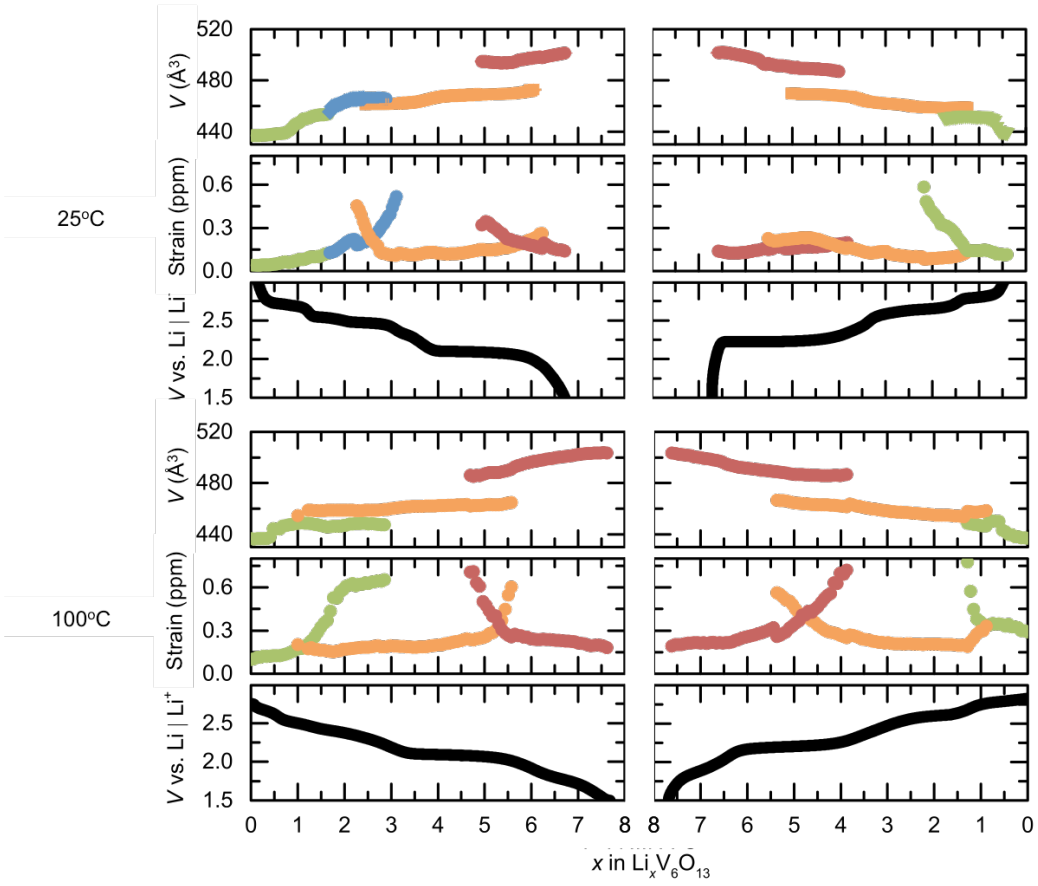

Figure 5.4. Evolution of unit cell volumes and microstrain (determined from the Pawley refinement, as detailed in Chapter 2) of the four observed phases during the first discharge (left) and charge (right) cycle of V_6O_{13} at RT (top) and 100°C (bottom). The unit cell volume progressively increases upon discharge as Li is incorporated, and decreases upon charge. The continuous change in unit cell volume from phase 1 (green) to phase 2 (blue) on discharge at RT is characteristic of a second order phase transition. Phase 2 is not observed on either charge at RT or during the whole discharge and charge at 100°C. The orange points correspond to phase 3 and red to phase 4. The discontinuous change in volume and growth of new phases is characteristic of a nucleation and growth mechanism, which operates in all other transformations.

At both temperatures, phase 4 nucleates from phase 3. The miscibility gap between phase 3 and phase 4 is smaller at 100°C ($4.6 \leq x < 5.6$) compared to RT ($4.8 \leq x < 6.2$). This two-phase region at 100°C also corresponds to the 2.1 V plateau on the voltage profile. At 25°C, phase 4 expands uniaxially along *a* by 1.2% for $6.2 \leq x < 6.7$ (Figure 5.3). At 100°C, phase 4 expands in both *a* (1%) and *b* (1.1%) directions for $5.6 \leq x < 8.0$. The 2D expansion comes with 1.3 more Li uptake per formula unit, as well as the extra plateau at 1.8 V on discharge.

First discharge from 25°C to 125°C

In situ XRD measurements at 100°C show that the main differences in phases formed during RT and HT cycling lie in phase 2 and phase 4. The series of *in situ* XRD from 25°C to 125°C further indicate that

(1) phase 2 only disappears above 100°C (Figure 5.5). Extracted phase information at VT shows that phase 2 is formed at 25°C, 50°C, and 75°C. Notably, once phase 2 is formed, there is little evidence that the Li solubility range of phase 2 is temperature dependent. The first miscibility gap between phase 2 and phase 3 falls in the range of $1.8 \leq x < 3.0$. When temperature rises to 100°C and above, phase 2 disappears and the miscibility gap (now between phase 1b and phase 3) widens to $1.2 \leq x < 3.0$, almost 50% wider compared to that below 100°C.

(2) the much expanded lattice parameter *c* in phase 2 shrinks with temperature below 100°C (Figure 5.6). Unlike the solubility range of phase 2, the lattice parameters of phase 2 are temperature dependent (Figure 5.6). Lattice parameter *c* is chosen over *a* and *b* to represent the change in phase 1 and phase 2 because it is much more significant. The starting composition of phase 2 (end composition of phase 1b) has a *c* lattice parameter of 10.597 Å, 10.534 Å, and 10.506 Å at 25°C, 50°C, and 75°C respectively. Even though the end phase composition of phase 2 is similar at 25°C, 50°C, and 75°C, the *c* lattice parameter decreases from 10.853 Å (25°C) to 10.773 Å (50°C) to 10.615 Å (75°C). Therefore, the unit cell expansion in *c* decreases with temperature increase, reducing from 2.4% increase at 25°C, to 2.2% at 50°C, to 1.0% at 75°C, in the phase 2 region.

(3) phase 4 solid solution region extends at HT. At 75°C, the solid solution phase 4 is present at $5.4 \leq x < 7.9$, increasing by 400% compared to the phase 4 region at $6.2 \leq x < 6.7$ at RT (Figure 5.5). As temperature further rises, the wide solubility range of phase 4 remains.

(4) lattice parameters in phase 4 expand more isotropically at HT. When temperature reaches 75°C and 100°C, the unit cell expands in both *a* and *b* (Figure 5.6), instead of increasing uniaxially along *a* (see RT). At 125°C, the unit cell expands in all three

directions. The *a* and *b* lattice parameters of the incipient phase 4 at 125°C are smaller than those at 25°C, differing at much as 1% and 1.3%, respectively.

(5) other phases also show minor changes in the composition range and lattice parameters. The Li composition range of phase 1a shrinks from $0 \le x < 0.7$ at 25°C to $0 \le x < 0.4$ at 125°C. After the second order phase transition to phase 1b, about one Li can intercalate into phase 1b regardless of the temperature increase. The *c* lattice parameter of phase 1b shows continuing decrease with the rise of temperature up to 100°C.

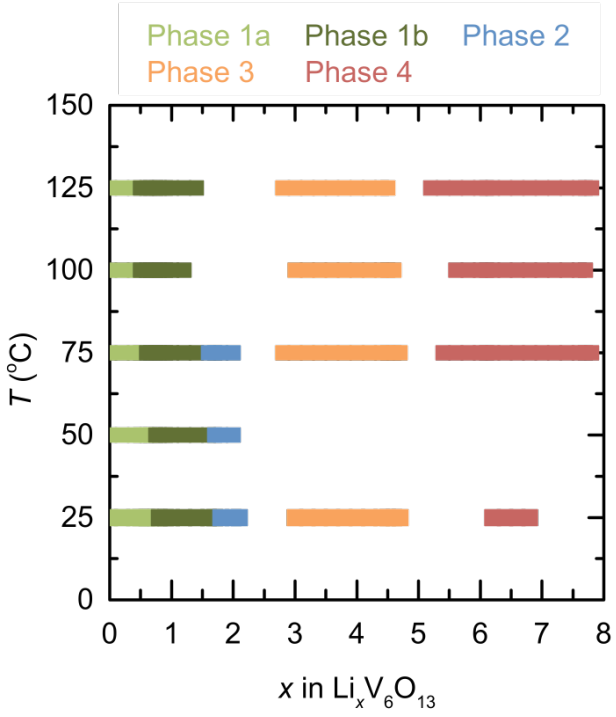

Figure 5.5. Bar diagram of the first discharge process of V_6O_{13} determined by *in situ* XRD. Phase 1a, phase 1b, phase 2, phase 3 and phase 4 single phase compositions that are formed during first discharge at VT are shown in green, dark green, blue, orange, and red dots, respectively. Data are extracted from the first full discharge process of V_6O_{13} from 25 to 125$_o$C, apart from 50°C. The beam was lost at during the latter half of the experiment and phase information was not collected.

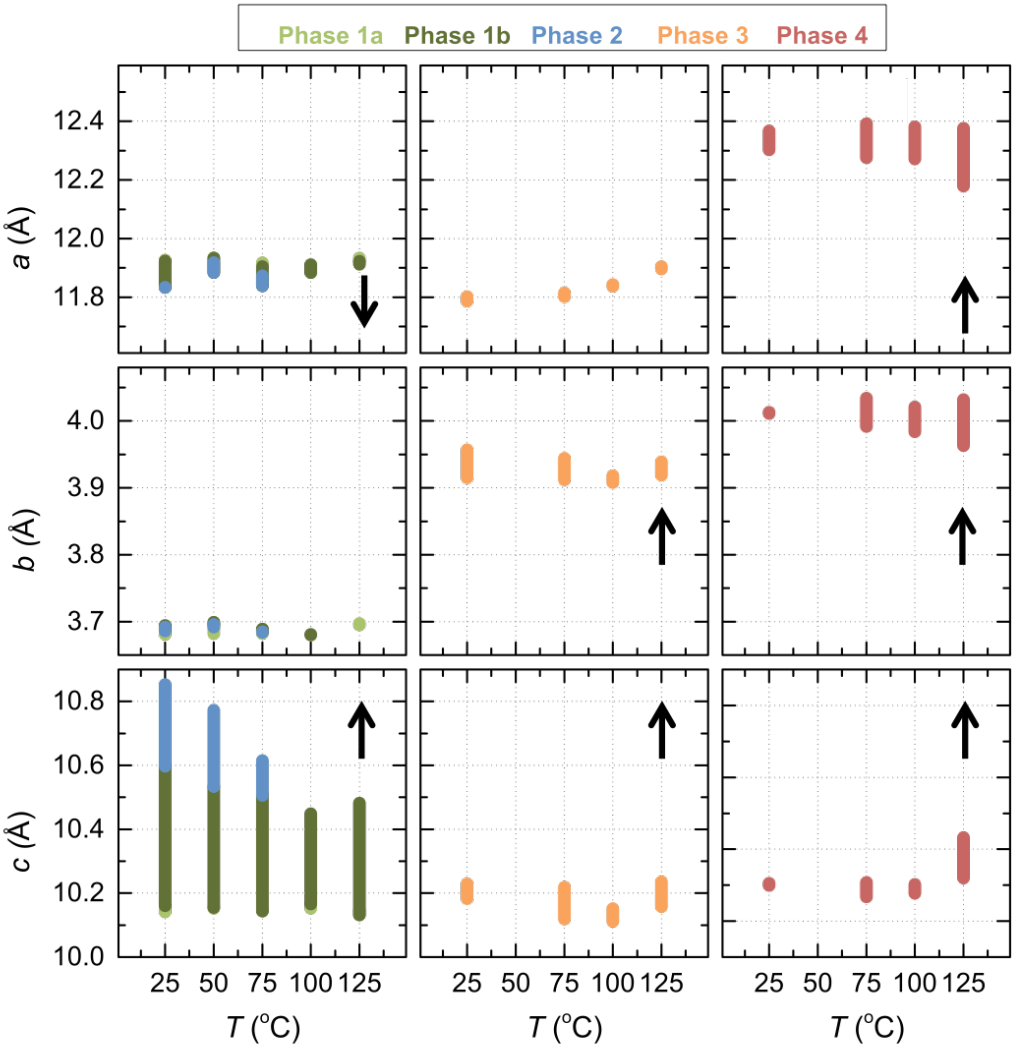

Figure 5.6. The ranges of lattice parameters of phase 1a (green), phase 1b (dark green), phase 2 (blue), phase 3 (orange), and phase 4 (red), extracted form VT *in situ* XRD experiments performed at temperatures from 25°C to 125°C. The black arrows represent whether lattice parameters increase or decrease in that phase. The lattice parameters at 50°C could not be extracted due to the loss of the beam during part of the experiment. The most significant changes of lattice parameters are the disappearance of phase 2 and expansion in phase 4 at HT.

First charge at 100°C

Li is deintercalated from $Li_8V_6O_{13}$ and V_6O_{13} is formed at the end of charge. During charging, the material evolves through five steps, which include three single-phase solid solutions (Figure 5.3), namely phase 4 ($5.5 < x \leq 8.0$), phase 3 ($1.4 < x \leq 3.8$), and phase 1 ($0 < x \leq 0.9$) and two miscibility gaps ($0.9 < x \leq 1.4$, $3.8 < x \leq 5.5$). Similar to the charging process at 25°C, both transitions from phase 4 to phase 3 and phase 3 to phase 1 are first-order. Phase 2 is also not observed on charge, which makes the discharge and charge process at 100°C seemingly symmetric. Phase 4 extends over a wider Li composition range on both discharge

and charge at 100°C compared to 25°C. The plateaus at 1.75 V on discharge and 1.8 V on charge reflect this reversible prolonged Li insertion and extraction process at HT. Therefore, understanding the mechanism behind the disappearance of phase 2 and extended Li (de)intercalation in phase 4 is critical for understanding the performance of V_6O_{13} as a cathode material at HT.

V_6O_{13} is found to be undertaking a slightly different lithiation process to phase 4 at 100°C compared to RT during discharge, bypassing phase 2, while phase 4 is delithiated to phase 1 via similar phase transition processes at both 25°C and 100°C. Phase 4 has increased solubility of Li and is found to expand in at least two directions, resulting in the extra capacity observed at 100°C. Whether these two major differences take place at a certain onset temperature or gradually as material characteristics change with temperature remain a subject of study.

5.2.2 Comparison of organic and ionic liquid electrolytes at 75°C

As mentioned in section 5.1, *in situ* XRD experiments are performed during first discharge of V_6O_{13} cells with both organic and IL electrolytes at 75°C. In both electrolytes, the first discharge cycles insert 8 Li ions per formula unit from V_6O_{13} to $Li_8V_6O_{13}$, corresponding to 417 mAh/g discharge capacity (Figure 5.7). The identity of the electrolyte does not influence the general evolution of the crystal structure, as determined by *in situ* XRD. The voltage profiles show little difference as well, as the 2.7 V, 2.45 V, 2.4 V, and 2.1 V plateaus all appear within the same Li composition region.

However, the ranges of the miscibility gap regions differ with the choice of electrolyte at 75°C. $Li_xV_6O_{13}$ has larger miscibility gaps when using IL electrolyte compared to organic ones. The regions for first order phase transformations between phase 1 and phase 3, phase 3 and phase 4, are at $2.0 \leq x < 2.7$, and $4.7 \leq x < 5.4$ respectively in organic electrolyte cells; while the regions widens to $1.8 \leq x < 2.9$, and $4.6 \leq x < 6.1$ in IL cells.

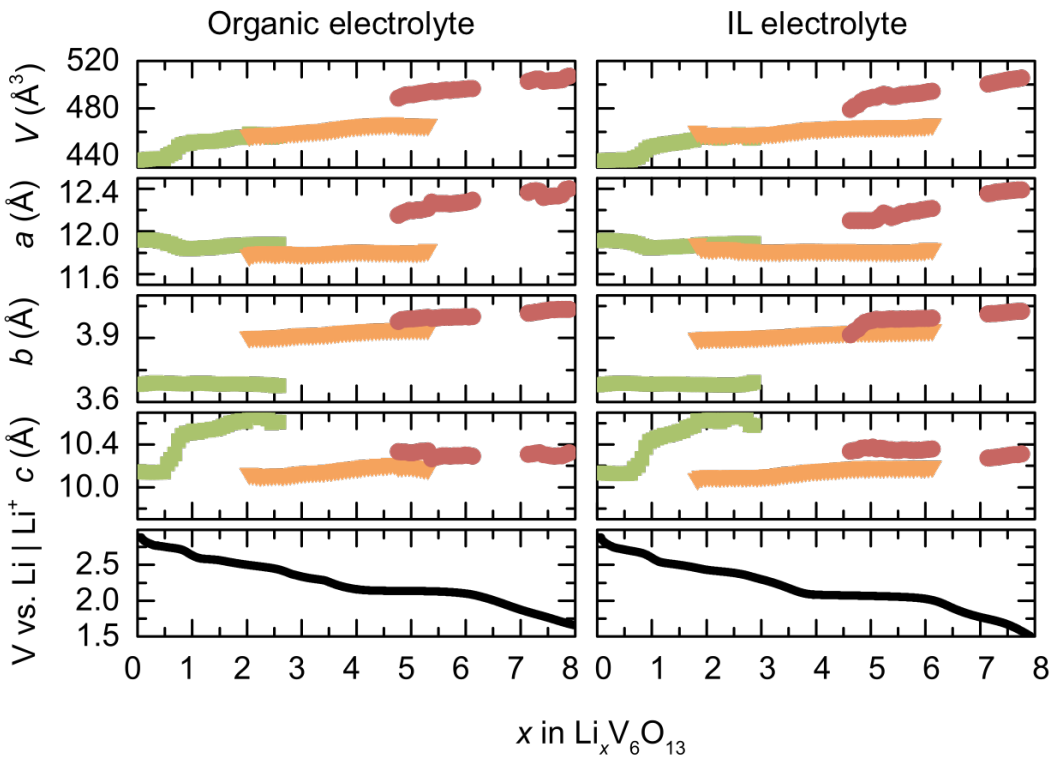

Figure 5.7. Evolution of unit cell volume and lattice parameters of the three phases observed during the first discharge of V_6O_{13} in a cell with organic electrolyte (left) and ionic liquid electrolyte (right) at 75°C. The major difference between $Li_xV_6O_{13}$ phase transition mechanisms within cells with these two types of electrolytes is the range of miscibility gaps. The material in the IL electrolyte tends to have wider miscibility gaps.

5.3 *Ex situ* XRD and NMR results

A series of VT *ex situ* XRD on $Li_2V_6O_{13}$ (phase 2) was performed to determine whether phase 2 is a thermodynamically stable phase. The *ex situ* XRD patterns show no changes in composition, no phase formation or decomposition, only with peaks shifting continuously due to positive or negative thermal expansion. The (001) reflection of $Li_2V_6O_{13}$ shift to higher 2θ from 25°C to 100°C (Figure 5.8), indicating the *c* lattice parameter shrinks with increasing temperature, which corresponds with the *c* shrinkage of the same composition observed at the same composition range during *in situ* XRD. When temperature further increases, *c* starts to expand again as the (001) peak shifts to lower 2θ. The (110) reflection, which is determined by both *a* and *b* lattice parameters, shows a minor change in peak positions as well as peak shape, indicating that the *a* and *b* lattice parameters change very little when the sample is heated from 25°C to 150°C. The XRD pattern at 125°C is almost identical to that at 25°C.

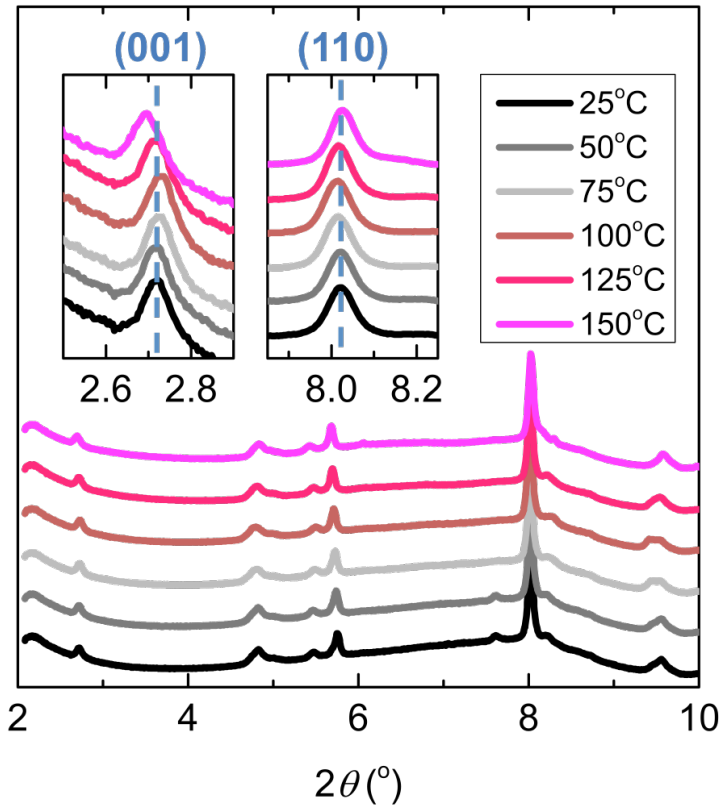

Figure 5.8. *Ex situ* VT XRD on $Li_2V_6O_{13}$ (phase2) from 25 to 150°C. Regions of (001) and (110) reflections are zoomed in and shown in embedded graphs. The *c* lattice parameter, which is indicated by the (001) peak, has the most significant change due to temperature in phase 2, while *a* and *b* lattice parameters show minor changes, indicated by the (110) peak. The (001) peak shifts continuously to higher 2θ from 25 to 100°C and back to lower 2θ above 100°C.

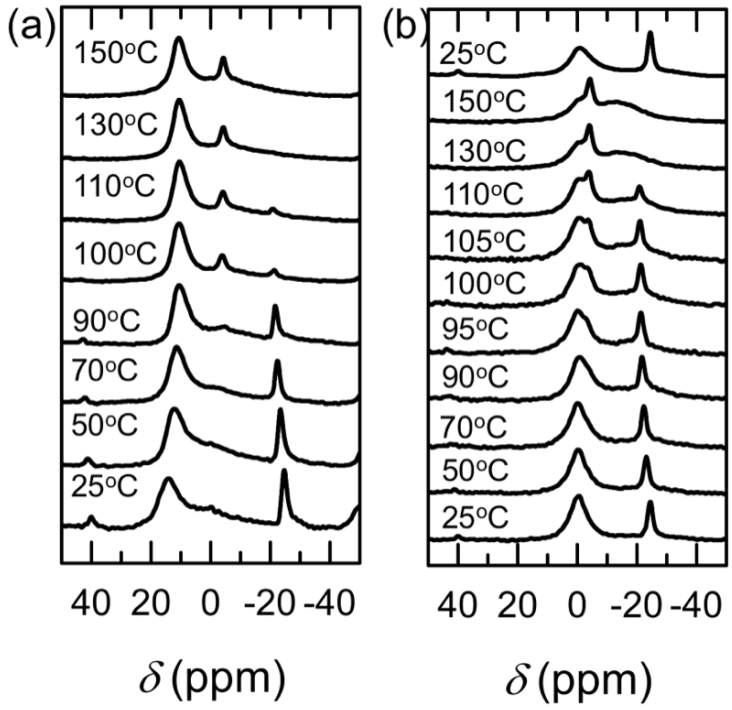

Figure 5.9. *Ex situ* VT NMR spectra of (a) $Li_2V_6O_{13}$ from 25 to 150°C. A new Li resonance at -4 ppm becomes present once the temperature rises above 90°C, meanwhile the sharp feature at -23 ppm gradually decreases in intensity. (c) LiV_6O_{13} from 25 to 150°C. Same as $Li_2V_6O_{13}$, a new Li site at -4 ppm becomes present once the temperature rises above 90°C and the -23 ppm peak decreases in intensity and totally diminishes at 130°C.

^{7}Li *ex situ* VT NMR on $Li_2V_6O_{13}$ shows change in the two main resonances. A new Li peak at -4 ppm is present above 90°C, which comes as an expense of the disappearance of the resonance at -23 ppm (Figure 5.9, left). The 15 ppm peak also shifts to 11 ppm when temperature rises from 25°C to 150°C. ^{7}Li *ex situ* VT NMR on LiV_6O_{13} also shows the formation of a new peak around -4 ppm at temperatures above 100°C (Figure 5.9, right). The onset temperature (90°C) is in line with the highest temperature that phase 2 is observed in the *in situ* XRD experiments.

5.4 Density functional theory calculations

The low energy structures from V_6O_{13} to $Li_9V_6O_{13}$ predicted by the computational structural search (see Chapter 2, Section 2.4 for more details) show that the lattice parameters are very sensitive to the Li positions (Table 5.2). The DFT calculated structures and their lattice parameter changes serve as a database to predict the possible $Li_xV_6O_{13}$ structures that are formed during HT cycling based on the lattice parameters extracted from *in situ* XRD. For the highly lithiated phases, such as $Li_7V_6O_{13}$ and $Li_8V_6O_{13}$, the formation energy of the structure

on the convex hull is much lower than the other configurations. Therefore, these structures are highly considered as the ones formed during HT cycling.

Table 5.2. DFT calculated low energy structures of $Li_xV_6O_{13}$ close to the convex Hull (within the energy variation range at room temperature). Full occupancy of Li(3) site only corresponds to one Li in a unit formula due to symmetry (half the multiplicity of the other Li sites, as can be deduced from the Wyckoff positions presented in the parentheses), while the other sites all correspond to two. All expansion rates are calculated by the equation $\frac{(v-v_{pristine})}{v_{pristine}}$, where *v* is the lattice parameter *a*, *b*, *c*, and unit cell volume *V*.

x in	Lattice parameters			Li sites					
$Li_xV_6O_{13}$	*a* (%)	*b* (%)	*c* (%)	Li1 (4*i*)	Li2 (4*i*)	Li3 (2*a*)	Li4 (4*i*)	Li5 (4*i*)	Li6 (4*i*)
0	0.0	0.0	0.0	-	-	-	-	-	-
1	0.5	-0.2	3.5	1/2	-	-	-	-	-
	2.2	0.3	0.0	-	1/2	-	-	-	-
	1.1	1.4	-0.1	-	-	-	1/2	-	-
2	1.3	1.9	2.7	-	1/2	-	-	1/2	-
	0.9	-2.4	8.5	1	-	-	-	-	-
	2.6	2.2	0.4	-	1	-	-	-	-
3	3.3	2.8	0.9	-	1	-	-	-	1/2
	1.5	4.5	1.5	-	1	-	1/2	-	-
	1.6	4.2	0.7	-	1/2	-	1/2	1/2	-
	0.2	5.5	0.4	-	-	1	1	-	-
4	1.9	4.7	2.3	-	1	-	1/2	1/2	-
	2.2	4.1	3.1	-	-	1	1	-	1/2
	0.6	6.4	0.9	-	-	1	1	1/2	-
	1.4	5.0	2.3	-	1/2	1	1	-	-
5	3.7	5.2	1.5	-	1	-	1/2	1	-
	6.1	5.3	-0.8	-	-	1	1	-	1
	3.0	6.2	1.3	-	-	1	1	1/2	1/2
	2.6	6.7	0.8	-	1/2	1	1	-	1/2
	2.4	6.7	1.4	-	-	1	1	1/2	1/2
	4.0	5.5	1.3	-	1/2	1	1	-	1/2
6	4.7	5.1	3.3	-	1	-	1/2	1	1/2
	6.0	6.7	-0.8	-	1/2	1	1	-	1
7	6.4	5.4	3.3	-	1	-	1/2	1	1
8	6.5	6.0	4.1	-	1	-	1	1	1
9	5.9	9.4	2.6	-	1	1	1	1	1

5.5 Discussion

The VT *in situ* XRD experiments give insights into the influence of temperature on the change of phase transition mechanisms during first discharge at HT. The two major differences at HT are 1) the disappearance of phase 2 above 100°C and 2) the extended solubility range of phase 4 with increasing temperature.

5.5.1 Disappearance of phase 2 above 100°C

The disappearance of phase 2 above 100°C is observed only during *in situ* experiments but not *ex situ*. The fact suggests that phase 2 cannot be formed by electrochemical Li insertion above 100°C. However, once phase 2 is formed at RT, it remains single phase when heated above 100°C.

Phase 2 should readily decompose into other phases if the disappearance of phase 2 during HT electrochemical lithiation is due to the metastability of phase 2. Because $Li_2V_6O_{13}$ is in the miscibility gap above 100°C (see Figure 5.5), the single phase $Li_2V_6O_{13}$ obtained at 25°C should phase separate into a mixture of phase 1 and phase 3 as temperature increases. However, VT *ex situ* XRD on $Li_2V_6O_{13}$ shows no evidence of this hypothesised phase separation (Figure 5.8). Both *ex situ* NMR and XRD indicate that a second order phase transition is present in phase 2 at around 100°C (Figure 5.8 and 5.9). Either the Li environment or the electronic/magnetic properties of this material changes at this temperature, evidenced by the disappearance of -23 ppm and growth of the -4 ppm resonances in the NMR spectra. This onset temperature also marks the start of expansion of lattice parameter *c*, which shrinks from 25°C to 100°C. The lattice parameter changes continuously from 25°C to 150°C, but the first order derivative of the lattice parameter changes discontinuously from negative to positive at 100°C. Given that DFT calculation (Chapter 2, Section 2.4) has shown that the lattice parameters are extremely sensitive to the Li positions (Chapter 4, Section 4.3 and Table 5.2), it is unlikely for the Li ions to rearrange because this will highly likely cause abrupt changes of lattice parameters, which is not observed. Therefore, the change of Li resonances shown in the NMR spectra is possibly due to the change of either electronic or magnetic properties of the material with temperature change. The origin of the change of properties is still under investigation, but it is clear that the transition from the low temperature (LT) phase 2 to HT phase 2 at 100°C is second order. During HT electrochemical lithiation (above 100°C), HT phase 2 cannot be formed. Because ionic and electronic conductivities are the factors affecting the electrochemical performance

of a material, it is valid to postulate that it is the electronic properties of HT phase 2 that hinders its formation at temperatures above 100°C.

It is also worthwhile to note that *c* lattice parameter of LT phase 2 shrinks with temperature increase. At RT in phase 2, the Li ions occupying the Li(1) position lead to further distortion of the VO_6 octahedra in the single layer (Figure 4.9). V(1) that is close to Li(1) changes from 6 to 5-coordinate vanadium. The average V(1)-O bonding distance increases. Especially, V(1)-O(5) becomes too lengthy to be considered a bond (refer to Figure 1.9 for the atom numeration in the unit cell). When the material is heated, the electrons become more delocalised. The charge ordering of phase 2 that is predicted by DFT calculation (Figure 4.10) is weakened upon heating. As the electron density distribute more evenly among the three vanadium environments, V(1) should become less off-centred in an octahedral VO_6 environment and finally restore to a 6-coordinate vanadium. As this process goes on with increasing temperature, the V(1)-O(5) bond distance shortens, resulting in the overall shrinkage along the *c* direction. Therefore, from 25 °C to 100°C, the more delocalised electrons result in the observed negative thermal expansion (shrinkage along *c*). Once the temperature reaches 100°C, all vanadium atoms become 6-coordinate and thermal expansion results in the lattice parameter increase.

5.5.2 Higher capacity due to more Li insertion into phase 4 at high temperature

Phase 4 has a much larger Li solubility at HT compared with RT (Figure 5.5). Utilising the DFT calculated structures (Table 5.2), it is possible to predict the structures in the extended phase 4 solid solution region at HT, which explains why V_6O_{13} has 12% more discharge capacity and how it accommodates the extra Li in the material.

From 25°C to 125°C, the range of solid solution phase 4 region expands at two ends. The lower limit reaches down from 6.2 to 5.2 and the upper limit increases from 6.7 to 8.0 Li per formula unit. The change of electrolyte from organic to IL electrolyte at 75°C influences the lower limit but not the upper. This is most likely associated with the dissociation energy of Li ions being less in the organic electrolyte compared with the IL. In a simplified model of a heterogeneous system with two solids (phase 3 and phase 4) and one liquid (electrolyte), the Li ion dissociation energy in the liquid controls the gradient and accessibility of the Li ions surrounding the electrode material (phase 3), tuning the composition of the incipient phase 4.

At 125°C, the incipient composition of phase 4 $Li_{5.2}V_6O_{13}$ is an intermediate composition between $Li_5V_6O_{13}$ and $Li_6V_6O_{13}$. The DFT calculated structures indicate that this structure has Li(2), Li(4), Li(5), and Li(6) sites fully or partially filled.

The DFT calculated $Li_7V_6O_{13}$ and $Li_8V_6O_{13}$ structures give insights into the extra Li sites that get filled at HT and the possible sequence of Li sites filling. The lowest energy $Li_7V_6O_{13}$ phase has a much lower formation energy compared with the other structures. Therefore, it is likely to be the only possible phase that is formed. Li(2), Li(5), and Li(6) are fully occupied while Li(4) is half occupied in this phase. When phase 4 exhibits extra capacity at HT, the half-filled Li(4) site keeps on intercalating Li and forms the lowest energy $Li_8V_6O_{13}$. Based on the calculation, this continuous filling of Li(4) results in an expansion of 0.6% along *b* and 0.8% along *c*, corresponding well with the *in situ* XRD results. However, *a*, *b*, and *c* expand more isotropically in phase 4 at HT, due to the fact that, at HT, Li ions not only have more energies to occupy the high energy Li defect sites they cannot access at RT, they also have more energies to hop between defect sites, making all the sites accessible at the same time. Since the changes in lattice parameters are driven by the positions occupied by Li in the crystal structure, the ability to populate all sites more equally may cause the cell to expand more isotropically at HT.

At HT, the between layer Li2), Li(5) and Li(6) sites become accessible in phase 4 at a smaller Li concentration, and can be occupied to a more puckered state at higher Li concentration, resulting the widening of the solubility window. The lattice parameters change in all three directions at 125°C instead of expanding solely along a at 25°C, suggesting that the between layer Li(2), Li(5), and Li(6) sites and within layer Li(4) site, affecting lattice parameter change in different directions, get filled at the same time, not in a sequential order.

5.6 Conclusion

In conclusion, the first cycle of cathode LIB material V_6O_{13} was investigated using electrochemistry, *in situ* XRD, *ex situ* VT XRD, *ex situ* VT NMR, and DFT calculations. The material still transforms via an alternating solid solution and two-phase mechanism at HT. However, at temperatures above 100°C, phase 2 can no longer be formed during discharge, which is in line with a more sloping electrochemical discharge profile. A single-phase phase 2 can be formed at RT and remain structurally stable up to 150°C, but cannot be formed via electrochemical lithiation above 100°C. Instead phase 3 nucleates from phase 1 directly during discharge above 100°C. Both ^{7}Li VT NMR and *ex situ* XRD suggest that there is a second order phase transition in phase 2 at 100°C, which is highly likely to be electronic. The HT phase 2 is difficult to be electrochemically formed above 100°C and the reason is still under investigation. The negative thermal expansion in phase 2 below 100°C is attributed to a V-O framework with more delocalised electrons, resulting in a change of V(1) from 5-coordinate to 6-coordinate and V(1)-O bond lengths to be reduced. The decrease in V(1)-O bond length leads to an overall reduction in the *c* lattice parameter, which ultimately results in the negative thermal expansion observed in both the *in situ* and *ex situ* XRD experiments.

At HT, the solubility range of phase 4 widens. Therefore, phase 4 nucleates within phase 3 at a smaller Li composition and takes in more Li at HT than RT. The Li rich phase 4 is able to insert more Li because Li ions have more energy to fully occupy Li(4) at HT. However, Li ions intercalate the Li puckered phase 4 differently at HT. A few Li sites get occupied at the same time, instead of in a sequential order as it does at RT. The more Li solubility in this phase leads to more than 12% capacity increase during electrochemical testing, making V_6O_{13} a great candidate for HT battery cathode material.

6 Conclusion and outlook

To understand the effect of temperature on phase transformation mechanisms in electrodes for LIBs, two structures: $LiFePO_4$ and V_6O_{13} were investigated using VT *in situ* synchrotron XRD, along with other techniques, such as electrochemistry, NMR and DFT calculations.

A HT *in situ* sXRD setup was developed to perform real-time investigations on battery electrode materials during electrochemical cycling at HT. The *in situ* cell had well distributed chemically inert conducting and insulating cell parts, adequate stack pressure, and airtight sealing to enable battery discharging and charging from low to high cycling rates. The cell was designed with integrated heating and temperature control systems that allow it to be heated up to 250^{o}C. The cell work in an X-ray transmission mode and allowed time-resolved XRD experiments to be done in real time during electrochemical cycling.

A series of *in situ* XRD experiments were performed on $LiFePO_4$ during high rate cycling from RT to 150^{o}C. While RT high rate cycling of $LiFePO_4$ in the new HT *in situ* XRD setup reproduced the current induced solid solution phase transition mechanism at high rates, suppression of this current induced metastable phase at HT was observed. The suppressed solid solution behaviour implied a possible competing phase transition mechanism between the current induced single-phase solid solution and two-phase nucleation and growth, governed possibly by Li diffusion rate. Also, the VT setup was able to monitor the change in $LiFePO_4$ structure and attribute the cause of battery failure at 75 and 100^{o}C to the insufficient ionic conductivity of the IL electrolyte.

The disclosure of the phase transition mechanisms of V_6O_{13} at both RT and HT were also aided by *in situ* XRD. An alternating solid solution and two-phase mechanism was proposed based on *in situ* XRD. At RT, the material featured an asymmetric six-step discharge and five-step charge, involving four phases (with the name phase 1, 2, 3, and 4), and expanded/shrank in a sequential order along *a*, *b* and *c* axes. DFT calculations showed that the sequential change was accompanied by significant electronic rearrangements, which were related to changes in the occupancy of Li ions in different Li sites in the unit cell and charge ordering. Phase 2 was formed on discharge via a second-order phase transition but not on charge, resulting in the asymmetric electrochemistry and phase transition mechanism. A different NMR spectrum was observed for phase 2 showing more Li environments compared with other phases implied more defects created due to the high strain in this phase. The huge change in lattice parameters from phase 2 to phase 3 also

caused a large interfacial energy, which could hinder the formation of phase 2 upon charge. At temperatures above 100^{o}C, phase 2 can no longer be formed during discharge, which was in line with a more sloping electrochemical discharge profile. Phase 2 remained structurally stable up to 150^{o}C, but could not be formed via electrochemical lithiation above 100^{o}C. ^{7}Li VT NMR spectra revealed evidence of a new Li site above 90^{o}C in both phase 1 and phase 2. The occupancy of this new Li site possibly aided the nucleation of phase 3 locally when the material reaches the end composition of phase 1 above 90^{o}C, bypassing phase 2. At HT, the solubility range of phase 4 widens. Therefore, phase 4 nucleated within phase 3 at a smaller Li composition and took in more Li at HT than RT. The Li rich phase 4 was able to insert more Li because Li ions had more energy to fully occupy Li(4) at HT. However, Li ions intercalated the Li puckered phase 4 in a different way at HT, occupying a few Li sites simultaneously, instead of in a sequential order as it did at RT.

Because particle size is a parameter that influences the phase transition mechanisms of electrode materials, further investigation on the effects of particle size on $LiFePO_4$ and V_6O_{13} at VT is underway. Since both materials have changes in the range of miscibility gaps at VT, it is of great scientific interest to understand the effect of particle size at VT. The application of V_6O_{13} is hindered partially due to the poor high rate performance of this material. Because two-phase mechanisms are normally regarded as kinetically limited and size reduction may prove useful in shrinking miscibility gaps at high rates at certain temperatures, the rate performance of V_6O_{13} could potentially benefit from particle size reduction and the material could have an even wider application in the industry.

Meanwhile, the investigation techniques and knowledge gained from LIBs systems are transferable to new systems, such as all solid-state batteries. Studies of all solid-state batteries are becoming increasingly exciting due to successful demonstrations of rapid preparation through spark plasma sintering over the past few years, and recent safety concerns of conventional LIBs containing flammable organic liquid electrolytes. However, many of the electrolyte decomposition problems at high voltage are still present in ion-conducting solid electrolytes, and remain to be studied owing to the complex and multi-component nature of assembled devices. Unfortunately, the benefits of inherent safety and low self-discharge rates in all solid-state batteries result from slow ion diffusion in solid electrolytes (e.g. Li^{+} ions), which comes with the undesired side-effect that electrochemical cycling must be performed on the order of 100 hours (C/100). Additionally, preliminary investigation on high-performance cathode and electrolyte materials using electron microscopy, *ex situ* NMR, as well as *ex situ* XRD have identified that decomposition occurs,

which must be investigated further using *in situ* techniques in order to design better and more compatible materials.

Other systems like Na-ion batteries are developed in parallel as alternatives/backups for the current state-of-art LIB technology. Preliminary results on $NaFePO_4$ materials have shown the high rate capability of this material. A combination of electrochemistry, *in situ* XRD, and NMR techniques are underway to understand the phase transition mechanisms behind the phenomenon.

References

(1) Tarascon, J. M.; Armand, M. Issues and Challenges Facing Rechargeable Lithium Batteries. *Nature* **2001**, *414* (6861), 359–367.

(2) Armand, M.; Tarascon, J.-M. Building Better Batteries. *Nature* **2008**, *451* (7179), 652–657.

(3) Nazri, G. A.; Pistoia, G. *Lithium Batteries - Science and Technology*; Springer, 2009.

(4) Huggins, R. A. *Advanced Batteries - Materials Science Aspects*; 2009.

(5) Tarascon, J.; Poizot, P.; Laruelle, S.; Grugeon, S.; Dupont, L. Nano-Sized Transition-Metal Oxides as Negative-Electrode Materials for Lithium-Ion Batteries. *Nature* **2000**, *407* (6803), 496–499.

(6) Boukamp, B. A.; Lesh, G. C.; Huggins, R. A. All-Solid Lithium Electrodes with Mixed-Conductor Matrix. *J. Electrochem. Soc.* **1981**, *128* (4), 725–729.

(7) Reimers, J. N.; Dahn, J. R. Electrochemical and in Situ X-Ray Diffraction Studies of Lithium Intercalation in LixCoO2. *J. Electrochem. Soc.* **1992**, *139* (8), 2091–2097.

(8) Pecher, O.; Carretero-González, J.; Griffith, K. J.; Grey, C. P. Materials' Methods: NMR in Battery Research. *Chem. Mater.* **2017**, *29* (1), 213–242.

(9) Armand, M.; Endres, F.; MacFarlane, D. R.; Ohno, H.; Scrosati, B. Ionic-Liquid Materials for the Electrochemical Challenges of the Future. *Nat. Mater.* **2009**, *8* (8), 621–629.

(10) Tarascon, J.-M. Key Challenges in Future Li-Battery Research. *Philos. Trans. A. Math. Phys. Eng. Sci.* **2010**, *368* (1923), 3227–3241.

(11) Scrosati, B.; Garche, J. Lithium Batteries: Status, Prospects and Future. *J. Power Sources* **2010**, *195* (9), 2419–2430.

(12) Pinson, M. B.; Bazant, M. Z. Theory of SEI Formation in Rechargeable Batteries: Capacity Fade, Accelerated Aging and Lifetime Prediction. *J. Electrochem. Soc.* **2012**, *160* (2), A243–A250.

(13) Kim, S.-P.; Duin, A. C. T. Van; Shenoy, V. B. Effect of Electrolytes on the Structure and Evolution of the Solid Electrolyte Interphase (SEI) in Li-Ion Batteries: A Molecular Dynamics Study. *J. Power Sources* **2011**, *196* (20), 8590–8597.

(14) Palacin, M. R.; de Guibert, A. Why Do Batteries Fail? *Science (80-.).* **2016**, *351* (6273), 1253292–1253292.

(15) Ota, H.; Sato, T.; Suzuki, H.; Usami, T. TPD–GC/MS Analysis of the Solid Electrolyte Interface (SEI) on a Graphite Anode in the Propylene Carbonate/ethylene Sulfite

Electrolyte System for Lithium Batteries. *J. Power Sources* **2001**, *97–98*, 107–113.

(16) Amatucci, G.; Du Pasquier, A.; Blyr, A.; Zheng, T.; Tarascon, J. M. The Elevated Temperature Performance of the LiMn2O4/C System: Failure and Solutions. *Electrochim. Acta* **1999**, *45* (1–2), 255–271.

(17) Xu, K. Nonaqueous Liquid Electrolytes for Lithium-Based Rechargeable Batteries. *Chem. Rev.* **2004**, *104* (10), 4303–4417.

(18) Park, O. K.; Cho, Y.; Lee, S.; Yoo, H.-C.; Song, H.-K.; Cho, J. Who Will Drive Electric Vehicles, Olivine or Spinel? *Energy Environ. Sci.* **2011**, *4*, 1621.

(19) Hensley, D.; Milewits, M.; Zhang, W. *The Evolution of Oilfield Batteries*; Rosharon, Texas, USA, 1998.

(20) Guidotti, R. a.; Reinhardt, F. W.; Odinek, J. Overview of High-Temperature Batteries for Geothermal and Oil/gas Borehole Power Sources. *J. Power Sources* **2004**, *136* (2), 257–262.

(21) Andersson, a. M.; Edström, K. Chemical Composition and Morphology of the Elevated Temperature SEI on Graphite. *J. Electrochem. Soc.* **2001**, *148* (10), A1100.

(22) Andersson, A. M.; Edström, K.; Rao, N.; Wendsjö, Å. Temperature Dependence of the Passivation Layer on Graphite. *J. Power Sources* **1999**, *81–82*, 286–290.

(23) Jow, T. .; Ding, M. .; Xu, K.; Zhang, S. .; Allen, J. .; Amine, K.; Henriksen, G. . Nonaqueous Electrolytes for Wide-Temperature-Range Operation of Li-Ion Cells. *J. Power Sources* **2003**, *119–121*, 343–348.

(24) Guyomard, D.; Tarascon, J. M. Li Metal-Free Rechargeable LiMn2O4/carbon Cells: Their Understanding and Optimization. *J. Electrochem. Soc.* **1992**, *139* (4), 937–948.

(25) Tarascon, J. M.; Mckinnon, W. R.; Coowar, F.; Bowmer, T. N.; Amatucci, G.; Guyomard, D. Synthesis Conditions and Oxygen Stoichiometry Effects on Li Insertion into the Spinel LiMn2O4. *J. Electrochem. Soc.* **1994**, *141* (6), 1421–1431.

(26) Etacheri, V.; Marom, R.; Elazari, R.; Salitra, G.; Aurbach, D. Challenges in the Development of Advanced Li-Ion Batteries: A Review. *Energy Environ. Sci.* **2011**, *4* (9), 3243–3262.

(27) Botte, G. G.; White, R. E.; Zhang, Z. Thermal Stability of LiPF6-EC:EMC Electrolyte for Lithium Ion Batteries. **2001**, *98*, 570–575.

(28) Finegan, D. P.; Scheel, M.; Robinson, J. B.; Tjaden, B.; Hunt, I.; Mason, T. J.; Millichamp, J.; Michiel, M. Di; Offer, G. J.; Hinds, G.; Brett, D. J. L.; Shearing, P. R. Lithium-Ion Batteries during Thermal Runaway. *Nat. Commun.* **2015**, *6*, 1–10.

(29) Quartarone, E.; Mustarelli, P. Electrolytes for Solid-State Lithium Rechargeable

Batteries: Recent Advances and Perspectives. *Chem. Soc. Rev.* **2011**, *40*, 2525–2540.

(30) Lewandowski, A.; Świderska-Mocek, A. Ionic Liquids as Electrolytes for Li-Ion batteries—An Overview of Electrochemical Studies. *J. Power Sources* **2009**, *194* (2), 601–609.

(31) Jin, J.; Li, H. H.; Wei, J. P.; Bian, X. K.; Zhou, Z.; Yan, J. Li/LiFePO4 Batteries with Room Temperature Ionic Liquid as Electrolyte. *Electrochem. commun.* **2009**, *11* (7), 1500–1503.

(32) Lewandowski, A. P.; Hollenkamp, A. F.; Donne, S. W.; Best, A. S. Cycling and Rate Performance of Li–$LiFePO_4$ Cells in Mixed FSI–TFSI Room Temperature Ionic Liquids. *J. Power Sources* **2010**, *195* (7), 2029–2035.

(33) Zhang, S.; Sun, N.; He, X.; Lu, X.; Zhang, X. Physical Properties of Ionic Liquids: Database and Evaluation. *J. Phys. Chem. Ref. Data* **2006**, *35* (4), 1475–1517.

(34) Endres, F. Ionic Liquids: Solvents for the Electrodeposition of Metals and Semiconductors. *Chemphyschem* **2002**, *3* (2), 145–154.

(35) Earle, M. J.; Esperança, J. M. S. S.; Gilea, M. a; Lopes, J. N. C.; Rebelo, L. P. N.; Magee, J. W.; Seddon, K. R.; Widegren, J. a. The Distillation and Volatility of Ionic Liquids. *Nature* **2006**, *439* (7078), 831–834.

(36) Vijayaraghavan, R.; Surianarayanan, M.; Armel, V.; MacFarlane, D. R.; Sridhar, V. P. Exothermic and Thermal Runaway Behaviour of Some Ionic Liquids at Elevated Temperatures. *Chem. Commun. (Camb).* **2009**, *13* (41), 6297–6299.

(37) Bayley, P. M.; Best, A. S.; MacFarlane, D. R.; Forsyth, M. Transport Properties and Phase Behaviour in Binary and Ternary Ionic Liquid Electrolyte Systems of Interest in Lithium Batteries. *Chemphyschem* **2011**, *12* (4), 823–827.

(38) Sakaebe, H.; Matsumoto, H. N-Methyl-N-Propylpiperidinium Bis(trifluoromethanesulfonyl)imide (PP13–TFSI) – Novel Electrolyte Base for Li Battery. *Electrochem. commun.* **2003**, *5* (7), 594–598.

(39) Howlett, P. C.; MacFarlane, D. R.; Hollenkamp, A. F. High Lithium Metal Cycling Efficiency in a Room-Temperature Ionic Liquid. *Electrochem. Solid-State Lett.* **2004**, *7* (5), A97.

(40) MacFarlane, D. R.; Pringle, J. M.; Howlett, P. C.; Forsyth, M. Ionic Liquids and Reactions at the Electrochemical Interface. *Phys. Chemstry Chem. Phys.* **2010**, *12* (8), 1659–1669.

(41) Howlett, P. C.; MacFarlane, D. R.; Hollenkamp, A. F. High Lithium Metal Cycling Efficiency in a Room-Temperature Ionic Liquid. *Electrochem. Solid-State Lett.* **2004**, *7*

(5), A97–A101.

(42) Howlett, P. C.; Brack, N.; Hollenkamp, a. F.; Forsyth, M.; MacFarlane, D. R. Characterization of the Lithium Surface in N-Methyl-N-Alkylpyrrolidinium Bis(trifluoromethanesulfonyl)amide Room-Temperature Ionic Liquid Electrolytes. *J. Electrochem. Soc.* **2006**, *153* (3), A595.

(43) Bayley, P. M.; Best, a S.; MacFarlane, D. R.; Forsyth, M. The Effect of Coordinating and Non-Coordinating Additives on the Transport Properties in Ionic Liquid Electrolytes for Lithium Batteries. *Phys. Chem. Chem. Phys.* **2011**, *13* (10), 4632–4640.

(44) Smart, M. C.; Ratnakumar, B. V.; Whitcanack, L. D.; Chin, K. B.; Surampudi, S.; Croft, H.; Tice, D.; Staniewicz, R. Improved Low-Temperature Performance of Lithium-Ion Cells with Quaternary Carbonate-Based Electrolytes. *J. Power Sources* **2003**, *119–121*, 349–358.

(45) Ding, M. S.; Xu, K.; Zhang, S. S.; Amine, K.; Henriksen, G. L.; Jow, T. R. Change of Conductivity with Salt Content, Solvent Composition, and Temperature for Electrolytes of LiPF[sub 6] in Ethylene Carbonate-Ethyl Methyl Carbonate. *J. Electrochem. Soc.* **2001**, *148* (10), A1196.

(46) Padhi, A. K.; Nanjundaswamy, K. S.; Goodenough, J. B. Phospho-Olivines as Positive-Electrode Materials for Rechargeable Lithium Batteries. *J. Electrochem. Soc.* **1997**, *144* (4), 1188–1194.

(47) Padhi, A. K.; Nanjundaswamy, K. S.; Masquelier, C.; Okada, S.; Goodenough, J. B. Effect of Structure on the Fe3+/Fe2+ Redox Couple in Iron Phosphates. *J. Electrochem. Soc.* **1997**, *144* (5), 1609–1613.

(48) Malik, R.; Abdellahi, A.; Ceder, G. A Critical Review of the Li Insertion Mechanisms in LiFePO4 Electrodes. *J. Electrochem. Soc.* **2013**, *160* (5), 3179–3197.

(49) MacNeil, D. D.; Lu, Z.; Chen, Z.; Dahn, J. R. A Comparison of the Electrode/electrolyte Reaction at Elevated Temperatures for Various Li-Ion Battery Cathodes. *J. Power Sources* **2002**, *108* (1–2), 8–14.

(50) Yamada, A.; Chung, S. C.; Hinokuma, K. Optimized LiFePO4 for Lithium Battery Cathodes. *J. Electrochem. Soc.* **2001**, *148* (3), A224.

(51) Huang, H.; Yin, S.-C.; Nazar, L. F. Approaching Theoretical Capacity of LiFePO4 at Room Temperature at High Rates. *Electrochem. Solid-State Lett.* **2001**, *4* (10), A170.

(52) Chen, Z.; Dahn, J. R. Reducing Carbon in LiFePO4/C Composite Electrodes to Maximize Specific Energy , Volumetric Energy , and Tap Density. *J. Electrochem. Soc.* **2002**, *149* (9), 1184–1189.

(53) Thackeray, M. M.; Johnson, P. J.; de Picciotto, L. A.; Bruce, P. G.; Goodenough, J. B. Electrochemical Extraction of Lithium from LiMn2O4. *Mater. Res. Bull.* **1984**, *19* (2), 179–187.

(54) Ohzuku, T.; Makimura, Y. Layered Lithium Insertion Material of LiNi1/2Mn1/2O2: A Possible Alternative to LiCoO2 for Advanced Lithium-Ion Batteries. *Chem. Lett.* **2001**, *2*, 744–745.

(55) Thackeray, M. M.; Wolverton, C.; Isaacs, E. D. Electrical Energy Storage for Transportation—approaching the Limits Of, and Going Beyond, Lithium-Ion Batteries. *Energy Environ. Sci.* **2012**, *5* (7), 7854.

(56) Menetrier, M.; Saadoune, I.; Levasseur, S.; Delmas, C. The Insulator – Metal Transition upon Lithium Deintercalation from LiCoO2: Electronic Properties and 7Li NMR Study. *J. Mater. Chem.* **1999**, *9*, 1135–1140.

(57) Yamada, A.; Koizumi, H.; Nishimura, S.; Sonoyama, N.; Kanno, R.; Yonemura, M.; Nakamura, T.; Kobayashi, Y. Room-Temperature Miscibility Gap in LixFePO4. *Nat. Mater.* **2006**, *5* (5), 357–360.

(58) Malik, R.; Zhou, F.; Ceder, G. Kinetics of Non-Equilibrium Lithium Incorporation in LiFePO4. *Nat. Mater.* **2011**, *10* (8), 587–590.

(59) Cabana, J.; Shirakawa, J.; Chen, G.; Richardson, T. J.; Grey, C. P. MAS NMR Study of the Metastable Solid Solutions Found in the LiFePO 4/FePO4 System. *Chem. Mater.* **2010**, *22* (3), 1249–1262.

(60) Delacourt, C.; Poizot, P.; Levasseur, S.; Masquelier, C. Size Effects on Carbon-Free LiFePO4 Powders. *Electrochem. Solid-State Lett.* **2006**, *9* (7), A352.

(61) Delacourt, C.; Poizot, P.; Tarascon, J.-M.; Masquelier, C. The Existence of a Temperature-Driven Solid Solution in LixFePO4 for 0<x<1. *Nat. Mater.* **2005**, *4* (3), 254–260.

(62) Van der Ven, A.; Garikipati, K.; Kim, S.; Wagemaker, M. The Role of Coherency Strains on Phase Stability in Li[sub x]FePO[sub 4]: Needle Crystallites Minimize Coherency Strain and Overpotential. *J. Electrochem. Soc.* **2009**, *156* (11), A949.

(63) Wagemaker, M.; Mulder, F. M.; Van Der Ven, A. The Role of Surface and Interface Energy on Phase Stability of Nanosized Insertion Compounds. *Adv. Mater.* **2009**, *21* (25–26), 2703–2709.

(64) Islam, M. S.; Driscoll, D. J.; Fisher, C. A. J.; Slater, P. R.; Group, M. C.; V, C. Di; Uni, V.; Gu, G.; Kingdom, U. Atomic-Scale Investigation of Defects , Dopants , and Lithium Transport in the LiFePO 4 Olivine-Type Battery Material. *Chem. Mater.* **2005**, *17* (11),

5085–5092.

(65) Morgan, D.; Van der Ven, a.; Ceder, G. Li Conductivity in Li[sub x]MPO[sub 4] (M = Mn, Fe, Co, Ni) Olivine Materials. *Electrochem. Solid-State Lett.* **2004**, *7* (2), A30.

(66) Maxisch, T.; Zhou, F.; Ceder, G. Ab Initio Study of the Migration of Small Polarons in Olivine Lix FePO4 and Their Association with Lithium Ions and Vacancies. *Phys. Rev. B - Condens. Matter Mater. Phys.* **2006**, *73* (10), 1–6.

(67) Nishimura, S.; Kobayashi, G.; Ohoyama, K.; Kanno, R.; Yashima, M.; Yamada, A. Experimental Visualization of Lithium Diffusion in LixFePO4. *Nat. Mater.* **2008**, *7* (9), 707–711.

(68) Ouyang, C. Y.; Shi, S. Q.; Wang, Z. X.; Li, H.; Huang, X. J.; Chen, L. Q. The Effect of Cr Doping on Li Ion Diffusion in LiFePO 4 from First Principles Investigations and Monte Carlo Simulations. *J. Phys. Condens. Matter* **2004**, *16* (16), 2265–2272.

(69) Adams, S. Lithium Ion Pathways in LiFePO 4 and Related Olivines. *J. Solid State Electrochem.* **2010**, *14* (10), 1787–1792.

(70) Malik, R.; Burch, D.; Bazant, M.; Ceder, G. Particle Size Dependence of the Ionic Diffusivity. *Nano Lett.* **2010**, *10* (10), 4123–4127.

(71) Laffont, L.; Delacourt, C.; Gibot, P.; Wu, M. Y.; Kooyman, P.; Masquelier, C.; Tarascon, J. M. Study of the LiFePO4/FePO4 Two-Phase System by High-Resolution Electron Energy Loss Spectroscopy. *Chem. Mater.* **2006**, *18* (5), 5520–5529.

(72) Chen, G.; Song, X.; Richardson, T. J. Electron Microscopy Study of the LiFePO4 to FePO4 Phase Transition. *Electrochem. Solid-State Lett.* **2006**, *9* (6), A295.

(73) Weichert, K.; Sigle, W.; van Aken, P. a; Jamnik, J.; Zhu, C.; Amin, R.; Acartürk, T.; Starke, U.; Maier, J. Phase Boundary Propagation in Large LiFePO4 Single Crystals on Delithiation. *J. Am. Chem. Soc.* **2012**, *134* (6), 2988–2992.

(74) Delmas, C.; Maccario, M.; Croguennec, L.; Le Cras, F.; Weill, F. Lithium Deintercalation in LiFePO4 Nanoparticles via a Domino-Cascade Model. *Nat. Mater.* **2008**, *7* (8), 665–671.

(75) Orvananos, B.; Malik, R.; Yu, H. C.; Abdellahi, A.; Grey, C. P.; Ceder, G.; Thornton, K. Architecture Dependence on the Dynamics of Nano-liFePO4 Electrodes. *Electrochim. Acta* **2014**, *137*, 245–257.

(76) Bai, P.; Cogswell, D. A.; Bazant, M. Z. Suppression of Phase Separation in LiFePO4 Nanoparticles during Battery Discharge. *Nano Lett.* **2011**, *11* (11), 4890–4896.

(77) Liu, H.; Strobridge, F. C.; Borkiewicz, O. J.; Wiaderek, K. M.; Chapman, K. W.; Chupas, P. J.; Grey, C. P. Capturing Metastable Structures during High-Rate Cycling of $LiFePO_4$

Nanoparticle Electrodes. *Science* **2014**, *344* (6191), 1252817.

(78) Zhou, F.; Maxisch, T.; Ceder, G. Configurational Electronic Entropy and the Phase Diagram of Mixed-Valence Oxides: The Case of LixFePO4. *Phys. Rev. Lett.* **2006**, *97* (15), 1–4.

(79) Delacourt, C.; Poizot, P.; Tarascon, J.-M.; Masquelier, C. The Existence of a Temperature-Driven Solid Solution in LixFePO4 for 0 ≤ X ≤ 1. *Nat. Mater.* **2005**, *4* (March), 254–260.

(80) Dodd, J. L.; Yazami, R.; Fultz, B. Phase Diagram of LixFePO4. *Electrochem. Solid-State Lett.* **2006**, *9* (3), A151.

(81) Ellis, B.; Perry, L. K.; Ryan, D. H.; Nazar, L. F. Small Polaron Hopping in Li X FePO4 Solid Solutions: Coupled Lithium-Ion and Electron Mobility. *J. Am. Chem. Soc.* **2006**, *128* (2), 11416–11422.

(82) Gu, L.; Zhu, C.; Li, H.; Yu, Y.; Li, C.; Tsukimoto, S.; Maier, J.; Ikuhara, Y. Direct Observation of Lithium Staging in Partially Delithiated LiFePO 4 at Atomic Resolution. *J. Am. Chem. Soc.* **2011**, *133* (13), 4661–4663.

(83) Chen, G.; Song, X.; Richardson, T. J. Metastable Solid-Solution Phases in the LiFePO[sub 4]⁄FePO[sub 4] System. *J. Electrochem. Soc.* **2007**, *154* (7), A627.

(84) Zhang, S. S.; Xu, K.; Jow, T. R. An Improved Electrolyte for the LiFePO4 Cathode Working in a Wide Temperature Range. *J. Power Sources* **2006**, *159* (1), 702–707.

(85) Zaghib, K.; Ravet, N.; Gauthier, M.; Gendron, F.; Mauger, A.; Goodenough, J. B.; Julien, C. M. Optimized Electrochemical Performance of LiFePO4 at 60 ??C with Purity Controlled by SQUID Magnetometry. *J. Power Sources* **2006**, *163* (1 SPEC. ISS.), 560–566.

(86) Amine, K.; Liu, J.; Belharouak, I. High-Temperature Storage and Cycling of C-LiFePO4/graphite Li-Ion Cells. *Electrochem. commun.* **2005**, *7* (7), 669–673.

(87) Chang, H.-H.; Wu, H.-C.; Wu, N.-L. Enhanced High-Temperature Cycle Performance of LiFePO4/carbon Batteries by an Ion-Sieving Metal Coating on Negative Electrode. *Electrochem. commun.* **2008**, *10* (12), 1823–1826.

(88) Chang, H.-H.; Chang, C.-C.; Su, C.-Y.; Wu, H.-C.; Yang, M.-H.; Wu, N.-L. Effects of TiO2 Coating on High-Temperature Cycle Performance of LiFePO4-Based Lithium-Ion Batteries. *J. Power Sources* **2008**, *185* (1), 466–472.

(89) Maccario, M.; Croguennec, L.; Le Cras, F.; Delmas, C. Electrochemical Performances in Temperature for a C-Containing LiFePO4 Composite Synthesized at High Temperature. *J. Power Sources* **2008**, *183* (1), 411–417.

(90) Mestre-Aizpurua, F.; Hamelet, S.; Masquelier, C.; Palacín, M. R. High Temperature Electrochemical Performance of Nanosized LiFePO4. *J. Power Sources* **2010**, *195* (19), 6897–6901.

(91) Andersson, G. Studies on Vanadium Oxides. *Acta Chem. Scand.* **1954**, *8*, 1599–1606.

(92) West, K.; Ostergwrd, M. J. L.; Jacobsen, T. Vanadium Oxides as Electrode Rechargeable Lithium Cells. *J. Power Sources* **1987**, *20* (1), 165–172.

(93) Thackeray, M. M.; Thomas, J. O.; Whittingham, M. S. Science and Applications of Mixed Conductors for Lithium Batteries. *MRS Bull.* **2000**, *25* (3), 39–46.

(94) Whittingham, M. S. Lithium Batteries and Cathode Materials. *Chem. Rev.* **2004**, *104* (10), 4271–4301.

(95) Whittingham, M. S.; Song, Y.; Lutta, S.; Zavalij, P. Y.; Chernova, N. a. Some Transition Metal (Oxy)phosphates and Vanadium Oxides for Lithium Batteries. *J. Mater. Chem.* **2005**, *15* (33), 3362.

(96) Chernova, N. a.; Roppolo, M.; Dillon, A. C.; Whittingham, M. S. Layered Vanadium and Molybdenum Oxides: Batteries and Electrochromics. *J. Mater. Chem.* **2009**, *19*, 2526.

(97) Galy, J.; Darriet, J.; Hagenmuller, P. Manuscrit Auteur, Publié dans “Revue de Chimie Minerale 8 (1971) 509-522.” *Rev. Chim. Miner.* **1971**, *8*, 509–522.

(98) Murphy, D. W.; Christian, P. A.; Disalvo, F. J.; Waszczak, J. V. Lithium Incorporation by Vanadium Pentoxide. *Inorg. Chem.* **1979**, *18* (10), 2800–2803.

(99) Cocciantelli, J. M.; Doumerc, J. P.; Pouchard, M. Crystal Chemistry of Electrochemically Inserted LixV2O5. *J. Power Sources* **1991**, *34*, 103–111.

(100) Dickens, P. G.; French, S. J.; Hight, A. T.; Pye, M. F. Phase Relationships in the Ambient Temperature LixV2O5 System (0.1<x<1.0). *Mater. Res. Bull.* **1979**, *14* (10), 1295–1299.

(101) Savariault, J.-M.; Deramond, E.; Galy, J.; Mongrelet, T.; Hirschinger, J. Lithium Insertion Study in Vanadium Oxide Bronze by NMR and X Ray Diffraction. *Mol. Cryst. Liq. Cryst. Sci. Technol. Sect. A. Mol. Cryst. Liq. Cryst.* **1994**, *244* (1), 367–372.

(102) Delmas, C.; Cognac-Auradou, H. Formation of the ω-Type Phase by Lithium Intercalation in (Mo, V) Oxides Deriving from V2O5. *J. Power Sources* **1995**, *54* (2), 406–410.

(103) Coccíantelli, J. M.; Ménétrier, M.; Delmas, C.; Doumerc, J. P.; Pouchard, M.; Hagenmuller, P. Electrochemical and Structural Characterization of Lithium Intercalation and Deintercalation in the γ-LiV2O5 Bronze. *Solid State Ionics* **1992**, *50* (1–2), 99–105.

(104) Delmas, C.; Cognac-Auradou, H.; Cocciantelli, J. M.; Menetrier, M.; Doumerc, J. P. The LixV2O5 System : An Overview of the Structure Modifications Induced by the Lithium Intercalation. *Solid state ionics* **1994**, *69*, 257–264.

(105) Delmas, C.; Brethes, S.; Menetrier, M. ω-LixV2O5 - a New Electrode Material for Rechargeable Lithium Batteries. *J. Power Sources* **1991**, *34* (2), 113–118.

(106) Leger, C.; Bach, S.; Soudan, P.; Pereira-Ramos, J.-P. Structural and Electrochemical Properties of ω -- LixV2O5 (0.4 ≤ X ≤ 3) as Rechargeable Cathodic Material for Lithium Batteries. *J. Electrochem. Soc.* **2005**, *152* (1), A236–A241.

(107) Zhang, Q.; Brady, A. B.; Pelliccione, C. J.; Bock, D. C.; Bruck, A. M.; Li, J.; Sarbada, V.; Hull, R.; Stach, E. A.; Takeuchi, K. J.; Takeuchi, E. S.; Liu, P.; Marschilok, A. C. Investigation of Structural Evolution of $Li_{1.1}V_3O_8$ by *In Situ* X-Ray Diffraction and Density Functional Theory Calculations. *Chem. Mater.* **2017**, acs.chemmater.7b00096.

(108) Murphy, D. W.; Christian, P. A.; Disalvo, F. J.; Carides, J. N. Vanadium Oxide Cathode Materials for Secondary Lithium Cells. *J. Electrochem. Soc.* **1979**, *126* (3), 497–499.

(109) West, K.; Zachau-Christiansen, B.; Jacobsen, T.; Atlung, S. V6O13 as Cathode Material for Lithium Cells. *J. Power Sources* **1985**, *14*, 235–245.

(110) Bruce, P.; Krok, F. Studies of the Interface V6O13 and Poly(ethlyene Oxide) Based Electrolytes. *Electrochim. Acta* **1988**, *33* (11), 1669–1674.

(111) Gustafsson, T.; Thomas, J. O.; Koksbang, R.; Farrington, G. C. The Polymer Battery as an Environment for in Situ X-Ray Diffraction Studies of Solid-State Electrochemical Processes. *Electrochim. Acta* **1992**, *37* (9), 1639–1643.

(112) Macklin, W. J.; Neat, R. J.; Sandhu, S. S. Structural Changes in Vanadium Oxide-Based Cathodes during Cycling in a Lithium Polymer Electrolyte Cell. *Electrochi* **1992**, *37* (9), 1715–1720.

(113) West, K.; Zachau-Christiansen, B.; Jacobsen, T. Electrochemical Properties of Non-Stoichiometric V6O13. *Electrochim. Acta* **1983**, *28* (12), 1829–1833.

(114) Murphy, D. W.; Christian, P. A.; Disalvo, F. J.; Carides, J. N.; Waszczak, J. V. Lithium Incorporation by and Related Vanadium (+ 4 , + 5) Oxide Cathode Materials. *J. Electrochem. Soc.* **1981**, *128* (10), 2053–2060.

(115) Tian, X.; Xu, X.; He, L.; Wei, Q.; Yan, M.; Xu, L.; Zhao, Y.; Yang, C.; Mai, L. Ultrathin Pre-Lithiated V6O13 Nanosheet Cathodes with Enhanced Electrical Transport and Cyclability. *J. Power Sources* **2014**, *255*, 235–241.

(116) Ding, Y. L.; Wen, Y.; Wu, C.; Van Aken, P. A.; Maier, J.; Yu, Y. 3D V6O13 Nanotextiles Assembled from Interconnected Nanogrooves as Cathode Materials for High-Energy

Lithium Ion Batteries. *Nano Lett.* **2015**, *15* (2), 1388–1394.

(117) Aebi, F. Phasenuntersuchungen Im System Vanadin-Sauerstoff Und Die Krystallstruktur Von V12O26. *Helv. Chim. Acta* **1948**, *31* (1), 8–21.

(118) Wilhelmi, K. A.; Waltersson, K.; Kihlborg, L. A Refinement of Crystal Structure of V6O13. *Acta Chem. Scand.* **1971**, *25*, 2675–2687.

(119) Bergström, Ö.; Gustafsson, T.; Thomas, J. O. Lithium Insertion into V6O13 Studied by Deformation Electron Density Refinement of Single-Crystal X-Ray Data. *Solid state ionics* **1998**, *110*, 179–186.

(120) Chaklanabish, N. C.; Maiti, H. S. Phase Stability and Electrical Conductivity of Lithium Intercalated Nonstoichiometric V6O13. *Solid State Ionics* **1986**, *21*, 207–212.

(121) Björk, H.; Lidin, S.; Gustafsson, T.; Thomas, J. O. Superlattice Formation in the Lithiated Vanadium Oxide Phases Li(0.67)V(6)O(13) and LiV(6)O(13). *Acta Crystallogr. B.* **2001**, *B57*, 759–765.

(122) Bergström, Ö.; Gustafsson, T.; Thomas, J. O. Electrochemically Lithiated Vanadium Oxide, Li2V6O13. *Acta Crystallogr. Sect. C Cryst. Struct. Commun.* **1997**, *53* (5), 528–530.

(123) Bergström, Ö.; Gustafsson, T.; Thomas, J. O. Electrochemically Lithiated Vanadium Oxide, Li3V6O13. *Acta Crystallogr. Sect. C Cryst. Struct. Commun.* **1998**, *54* (9), 1204–1206.

(124) Höwing, J.; Gustafsson, T.; Thomas, J. O. Li(3+δ)V6O13: A Short-Range-Ordered Lithium Insertion Mechanism. *Acta Crystallogr. B.* **2004**, *60* (4), 382–387.

(125) Braithwaite, J. S.; Catlow, C. R. A.; Harding, H.; Gale, J. D.; July, A. A Theoretical Study of Lithium Intercalation into V6O13 - a Combined Classical , Quantum Mechanical Approach. *Phys. Chemstry Chem. Phys.* **2001**, *3* (18), 4052–4059.

(126) Schmitt, T.; Duda, L.-C.; Matsubara, M.; Mattesini, M.; Klemm, M.; Augustsson, a.; Guo, J.-H.; Uozumi, T.; Horn, S.; Ahuja, R.; Kotani, a.; Nordgren, J. Electronic Structure Studies of V6O13 by Soft X-Ray Emission Spectroscopy: Band-like and Excitonic Vanadium States. *Phys. Rev. B* **2004**, *69* (12), 125103.

(127) Schmitt, T.; Augustsson, A.; Nordgren, J.; Duda, L.-C.; Höwing, J.; Gustafsson, T.; Schwingenschlögl, U.; Eyert, V. Electronic Structure of Li-Inserted V6O13 Battery Cathodes: Rigid Band Behavior and Effects of Hybridization. *Appl. Phys. Lett.* **2005**, *86* (6), 64101.

(128) Kobayashi, G.; Nishimura, S. I.; Park, M. S.; Kanno, R.; Yashima, M.; Ida, T.; Yamada, A. Isolation of Solid Solution Phases in Size-Controlled Li xFePO4 at Room Temperature.

Adv. Funct. Mater. **2009**, *19* (3), 395–403.

(129) Liang, H.-P.; Du, J.; Jones, T. G. J.; Lawrence, N. S.; Meredith, A. W. Large-Scale Production of V6O13 Cathode Materials Assisted by Thermal Gravimetric Analysis–Infrared Spectroscopy Technology. *ACS Appl. Mater. Interfaces* **2016**, *8* (39), 25674–25679.

(130) Meng, W.; Pigliapochi, R.; Bayley, P. M.; Pecher, O.; Gaultois, M. W.; Seymour, I. D.; Liang, H.; Xu, W.; Wiaderek, K. M.; Chapman, K. W.; Grey, C. P. Unraveling the Complex Delithiation and Lithiation Mechanisms of the High Capacity Cathode Material V 6 O 13. *Chem. Mater.* **2017**, *29*, 5513–5524.

(131) Sloop, S. E.; Pugh, J. K.; Wang, S.; Kerr, J. B.; Kinoshita, K. Chemical Reactivity of PF[sub 5] and LiPF[sub 6] in Ethylene Carbonate/Dimethyl Carbonate Solutions. *Electrochem. Solid-State Lett.* **2001**, *4* (4), A42–A44.

(132) Barlow, C. G. Reaction of Water with Hexafluorophosphates and with Li Bis (Perfluoroethylsulfonyl) Imide Salt. *Electrochem. Solid-State Lett.* **1999**, *2* (8), 362–364.

(133) Sloop, S. E.; Kerr, J. B.; Kinoshita, K. The Role of Li-Ion Battery Electrolyte Reactivity in Performance Decline and Self-Discharge. *J. Power Sources* **2003**, *119–121*, 330–337.

(134) Dahbi, M.; Ghamouss, F.; Tran-Van, F.; Lemordant, D.; Anouti, M. Comparative Study of EC/DMC LiTFSI and LiPF6 Electrolytes for Electrochemical Storage. *J. Power Sources* **2011**, *196* (22), 9743–9750.

(135) Borkiewicz, O. J.; Shyam, B.; Wiaderek, K. M.; Kurtz, C.; Chupas, P. J.; Chapman, K. W. The AMPIX Electrochemical Cell: A Versatile Apparatus for in Situ X-Ray Scattering and Spectroscopic Measurements. *J. Appl. Crystallogr.* **2012**, *45* (1), 1261–1269.

(136) Stinton, G. W.; Evans, J. S. O. Parametric Rietveld Refinement. *J. Appl. Crystallogr.* **2007**, *40* (Pt 1), 87–95.

(137) Toby, B. H.; Von Dreele, R. B. GSAS-II: The Genesis of a Modern Open-Source All Purpose Crystallography Software Package. *J. Appl. Crystallogr.* **2013**, *46* (2), 544–549.

(138) Thompson, P.; Cox, D. E.; Hastings, J. B. Rietveld Refinement of Debye–Scherrer Synchrotron X-Ray Data from Al2O3. *J. Appl. Crystallogr.* **1987**, *20*, 79–83.

(139) Rietveld, H. M. A Profile Refinement Method for Nuclear and Magnetic Structures. *J. Appl. Crystallogr.* **1969**, *2* (2), 65–71.

(140) Young, R. a.; Wiles, D. B. Profile Shape Functions in Rietveld Refinements. *J. Appl. Crystallogr.* **1982**, *15* (4), 430–438.

(141) Pawley, G. S. Unit-Cell Refinement from Powder Diffraction Scans. *J. Appl. Crystallogr.* **1981**, *14* (6), 357–361.

(142) Von Dreele, R. B. Quantitative Texture Analysis by Rietveld Refinement. *J. Appl. Crystallogr.* **1997**, *30* (4), 517–525.

(143) Kresse, G.; Furthmüller, J. Efficient Iterative Schemes for Ab Initio Total-Energy Calculations Using a Plane-Wave Basis Set. *Phys. Rev. B* **1996**, *54* (16), 11169–11186.

(144) Blöchl, P. E. Projector Augmented-Wave Method. *Phys. Rev. B* **1994**, *50* (24), 17953–17979.

(145) Perdew, J. P.; Burke, K.; Ernzerhof, M. Generalized Gradient Approximation Made Simple. *Phys. Rev. Lett.* **1996**, *77* (18), 3865–3868.

(146) Anisimov, V. I.; Zaanen, J.; Andersen, O. K. Band Theory and Mott Insulators: Hubbard U instead of Stoner I. *Phys. Rev. B* **1991**, *44* (3), 943–954.

(147) Anisimov, V. I.; Solovyev, I. V.; Korotin, M. A.; Czyyk, M. T.; Sawatzky, G. A. Density-Functional Theory and NiO Photoemission Spectra. *Phys. Rev. B* **1993**, *48* (23), 16929–16934.

(148) Liechtenstein, A. I.; Anisimov, V. I.; Zaanen, J. Density-Functional Theory and Strong Interactions: Orbital Ordering in Mott-Hubbard Insulators. *Phys. Rev. B* **1995**, *52* (8), 5467–5471.

(149) Toriyama, T.; Nakayama, T.; Konishi, T.; Ohta, Y. Charge and Orbital Orderings Associated with Metal-Insulator Transition in V6O13. *Phys. Rev. B* **2014**, *90* (8), 85131.

(150) Van Der Ven, A.; Thomas, J. C.; Xu, Q.; Swoboda, B.; Morgan, D. Nondilute Diffusion from First Principles: Li Diffusion in LixTiS2. *Phys. Rev. B - Condens. Matter Mater. Phys.* **2008**, *78* (10), 1–12.

(151) Van der Ven, A.; Thomas, J. C.; Xu, Q.; Bhattacharya, J. Linking the Electronic Structure of Solids to Their Thermodynamic and Kinetic Properties. *Math. Comput. Simul.* **2010**, *80* (7), 1393–1410.

(152) Kim, J.; Middlemiss, D. S.; Chernova, N. A.; Zhu, B. Y. X.; Masquelier, C.; Grey, C. P. Linking Local Environments and Hyperfine Shifts: A Combined Experimental and Theoretical 31P and 7Li Solid-State NMR Study of Paramagnetic Fe(III) Phosphates. *J. Am. Chem. Soc.* **2010**, *132* (47), 16825–16840.

(153) Dovesi, R.; Orlando, R.; Civalleri, B.; Roetti, C.; Saunders, V. R.; Zicovich-Wilson, C. M. CRYSTAL: A Computational Tool for the Ab Initio Study of the Electronic Properties of Crystals. *Zeitschrift für Kristallographie - Crystalline Materials*. 2005, p 571.

(154) Becke, A. D. Density-functional Thermochemistry. III. The Role of Exact Exchange. *J. Chem. Phys.* **1993**, *98* (7), 5648–5652.

(155) Muñoz-Rojas, D.; Leriche, J.-B.; Delacourt, C.; Poizot, P.; Palacín, M. R.; Tarascon, J.-M. Development and Implementation of a High Temperature Electrochemical Cell for Lithium Batteries. *Electrochem. commun.* **2007**, *9* (4), 708–712.

(156) Chianelli, R. R.; Scanlon, J. C.; Rao, B. M. L. Ln Situ Studies of Electrode Reactions: The Mechanism of Electrode Reactions : Of Lithium Intercalation in TiS2*. *J. Solid State Chem.* **1979**, *29*, 323–337.

(157) Courtney, I. A.; Dahn, J. R. Electrochemical and in Situ X-Ray Diffraction Studies of the Reaction of Lithium with Tin Oxide Composites. *J. Electrochem. Soc.* **1997**, *144* (6), 2045–2052.

(158) Hatchard, T. D.; Dahn, J. R. In Situ XRD and Electrochemical Study of the Reaction of Lithium with Amorphous Silicon. *J. Electrochem. Soc.* **2004**, *151* (6), 838–842.

(159) Richard, M. N., Koetschau, I. , Dahn, J. R. A Cell for In Situ X-Ray Diffraction Based on Coin Cell Hardware and Bellcore Plastic Electrode Technology. *J. Electrochem. Soc.* **1997**, *144* (2), 554–557.

(160) Koetschau, I. Orthorhombic LiMnO[sub 2] as a High Capacity Cathode for Li-Ion Cells. *J. Electrochem. Soc.* **1995**, *142* (9), 2906.

(161) Nikolowski, K.; Baehtz, G.; Bramnik, N. N.; Ehrenberg, H. A Swagelok-Type in Situ Cell for Battery Investigations Using Synchrotron Radiation. *J. Appl. Crystallogr.* **2005**, *38* (5), 851–853.

(162) Ronci, F.; Scrosati, B.; Albertini, V. R.; Perfetti, P. In Situ Energy Dispersive X-Ray Diffraction Study of LiNi0.8Co0.2O2 Cathode Material for Lithium Batteries. *J. Phys. Chem. B* **2001**, *105* (4), 754–759.

(163) Marco, R. De; Veder, J.-P. In Situ Structural Characterization of Electrochemical Systems Using Synchrotron-Radiation Techniques. *TrAC Trends Anal. Chem.* **2010**, *29* (6), 528–537.

(164) Morcrette, M.; Chabre, Y.; Vaughan, G.; Amatucci, G.; Leriche, J. B.; Patoux, S.; Masquelier, C.; Tarascon, J. M. In Situ X-Ray Diffraction Techniques as a Powerful Tool to Study Battery Electrode Materials. *Electrochim. Acta* **2002**, *47* (19), 3137–3149.

(165) Braun, A.; Shrout, S.; Fowlks, A. C.; Osaisai, B. A.; Seifert, S.; Granlund, E.; Cairns, E. J. Electrochemical in Situ Reaction Cell for X-Ray Scattering, Diffraction and Spectroscopy. *J. Synchrotron Radiat.* **2003**, *10* (4), 320–325.

(166) Balasubramanian, M.; Sun, X.; Yang, X. .; McBreen, J. In Situ X-Ray Diffraction and X-

Ray Absorption Studies of High-Rate Lithium-Ion Batteries. *J. Power Sources* **2001**, *92* (1–2), 1–8.

(167) Borkiewicz, O. J.; Wiaderek, K. M.; Chupas, P. J.; Chapman, K. W. Best Practices for Operando Battery Experiments: Influences of X-Ray Experiment Design on Observed Electrochemical Reactivity. *J. Phys. Chem. Lett.* **2015**, *6* (11), 2081–2085.

(168) Liu, H.; Grey, C. P. Influence of Particle Size, Cycling Rate and Temperature on the Lithiation Process of Anatase TiO_2. *J. Mater. Chem. A* **2016**, *4* (17), 6433–6446.

(169) Gibot, P.; Casas-Cabanas, M.; Laffont, L.; Levasseur, S.; Carlach, P.; Hamelet, S.; Tarascon, J.-M.; Masquelier, C. Room-Temperature Single-Phase Li Insertion/extraction in Nanoscale Li(x)FePO4. *Nat. Mater.* **2008**, *7* (9), 741–747.

(170) Adler, D. Mechanisms for Metal-Nonmental Transitions in Transition-Metal Oxides and Sulfides. *Rev. Mod. Phys.* **1968**, *40* (4), 714–736.

(171) Kawashima, K.; Ueda, Y.; Kosuge, K.; Kachi, S. Crystal Growth and Some Electric Properties of V6O13. *J. Cryst. Growth* **1974**, *26*, 321–322.

(172) Dernier, P. D. Structural Investigation of the Metal-Insulator Transition in V6O13. *Mater. Res. Bull.* **1974**, *9*, 955–963.